Colloids in Non–Equilibrium: Dynamical Density Functional Theory of Colloidal Suspensions under External Forcing

Inaugural-Dissertation

zur Erlangung des Doktorgrades der
Mathematisch-Naturwissenschaftlichen Fakultät
der Heinrich-Heine-Universität Düsseldorf

vorgelegt von

Urs Zimmermann
aus Bochum

Düsseldorf, November 2017

aus dem Institut für Theoretische Physik II: Weiche Materie
der Heinrich-Heine-Universität Düsseldorf

Gedruckt mit der Genehmigung der
Mathematisch-Naturwissenschaftlichen Fakultät der
Heinrich-Heine-Universität Düsseldorf

Referent: Prof. Dr. Hartmut Löwen

Korreferent: Prof. Dr. Jürgen Horbach

Tag der mündlichen Prüfung: 15. Januar 2018

Abstract

Many physical processes and phenomena in our environment are inherently out of thermodynamic equilibrium. It remains a challenge to physicists to describe, analyze and understand non-equilibrium systems. The thesis at hand focuses on the theoretical description of transport processes in various colloidal systems using the dynamical density functional theory (DDFT). As a theoretical framework, DDFT describes the temporal evolution of the averaged particle density distribution of the colloidal suspension. This thesis includes studies of three different colloidal systems.

First, we consider non-interacting colloidal particles in a periodic potential energy landscape subjected to an external driving force. This force consists of two components: a constant and a time-modulated part. The natural frequency of the particle motion over the periodic landscape couples to the modulation frequency and results in a synchronization of particle movement into discrete modes. We summarize the resulting transport properties and their dependence on the modulation frequency and drive amplitudes via state diagrams. Furthermore, we deduce an analytic approximate theory and compare it to experiments, simulations, and DDFT. The different investigation results are in very good agreement with each other.

In the second study, we examine the flow of repulsive colloidal particles through a two–dimensional microchannel induced by a constant driving force. The effect of a geometrical constriction in the channel is studied as a function of its width and the strength of the particle interactions. Four qualitatively different flow patterns can be identified: complete blockade, constant particle flow, damped oscillatory flow and persistent oscillations. State diagrams of these patterns are displayed. Moreover, we show a qualitative different oscillation behavior in the persistent oscillations regime that depends on the parity of particle layering in the channel. A good qualitative agreement between DDFT predictions and computer simulations is found.

The third study explores the resistance imposed by obstacles to the flow of repulsive colloidal particles driven by a constant force in a two-dimensional microchannel. We investigate deviations from additivity of the resistances of two energetic barriers put in series. For barrier separation distances comparable to the correlation length of the particles, the resistance is strongly non-additive. The increase in resistance caused by a second barrier can be either much larger, smaller, or even negative, depending on its position with respect to the first barrier. The latter case is of particular importance, since in this situation particle transport, counterintuitively, is facilitated by the presence of an additional obstacle. This interesting effect is analyzed and explained by the structure of the suspension between the obstacles that enables an enhanced

particle transport via fluctuations.

Zusammenfassung

Viele physikalische Prozesse und Phänomene in unserer direkten Umgebung finden jenseits des thermodynamischen Gleichgewichts statt. Es bleibt weiterhin eine Herausforderung der Physik, grundlegende Einsichten in die Dynamik solcher Vorgänge zu erlangen. Die vorliegende Dissertation untersucht Transportprozesse dreier kolloidaler Systeme mit verschiedenen Wechselwirkungen in Gegenwart von externen Feldern. Methodischer Schwerpunkt ist hierbei die dynamische Dichtefunktionaltheorie (DDFT), mit der die zeitliche Entwicklung einer mittleren Teilchendichte beschrieben werden kann.

Die erste Studie untersucht nicht-wechselwirkende kolloidale Teilchen, die in einer periodischen Potentiallandschaft von einer externen Kraft getrieben werden. Die treibende Kraft setzt sich zusammen aus einer konstanten und einer zeitperiodischen Kraftkomponente. Durch eine Synchronisation der zeitperiodischen Kraft mit der intrinsischen Bewegungsfrequenz, hervorgerufen durch die konstante treibende Kraft und das periodische Potential, zerfällt die Kolloidbewegung in diskrete Moden. Die Abhängigkeit der Transportcharakteristika von der Frequenz der äußeren Kraft and der Amplituden beider Kraftkomponenten werden umfassend untersucht und in Zustandsdiagrammen dargestellt. Numerische Lösungen der DDFT zeigen im Vergleich mit Ergebnissen aus Experiment und Simulation eine hervorragende Übereinstimmung. Des Weiteren wird mit der DDFT die Güte einer analytischen Näherung bestimmt und das Diffusionsverhalten des Teilchens bei verschiedenen Parameterkombinationen charakterisiert.

In der zweiten Arbeit wird der Teilchenfluss von repulsiven kolloidalen Teilchen durch einen zweidimensionalen Kanal betrachtet, der durch eine konstante treibende Kraft hervorgerufen wird. Hierbei wird der Einfluss einer Verengung des Kanals in Abhängigkeit der Wechselwirkungsstärke der Kolloide untereinander auf das Flussverhalten betrachtet. Vier qualitativ unterschiedliche Flussmuster können sowohl in der DDFT als auch in Simulationen nachgewiesen werden: komplette Blockade, konstanter Teilchenfluss sowie gedämpft schwingender und persistent oszillierender Teilchenstrom. In einem Zustandsdiagramm werden die Flussmuster in Abhängigkeit von Wechselwirkungsstärke und Verengungsbreite dargestellt, wobei eine qualitative Übereinstimmung von DDFT und Simulation besteht. Es wird ferner gezeigt, dass das Schwingungsverhalten im Bereich des persistent oszillierenden Kolloidstroms von der Anzahl der Teilchenschichten entlang des Kanals abhängt.

Das dritte hier vorgestellte System besteht aus einer Suspension mit repulsiv wechselwirkenden Kolloiden, die von einer konstanten Kraft durch einen zweidimensionalen

Mikrokanal getrieben wird, in bis zu zwei Potentialbarrieren eingeführt werden. Der durch die Barrieren hervorgerufene Widerstand wird untersucht und der Frage nachgegangen, inwiefern die Widerstände zweier in Reihe geschalteter Barrieren additiv sind. Hierbei deuten Daten aus einem Experiment eine Nicht-Additivität an, die mit Hilfe von DDFT und Simulationen eingehend untersucht wird. Die Stärke des zweiten Widerstandes kann – abhängig von dem Abstand zum ersten Hindernis – sehr viel größer, kleiner oder sogar negativ sein. Im letzteren Fall ist der Widerstand von zwei Hindernissen effektiv einfacher zu überwinden, als dasselbe System mit einer einzelnen Barriere. Dieser nicht-intuitive Effekt wird näher analysiert und mit der Strukturbildung der Suspension zwischen den Hindernissen erklärt.

Eidesstattliche Versicherung

Ich versichere an Eides Statt, dass die Dissertation von mir selbständig und ohne unzulässige fremde Hilfe unter Beachtung der „Grundsätze zur Sicherung guter wissenschaftlicher Praxis an der Heinrich-Heine-Universität Düsseldorf“ erstellt worden ist.

Ort, Datum

Urs Zimmermann

Danksagung

Eine Dissertation entsteht in der Regel nicht in einem abgeschlossenen Raum, vielmehr trägt eine Vielzahl von Personen zur ihrer Entstehung bei. Ich möchte mich in diesem Rahmen bei den Menschen bedanken, die in ganz besonderem Maße zur Dissertation beigetragen haben.
Der größte Dank gilt meinem Doktorvater Prof. Dr. Hartmut Löwen, der mich während der Promotionszeit stets unterstützt und gefördert hat. Aus unseren Diskussionen konnte ich gute Ratschläge und wertvolle Denkanstöße mitnehmen.
Ebenfalls danken möchte ich Dr. Frank Smallenburg, mit dem ich viele Fragestellungen diskutieren und daraus Ideen entwickeln konnte. Darüber hinaus hat er Simulationsdaten zu zwei Publikationen beigesteuert.
Ein besonderer Dank geht an Dr. Christian Kreuter, Dr. habil Artur Erbe und Prof. Dr. Paul Leiderer, die ihre Daten aus Experimenten zu Doppelbarrieresystemen für eine Kooperation zur Verfügung gestellt haben.
Auch möchte ich mich bei Dr. Roel Dullens und den Kolleginnen und Kollegen seiner Arbeitsgruppe an der University of Oxford bedanken, in der ich als Gastwissenschaftler tätig war. Besonders hervorheben möchte ich Dr. Michael Juniper, mit dem infolge meines Aufenthaltes eine Publikation hervorgegangen ist.
Für die Zeit meines Aufenthaltes in Oxford wurde ich vom Deutschen Akademischen Austauschdienst (DAAD) gefördert, dem ich ebenfalls danken möchte. Die Finanzierung durch den DAAD hat dieser Aufenthalt erst ermöglicht.
Ich danke allen aktuellen und ehemaligen Mitgliedern des Lehrstuhls Theoretische Physik II: Weichen Materie für die überaus gute und kollegiale Atmosphäre. Die Arbeit am Lehrstuhl hat mir immer große Freude bereitet.
Für die sorgfältige Durchsicht der Dissertationsschrift möchte ich mich bei folgenden Personen besonders bedanken: Martin Nopper, Giorgio Pessot sowie Uwe, Irene, Valeriya, Leif, Jill und Ronja Zimmermann.
Spezieller Dank geht an meine Eltern Uwe und Irene, die mich in vielerlei Hinsicht unterstützt haben.
Ein ganz besonderer und herzlicher Dank gilt meiner Ehefrau Valeriya, die mir auch in schweren Zeiten immer zur Seite stand und mir während der Promotionszeit einen wundervollen Sohn geschenkt hat.

Inhaltsverzeichnis

1 Introduction

1.1 Soft Matter

The state of matter is commonly classified into three fundamental categories: gas, liquid, and solid. Yet, in our everyday life we are surrounded by materials that do not fit into this scheme: they are ordered to some extent, but rather than rigid they are 'soft', in the sense that they can be easily deformed by hand. As an example, we may find whipped cream, Götterspeise, or bread in the kitchen, toothpaste, lipsticks, or sponges in the bathroom, and on our desk there may be erasers, ink, and a computer monitor with a liquid crystal display (LCD). Most notably, our bodies consist of soft tissue such as muscles, fat, skin, fasciae, or nerves. These kinds of material are generally referred to as *soft matter* [1–3].

Two properties are common to soft matter systems that make them important for functional or smart materials as well as for living organisms: weak ordering on length scales larger than atomic ones and strong response towards small changes in environmental conditions causing dramatic changes of macroscopic properties [4,5]. The first property opens a window to very complex materials which is an essential ingredient for living organisms. The biochemist Dikran Dervichian expressed the importance of intermediate ordering between crystalline solid and liquid – here with respect to liquid crystals – with the words:

> "Liquid crystals stand between the isotropic liquid phase and the strongly organized solid state. Life stands between complete disorder, which is death and complete rigidity, which is death again." [6].

The second property is important for dynamical behavior and rapid reactions to external impulses, a key feature for higher forms of life [3].

Apart from just understanding the numerous examples of soft matter in nature and modern life, there is also the possibility to enhance applications or even craft completely new materials with special mechanical, optical, electric, or magnetic characteristics [7]. An emerging technology is, for instance, artificial muscles [8–10] that can be used as a prosthesis or to construct flexible robots. Another future application is targeted drug delivery inside the human body using controllable container particles [11–13]. Furthermore, medical agents are imaginable that perform disease treatment from the inside, following the vision to "swallow the doctor", as Richard Feynman proposed in his talk on nanotechnology [14].

Soft matter is a rather interdisciplinary field of research on the interface between physics, chemistry, biochemistry, microbiology, materials science, and engineering [1, 15]. It is a collection of many subfields like colloidal suspensions [16], polymers [17,18], liquid crystals [19], amphiphilies [2], ferrogels [20], biomembranes and biopolymers [21], and complex plasmas [22]. Although some of these subfields have a long history track in science, it lasted to the 1960s until Pierre-Gilles de Gennes and Samuel Edwards categorized and studied soft matter in a systematic approach. De Gennes, who is often viewed as the father of soft matter, was awarded with the Nobel Prize in Physics in 1991 [23]. The name 'matière molle' – *soft matter* – is attributed to a close collaborator of de Gennes, Madeleine Veyssié, and was initially meant as a joke [4]. However, it evolved as a common term for the area of research along with 'complex fluids', a term that is often used synonymously [7, 24].

This cumulative thesis is about various colloidal systems in non-equilibrium and description via dynamical density functional theory thereof. This introductory first chapter gives an overview of colloidal systems, gradually narrowing the focus to the actual colloidal systems studied in this thesis. In the second chapter an analytical study is presented discussing the set-up of Paper III for non-interacting particles. The main scientific work is presented in the third chapter including reprints of the scientific publications.

This introduction first discusses general characteristics and features of colloidal systems in section 1.2. Then, the Brownian motion of dilute colloidal suspensions is discussed with some historical annotations in section 1.3. The complexity of colloidal systems can be classified into two categories: interparticle interactions and external fields [25]. Following this complexity scheme, we discuss particle-particle interactions and the influence of external fields in sections 1.4 and 1.5, respectively. Section 1.6 introduces the dynamical density functional theory as the theoretical framework used in this thesis. Finally, section 1.7 presents the systems of the papers in chapter 3 and discusses the main results as well as the insights.

1.2 Colloidal suspension

Colloidal suspensions are a subfield of soft matter. In this section, we first explain what is understood by a colloidal suspension. Then, we highlight remarkable properties of colloidal systems. Finally, we outline the most common approaches to simplify the systems in order to efficiently describe them in theories.

1.2.1 What are colloidal suspensions?

Colloidal suspensions are particles of size 1nm - 10μm that are immersed in an atomic or molecular medium. The dispersed particles are called *colloids* and the characteristic length scale is referred to as *mesoscopic*, which is orders of magnitude larger than

the size of the solvent particles [26, 27]. However, the size of colloids is not sharply defined, but rather set by two requirements. As a lower limit, the colloids have to be considerably larger than the solvent constituents so interactions between solvent and colloids can be viewed in an averaged, coarse-grained manner. The upper limit criterion is that colloidal particles have to be small enough that thermal fluctuations are an important part of the dynamics [16, 28]. This way, colloids are sometimes described as "big atoms" [29] or "large molecules" [16] that are large enough, however, to disregard quantum interference effects. Typical examples of colloidal suspensions are ink, milk, or red blood cells.

1.2.2 Features of colloidal suspensions

In its simplest representation, colloidal dispersions consist of a single type of equally-sized colloids. Despite this simplicity, however, the macroscopic behavior can differ strongly: depending on the effective interparticle interactions, colloidal systems can adopt various phases. Aside from dilute gas-like and fluid phases, a rich variety of partially ordered phases can be observed even for one-component colloidal systems. One can roughly distinguish between translational ordered phases such as layering, liquid crystal, hexagonal (columnar), plastic crystal, or several crystalline phases and between orientational ordered phases, for example nematic and smectic phases [1, 30]. Furthermore, there are also aperiodic ordered phases that form quasicrystals [31, 32].

Another great advantage is that colloidal systems are experimentally accessible in many aspects. One aspect is visual accessibility. The mesoscopic length scale is very well observable using optical microscopy [33]. Moreover, one of the most important advances in microscopy is the invention of confocal microscopy, a technique that is able to create three-dimensional pictures of a colloidal sample in real–time [34, 35]. Since the separation distances of particles are comparable to the wavelength of visible light, Bragg reflections can be observed indicating the emergence of colloidal crystals. The internal structure of a colloidal sample can be further analyzed by performing static or dynamic light scattering with simple laser devices [36–38]. Another aspect is amendable dynamic properties. The typical time scale of colloidal motion is in the range of microseconds to seconds, a time that is very well resolvable by cameras or bare eye. Researchers are virtually able to *see* the dynamics of transition processes and evaluate them statistically using particle tracking applications [39, 40]. Finally, experiments on colloidal suspensions are of relatively low cost, compared to other fields of research where huge machines or expensive materials are needed.

This accessibility is in great contrast to, for instance, atomic systems where direct observation of the underlying processes is not possible [29, 41]. Therefore, colloidal systems are excellent models to study less accessible systems [42–44]. Dynamical processes like nucleation, crystal growth, spinodal decomposition, and melting can be made visible [45, 46]. Consequently, "complex fluids are ideal laboratories for non-equilibrium physics." [47].

The interparticle interactions of colloidal suspensions are not preassigned by electron configurations, as this is the case for atomic systems. In fact, it is possible to tune or even design the interaction potential of colloids by external fields [44, 48] or proper chemical engineering [49–51]. This tuning capability is essential to mimic interactions of less accessible systems. It can also be used to tailor interactions in order to design novel functional material. Aside from controlling the interaction potential of colloidal particles, there is great freedom in preparing external potential landscapes and geometric confinements by either lithography [52,53] or optical potentials [54,55]. Moreover, with optical laser tweezers manipulations can be performed on the level of individual particles [56, 57].

All in all, these comprehensive possibilities to prepare experimental set-ups allow to arrange colloidal systems according to theoretical assumptions to test the validity and limitations of certain theories [58]. Great progress has been made thanks to this close link between experimental systems and theoretical modeling.

1.2.3 Theoretical modeling

A better understanding of colloidal systems has been achieved by a combination of experimental studies with predictions from computer simulations and insights from theories [58, 59]. Although the presence of several time, energy and length scales in colloid dispersions is the source of a stunning variety of macroscopic phenomena, it is highly challenging from the theoretical perspective. The need for simplifications is apparent to take account of the mesoscopic and microscopic scale in order to describe macroscopic effects.

The microscopic scale is usually viewed in a coarse-grained manner so that the extensive number of particles in the suspension medium are treated as a *continuum* [16]. This approach is justified due to the big differences between the colloids and the solvent particles in terms of size as well as relaxation times. While the molecular components move rapidly at high collision rate, the dynamics of mesoscopic particles are much slower. Therefore, the solvent particles can be assumed to be instantly in equilibrium. On the mesoscopic level, the effects of the solvent medium onto the colloids can be described via fluid dynamics [60]. Note, however, that an important characteristic of colloidal suspensions – the thermal motion of the colloids – stems from the discrete nature of the fluid constitutes, as detailed in section 1.3. In theoretical modeling, this thermal motion is represented by a phenomenological random and uncorrelated force acting on the colloids.

Further simplifications are made with respect to the internal structure of colloids. While the internal details of colloids are important to chemical reactions or biochemical processes, they are not needed to understand collective effects like phase behavior. For this reason, the – possibly complicated – internal structure of colloids is usually not considered in favor of effective interactions between the colloids. In this sense, long polymers or large proteins may also share some aspect of colloidal systems [16,17,28].

In order to get a profound understanding of fundamental mechanisms that drive macroscopic behavior, it is advisable to start studying systems as simple as possible, and later include additional elements with increasing complexity.

1.3 Brownian motion

The most simple colloidal systems are very dilute suspensions at rest. The study of such a system is essential to lay the foundations for a more profound understanding of more complicated systems. Moreover, the discovery and comprehension of the thermally activated motion of colloids, commonly known as *Brownian motion*, has been an important milestone in science.

Although the random motion of mesoscopic particles in a suspension has been observed before [61], its discovery is commonly attributed to the botanist Robert Brown, who in 1827 observed pollen grains dissolved in water under a microscope. In his studies he noted that the visible particles moved erratically [16, 62]. Brown could also disprove the hypothesis that this motion was in any kind related to life by finding the same kind of motion pattern for clearly inanimate dissolved particles [62]. He also carefully ruled out possible sources of this motion like evaporation or surface effects of the suspension, but he could not provide any explanation of the mechanisms behind it.

In the first of his *Annus Mirabilis* papers Albert Einstein [63] and independently Marian von Smoluchowski [64] in 1906 provided a theoretical explanation for Brownian motion: many microscopic particles of the surrounding medium collide at high frequency with the dissolved mesoscopic particles, each transferring a tiny momentum. Fluctuations in the collision rate along the colloidal surface result in an effective push on the colloid. These pushes change rapidly in intensity and direction, causing a continuous jittery motion of the colloidal particle. Einstein and Smoluchowski could accurately describe Brownian Motion as a diffusion process.

One remarkable aspect of this theoretical explanation is the assumption that the solvent consists of many atomic or molecular particles. By the time of publication the discrete nature of matter was still a debated and not commonly accepted theory. From the theoretical explanation of Brownian motion, Avogadro's number could be predicted. Inspired by this theoretical model, Jean Baptiste Perrin performed experiments and could prove the existence of atoms and molecules in 1909 [65]. Perrin's research finally put an end to the long debate about the existence of atoms; in 1926, he was awarded with the Nobel Prize in Physics [66].

1.4 Particle interactions

An ensemble of non-interacting particles – often referred to as *ideal gas* – can in many situations be completely described by an analytical solution [67]. Apart from few exceptions, this is not the case if interactions between particles are present. Interparticle interactions introduce a high level of complexity to the system, transforming a local problem, where a particle behavior is only determined by external potentials at the current position, to a global problem, where the dynamics of a particle are influenced by all other particles and the emerging structure. This additional complexity manifests in rich phase behaviors even for one-component particle ensembles and is the origin of the wide variety of features that can be found in colloidal suspensions.

A broad range of particle interaction potentials exist in colloidal systems. Some interactions are inherently present like van der Waals attraction between colloids [68, 69] or solvent-mediated hydrodynamic interactions [60]. Other interactions can be tuned by external fields or by changing the salt concentration of the medium. Some colloidal interactions are specially prepared or designed by attaching functional chemical groups on the surface, as this is the case for, e.g., patchy particles [70–72].

First, this section presents the hard sphere interaction potential which is of great theoretical interest. Second, we discuss the interaction potential of repulsive magnetic dipoles used in Paper II and Paper III.

1.4.1 Hard spheres

The most simple nontrivial particle interaction is the model of hard spheres, i.e., spherical particles with a hard, impenetrable core that do not interact except for prohibiting overlap configurations. The pairwise interaction potential of two colloids of diameter σ_1 and σ_2 at positions $\mathbf{r}_1$ and $\mathbf{r}_2$, respectively, is governed by

$$V_{\text{int}}(\mathbf{r}_1, \mathbf{r}_2) = \begin{cases} \infty, & \text{for } |\mathbf{r}_1 - \mathbf{r}_2| < \frac{\sigma_1+\sigma_2}{2} \\ 0, & \text{for } |\mathbf{r}_1 - \mathbf{r}_2| \geq \frac{\sigma_1+\sigma_2}{2} \end{cases} . \tag{1.1}$$

An often adopted simplification in theory is the assumption of a monodisperse system, i.e., $\sigma_1 = \sigma_2 \equiv \sigma$. However, *real* monodispersity is difficult to achieve in experiments, a variation in particle size of several percent is to be expected om most colloidal hard sphere probes [73, 74]. The degree of polydispersity is an important information since it affects transition lines between phases or even prevent the emergence of phases [75].

The hard sphere potential can be regarded as an extension of the ideal gas with the addition of hard cores to the particles. In contrast to the ideal gas, hard sphere suspensions are not limited to a gas-like phase. A crystalline phase for densities much lower than the closest packing was predicted by early computer simulations and theories in the 1950s [76–78]. By then, these theoretical results were highly controversial until in 1986 the crystallization of hard sphere suspensions was observed experimentally [79]. The fascinating aspect of this phase is that freezing of the hard sphere

suspension is purely driven by entropy [80]. Furthermore, hard spheres can arrange in a persistent metastable glass phase [75, 81, 82].

Because of its simplicity and the ability to account for phase transitions, hard spheres are a fundamental theoretical model that serves as an excellent benchmark for new theoretical frames. Related to the hard sphere model are other hard core potentials that prohibit particle overlap configurations for different geometrical shapes [83–85]. Notable examples are spherocylinders [86, 87], parallel and non-parallel cubes [88–90], or dumbbells [91, 92]. In specially prepared hard core systems we can find even unusual effects. For example, parallel cubes exhibit a second order phase transition between fluid and simple crystal phase that remains persistent even for parallel spherocubes, i.e., cubes with rounded edges [89, 93].

1.4.2 Paramagnetic particles

Colloidal particles that include a core of paramagnetic material are being used in Paper II and Paper III. A feature of paramagnetic particles is their interaction that is tunable by an external magnetic field $\mathbf{B}_{\text{ext}}$. This magnetic field induces a magnetic dipolar momentum, which can be linearized for small strengths of the magnetic field: $\mathbf{m} = \chi_{\text{eff}}\mathbf{B}_{\text{ext}}$, with χ_{eff} the effective magnetic susceptibility [94, 95]. A dipolar particle centered in the origin of a reference system generates a magnetic field [96]

$$\mathbf{B}_m(\mathbf{r}) = \frac{\mu_0}{4\pi} \cdot \frac{(3(\hat{\mathbf{r}} \cdot \mathbf{m})\hat{\mathbf{r}} - \mathbf{m})}{r^3}, \tag{1.2}$$

with μ_0 the vacuum permeability, $r = |\mathbf{r}|$ the length and $\hat{\mathbf{r}} = \frac{\mathbf{r}}{|\mathbf{r}|}$ the orientation of position $\mathbf{r}$.

We consider two paramagnetic particles at positions $\mathbf{r}_1$ and $\mathbf{r}_2$ with $\mathbf{r} = \mathbf{r}_1 - \mathbf{r}_2$ and with magnetic dipole moments $\mathbf{m}_1$ and $\mathbf{m}_2$, respectively. The pairwise interaction potential is

$$\begin{aligned} V_{\text{int}}(\mathbf{r}) &= -\mathbf{m}_1 \cdot \mathbf{B}_{m_2}(\mathbf{r}) = -\mathbf{m}_2 \cdot \mathbf{B}_{m_1}(-\mathbf{r}) \\ &= \frac{\mu_0}{4\pi} \cdot \frac{(\mathbf{m}_1 \cdot \mathbf{m}_2 - 3(\hat{\mathbf{r}} \cdot \mathbf{m}_1)(\hat{\mathbf{r}} \cdot \mathbf{m}_2))}{r^3}. \end{aligned} \tag{1.3}$$

If a homogeneous external magnetic field $\mathbf{B}_{\text{ext}}$ acts on the whole colloidal sample, we can assume that both magnetic dipole moments are oriented parallel to it and are of identical magnitude, i.e., $\mathbf{m}_1 = \mathbf{m_2} \equiv \mathbf{m}$. In this setting, the interaction potential simplifies to

$$V_{\text{int}}(\mathbf{r}) = \frac{\mu_0}{4\pi} \cdot \frac{(|\mathbf{m}|^2 - 3(\hat{\mathbf{r}} \cdot \mathbf{m})^2)}{r^3}. \tag{1.4}$$

Finally, by restricting the paramagnetic colloidal particles to a plane and applying the external magnetic field $\mathbf{B}_{\text{ext}}$ normal to that plane, the last term in eq. (1.4) vanishes and a purely repulsive interaction potential remains. It is inversely proportional

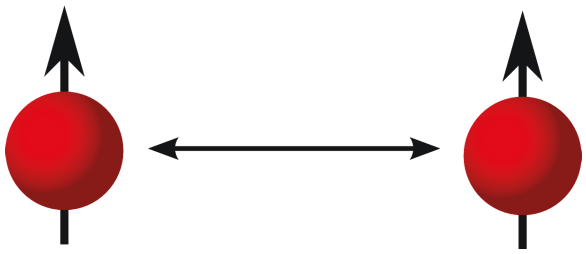

Abbildung 1.1: Sketch of two paramagnetic particles with parallel dipole moments induced by a uniform external magnetic field $\mathbf{B}_{\text{ext}}$. The particles are in a planar confinement, therefore the particle-particle interaction is purely repulsive, see eq. (1.5).

to the cube of the particle separation distance $r = |\mathbf{r}_1 - \mathbf{r}_2|$ and reads

$$\begin{aligned} V_{\text{int}}^{2D}(r) &= \frac{\mu_0}{4\pi} \cdot \frac{|\mathbf{m}|^2}{r^3} \\ &= \frac{\mu_0}{4\pi} \cdot \frac{\chi^2 |\mathbf{B}_{\text{ext}}|^2}{r^3}. \end{aligned} \tag{1.5}$$

This interaction potential is valid for point-like paramagnetic colloids in an external magnetic field. In experiments, the colloidal particles are of finite size and additional hard sphere interactions are present. In the case of a sufficiently strong external magnetic field these hard cores become irrelevant since the repulsion of two particles is sufficient to stabilize the colloids and prevent overlapping.

1.5 External fields

One aspect of complexity in colloidal systems is the presence of external fields [25]. They can influence a colloidal probe in manifold ways, ranging from confining colloids, inducing or modifying interparticle interactions, applying force fields to particles, to generating a flow field in the suspension medium [44, 97]. This section gives a brief classification of external fields in colloidal suspensions before discussing the significance of external fields in the papers of section 3.

1.5.1 Classification of external fields

Equilibrium and non-equilibrium

Bulk colloidal systems are usually in thermodynamic equilibrium. The presence of external fields can significantly disturb this inherent configuration and either force the system into another equilibrium state or even drive it out of equilibrium. A nearly open range of complexity is possible that is directly linked to the type of the

external field. It is therefore sensible to distinguish whether or not an equilibrium configuration exists for the system under study. Colloidal systems that are confined or exposed to static external energetic potentials usually reach an equilibrium state, whereas systems with time-dependent external potentials or force fields that do not stem from a potential are inherently out of equilibrium.

From the theoretical point of view equilibrium systems are of relatively easy to study because conceptually the route to obtain the relevant quantities is known from statistical mechanics [24, 98, 99]: First, calculate the respective partition function. Then, take its logarithm to obtain the corresponding thermodynamic quantity. Applying this *conceptual recipe* might be demanding or even unfeasible to calculate for a concrete system, but it sets a clear methodical framework. Furthermore, the equilibrium state is well-defined, unique, and depends on a relatively small set of parameters, the state variables.

In nature, non-equilibrium systems are prevalent; in fact, *life* itself is inherently out of equilibrium. There is no general recipe or route to characterize systems in non-equilibrium. However, they can qualitatively be classified into quasi-equilibrium, steady state non-equilibrium, and full non-equilibrium. The first one is slowly changing and can be assumed to be in equilibrium at each point of time. Steady state systems are not in equilibrium, but depend on few macroscopic variables that are independent of time. On the contrary, full non-equilibrium situations are characterized by a dynamic and aperiodic behavior, which usually strongly depends on the initial conditions.

Direct and indirect external forces

Among the applied external fields, it is a valuable question *how* these fields couple to the colloidal particles. This coupling can be classified as an either direct or indirect influence [16]. A direct force acts only on the colloidal particles, leaving the suspension medium unaffected. Examples include colloids exposed to a gravitational force field in a suspension medium at rest, laser-optical energetic landscapes, or charged or magnetic colloids in the presence of electric or magnetic fields.

A qualitative different situation is present for indirect external forces where the medium is not at rest but pushes the particle [60]. Here, the situation is much more complicated, since fluid dynamics equations – the Navier-Stokes equations – have to be solved for the medium that carries the particle along streamlines. In many practical situations hydrodynamic flow fields are present, for instance, in pressure induced flow through pipes and vessels, or shearing, stirring, shaking, and vibrating [60] a colloidal sample. As a rule of thumb indirect interactions lead to more complicated problems than direct external fields as the dynamics of the medium has to be taken into account, which is in many situations a challenging problem.

External force fields have to be distinguished from intrinsic forces that can drive a particle. In contrast to *passive particles* discussed so far, colloids that move according

to a self-propulsion mechanism are called *active particles* and have been studied with increasing interest in the last decade [85, 100–102] in various propulsion strategies [103–108] and confinements [105,109–116]. Active particles include artificial swimmers as well as microbiological agents like bacteria. Most self-propulsion mechanisms need to induce a flow field and are therefore indirect interactions [117, 118]. Sometimes, activity is controlled by an external field, e.g., as a power supply, but – differently from passive colloids – the autonomous behavior of active particles requires internal degrees of freedom.

1.5.2 Particle transport

A common characteristic of particle transport situations is the existence of a particle flux, indicating that this system is in a non-equilibrium state. The fundamental equation to describe transport phenomena is the continuity equation

$$\frac{\partial \rho(\mathbf{r},t)}{\partial t} = -\nabla \cdot \mathbf{J}(\mathbf{r},t), \tag{1.6}$$

with $\rho(\mathbf{r},t)$ the particle density and $\mathbf{J}(\mathbf{r},t)$ the particle current. In simple words, this equation states that the change in ρ at any point in time and space is linked to a flux to or away from this point. Thus, the continuity equation (1.6) implies conservation of the total number of particles.

Two types of particle fluxes can be distinguished: diffusion and convection [16,119, 120]. In a diffusive process the particle density spreads into all spatial directions. According to Fick's first law [121], the diffusive flux is generated by inhomogeneity in the particle concentration. In the simplest situation a constant diffusion coefficient D is assumed and the diffusive flux is

$$\mathbf{J}_{\text{diff}}(\mathbf{r},t) = -D\nabla\rho(\mathbf{r},t). \tag{1.7}$$

This equation holds even in more complex situations where D is generalized to a spatial- or time-dependent diffusion coefficient or a tensor describing anisotropic diffusion [122, 123].

In a convection or advection process the particle density is displaced in the direction of the flow. Typical sources of convective transport are external force fields or interparticle interactions. The convective flux is simply given by the product of particle concentration and the particle velocity field

$$\mathbf{J}_{\text{conv}}(\mathbf{r},t) = \rho(\mathbf{r},t)\mathbf{v}(\mathbf{r},t). \tag{1.8}$$

Both types of current are present and relevant in transport situations of colloidal systems, i.e., $\mathbf{J} = \mathbf{J}_{\text{diff}} + \mathbf{J}_{\text{conv}}$. While diffusion tends to stabilize or restore equilibrium, convection generally distorts equilibrium. Steady state solutions are a balance between both competing transport phenomena which also determines the microstructure of the problem [16].

1.6 Theoretical framework

This section is about the dynamical density functional theory (DDFT), which is the theoretical framework used to analyze the colloidal systems of the papers in chapter 3. We explain some background information on the DDFT and sketch the main ideas of this theory. It is, however, not intended to be an exhaustive derivation of the theory; several excellent surveys can be found in the literature [24, 98, 124–131].

DDFT is a dynamical extension of (equilibrium) density functional theory (DFT). Therefore, first the concepts of DFT are introduced. A discussion of excess free energy functionals follows before, finally, moving on outlining the DDFT.

1.6.1 Density Functional Theory

Density functional theory (DFT) provides a framework to determine properties of equilibrium systems and was originally formulated for quantum mechanical systems. In 1964 Pierre Hohenberg and Walter Kohn [132] demonstrated that the one-particle electron density distribution $n(\mathbf{r})$ is sufficient to completely describe a many-body system. Furthermore, they proved that a unique energy functional $E[n]$ exists with two remarkable properties:

- The energy functional of the ground state one-particle density distribution $n_0(\mathbf{r})$ is the actual ground state energy E_0, i.e., $E[n_0] = E_0$.
- Any other density distribution $n(\mathbf{r}) \neq n_0(\mathbf{r})$ returns larger energy values, i.e., $E[n \neq n_0] > E_0$.

Thus, the ground state can be calculated by minimizing the functional $E[n]$, which is the key idea of DFT and marks its birth hour. David Mermin showed that the concept is also applicable to electron systems at finite temperature, i.e., that are not in the ground state [133]. Kohn developed this framework further together with Lu Jeu Sham [134] and was awarded with the Nobel Prize in Chemistry for his pioneering work on DFT in 1998 [135].

In the 1970s the quantum mechanical formulation was successfully transferred to classical systems by following Mermins approach [126, 136]. For classical systems a grand canonical functional $\Omega[\rho]$ can be found that depends on the ensemble averaged one-particle density

$$\rho(\mathbf{r}) = \left\langle \sum_{i=1}^{N} \delta(\mathbf{r} - \mathbf{r}_i) \right\rangle, \tag{1.9}$$

with $\langle \dots \rangle$ denoting the ensemble average and $\mathbf{r}_i$ the particle positions. The grand functional $\Omega[\rho]$ has the same properties as the energy functional in quantum DFT: the equilibrium one-particle density distribution $\rho_0(\mathbf{r})$ minimizes $\Omega[\rho]$ and recovers the actual grand canonical potential, i.e., $\Omega[\rho_0] = \Omega$.

The problem of finding the equilibrium configuration can thus be reformulated as the variational problem

$$\frac{\delta\Omega[\rho]}{\delta\rho(\mathbf{r})} = 0, \tag{1.10}$$

using the functional derivative $\frac{\delta}{\delta\rho(\mathbf{r})}$. The grand potential functional is given by

$$\Omega[\rho] = \mathcal{F}[\rho] - \mu \int \mathrm{d}^3\mathbf{r}\ \rho(\mathbf{r}), \tag{1.11}$$

with μ the chemical potential and the Helmholtz free energy functional

$$\mathcal{F}[\rho] = \mathcal{F}_{\mathrm{id}}[\rho] + \mathcal{F}_{\mathrm{exc}}[\rho] + \int \mathrm{d}\mathbf{r}\ \rho(\mathbf{r},t) V_{\mathrm{ext}}(\mathbf{r},t). \tag{1.12}$$

The first term on the right-hand side of eq. (1.12) is the *ideal gas* contribution which reads

$$\mathcal{F}_{\mathrm{id}}[\rho] = k_{\mathrm{B}}T \int \mathrm{d}\mathbf{r}\ \rho(\mathbf{r}) \big(\log(\Lambda^d \rho(\mathbf{r})) - 1 \big), \tag{1.13}$$

with $\Lambda = h/\sqrt{2\pi m}$ the thermal de Broglie wavelength and d the spatial dimension of the respective system. The second term, $\mathcal{F}_{\mathrm{exc}}[\rho]$, is the *excess free energy functional* which accounts for the interparticle contributions to the free energy. In general, no practical approach to express $\mathcal{F}_{\mathrm{exc}}$ is available, therefore sensible approximations are needed. Finding such an approximation is, in practice, the actual challenge in DFT and much effort has been made to construct excess functionals for various particle interactions [124, 125].

1.6.2 Excess Free Energy Functional

The excess Helmholtz free energy functional is an essential ingredient for both, DFT and DDFT. It describes contributions to the free energy beyond the ideal gas stemming from particle-particle interactions. First, the conceptual properties are shown before discussing various approaches to approximate $\mathcal{F}_{\mathrm{exc}}$.

Conceptually, the excess free energy functional is a generating functional, i.e., functional derivatives generate a hierarchy of *direct correlation functions* [98, 137]:

$$c^{(m)}(\mathbf{r}_1, \ldots, \mathbf{r}_m) = -\beta \frac{\delta^m \mathcal{F}_{\mathrm{exc}}[\rho]}{\delta\rho(\mathbf{r}_1)\ldots\delta\rho(\mathbf{r}_m)}. \tag{1.14}$$

These direct correlation functions play an important role in the functional Taylor expansion of $\mathcal{F}_{\mathrm{exc}}[\rho]$. Furthermore, from another branch of physics, namely liquid

state integral theory, fairly accurate approximations for direct correlation functions of *uniform* fluids are known.

In the past decades many approximations for the excess free energy functional $\mathcal{F}_{\text{exc}}$ have been proposed. Some approaches focus on a special type of particle interaction, others try to be applicable to various classes of interaction potentials.

One of the simplest approaches is to reduce the many-body problem to a one-body problem. In this so-called *mean field approximation* the pair interaction potential is integrated using the one-particle densities as weight functions [138–140]. The result is a mean field potential that averages the interactions of all particles, neglecting particle-particle correlations. This approximation is valid for very soft particle interactions or diluted systems for which particle correlations are weak. However, this approach diverges for most singular interaction potentials. Other notable attempts are the *weighted density approximation* [141–143] and its extensions [144]. These theories make use of weight functions to compute weighted densities that are being used to construct the excess free energy functional. Among the most successful approximations is the *fundamental measure theory* by Yaakov Rosenfeld [145] and its refinements [146, 147] which are valid for hard spheres. Its key idea is a decomposition of the particles to geometrical meaningful quantities that enter weight functions. Generalizations to hard core particles of arbitrary convex shape were successfully derived [87, 148].

One early and conceptually simple approximation is a perturbative expansion around a fluid reference state. This functional expansion in one-body density ρ, truncated at second order, has been studied first by Ramakrishnan and Yussouff [149–151] and yields

$$\mathcal{F}_{\text{exc}}[\rho] \approx \mathcal{F}_{\text{exc}}(\bar{\rho}_0) - \frac{k_{\text{B}}T}{2} \int \mathrm{d}\mathbf{r} \int \mathrm{d}\mathbf{r}' \, \Delta\rho(\mathbf{r}')\Delta\rho(\mathbf{r}) c_0^{(2)}(|\mathbf{r}-\mathbf{r}'|; \bar{\rho}_0). \tag{1.15}$$

Here, $\bar{\rho}_0$ is the density of a homogeneous reference fluid, $\Delta\rho(\mathbf{r}) = \rho(\mathbf{r}) - \bar{\rho}_0$ is the density difference to the reference state. The two-particle direct correlation function of a uniform fluid, $c_0^{(2)}(|\mathbf{r}-\mathbf{r}'|; \bar{\rho}_0)$, can be calculated from liquid state integral theory [98] and serves as an input parameter.

This approach is appealing due to its simplicity. The functional derivative of eq. (1.15) is a convolution of the density profile $\rho(\mathbf{r})$ and the two-particle direct correlation function,

$$\begin{aligned} \frac{\delta\mathcal{F}_{\text{exc}}[\rho]}{\delta\rho(\mathbf{r})} &= -k_{\text{B}}T \int \mathrm{d}\mathbf{r}' \, \rho(\mathbf{r}') c_0^{(2)}(|\mathbf{r}'-\mathbf{r}|; \bar{\rho}_0) \\ &= -k_{\text{B}}T (\rho * c_0^{(2)})(\mathbf{r}), \end{aligned} \tag{1.16}$$

which can be very efficiently computed via fast convolution algorithms in Fourier space. A disadvantage of this approximation is the relatively crude nature of this functional and its poor accuracy. It is therefore to be expected that not all features of the colloidal interplay are captured. The Ramakrishnan-Yussouff approximation

has been used in paper Paper II and Paper III to model the repulsive interaction of paramagnetic particles on a two-dimensional plane, see (1.5).

1.6.3 Dynamical Density Functional Theory

DFT has been successful in describing equilibrium states for different particle interactions, even in presence of an external potential. Yet, dynamical situations like crystal growth, phase transitions or steady states cannot be investigated via equilibrium DFT. Naturally, attempts have been made to extent DFT to a dynamical theory [152, 153]. In 1999, Umberto Marconi and Pedro Tarazona were the first to successfully formulate the dynamical DFT (DDFT) based on the Langevin equation [154]. Later, two alternative derivations were proposed, one starting from the Smoluchowski equation [155] and the other using the technique of projection operators [156]. These alternative approaches confirm the validity of DDFT and allow a different conceptual view of the theory and its limitations. Here, we sketch the derivation of DDFT by Archer and Evans [155], since it states very clearly at which points approximations are made.

As a starting point we consider the overdamped Smoluchowski equation [17, 67] – a Fokker-Planck equation for particle positions – that describes the time-evolution of a probability distribution $P(\mathbf{r}^N, t)$ of N particles at positions $\mathbf{r}^N = (\mathbf{r}_1, \ldots, \mathbf{r}_N)$ via

$$\frac{\partial P(\mathbf{r}^N, t)}{\partial t} = \frac{1}{\xi} \sum_{i=1}^{N} \nabla_i \cdot \left(k_\mathrm{B} T \nabla_i - \nabla_i (U(\mathbf{r}^N, t) - V_\mathrm{ext}(\mathbf{r}^N, t)) \right) P(\mathbf{r}^N, t), \tag{1.17}$$

with ∇_i the nabla operator with respect to $\mathbf{r}_i$, ξ the friction coefficient, and $U(\mathbf{r}^N, t)$ and $V_\mathrm{ext}(\mathbf{r}^N, t)$ the particle interaction and external potential, respectively.

For a multiparticle distribution, equation (1.17) is dependent on a large set of variables, namely $dN + 1$, with d the dimensionality of the system. In practice, one is rather interested in the probability distribution of finding *any particle* instead of the probability distribution of each *possible particle configuration*. The one-body density distribution $\rho(\mathbf{r}, t)$ addresses this consideration and is obtained via

$$\rho(\mathbf{r}, t) = N \int \mathrm{d}\mathbf{r}_2 \cdots \int \mathrm{d}\mathbf{r}_N \; P(\mathbf{r}, \mathbf{r}_2, \ldots, \mathbf{r}_N, t). \tag{1.18}$$

In a similar fashion, we define the two-particle density distribution

$$\rho^{(2)}(\mathbf{r}, \mathbf{r}', t) = N(N-1) \int \mathrm{d}\mathbf{r}_3 \cdots \int \mathrm{d}\mathbf{r}_N \; P(\mathbf{r}, \mathbf{r}', \mathbf{r}_3 \ldots, \mathbf{r}_N, t), \tag{1.19}$$

which is the probability density of any two particles being at position $\mathbf{r}$ and $\mathbf{r}'$ at time t. The definition of m-particle densities is straightforward.

For simplicity, we assume pairwise particle interactions in the following, i.e.,

$$U(\mathbf{r}^N, t) = \sum_{i,j;j<i} V_{\text{int}}(|\mathbf{r}_i - \mathbf{r}_j|), \tag{1.20}$$

but a treatment with full many-body interaction potentials is also possible [155]. Integrating both sides of the Smoluchowski equation (1.17) by $\int \mathrm{d}\mathbf{r}_2 \cdots \int \mathrm{d}\mathbf{r}_N \; P(\mathbf{r}^N, t)$ we obtain

$$\frac{\partial \rho(\mathbf{r}, t)}{\partial t} = D\nabla^2 \rho(\mathbf{r}, t) + \frac{1}{\xi}\nabla \cdot \left(\rho(\mathbf{r}, t) \nabla V_{\text{ext}}(\mathbf{r}, t) + \int \mathrm{d}\mathbf{r}' \; \rho^{(2)}(\mathbf{r}, \mathbf{r}', t) \nabla V_{\text{int}}(|\mathbf{r} - \mathbf{r}'|) \right). \tag{1.21}$$

Equation (1.21) is a partial differential equation in $\rho(\mathbf{r}, t)$ that requires knowledge of the time-dependent two-particle density $\rho^{(2)}(\mathbf{r}, \mathbf{r}', t)$.

It can be shown [98, 157] that the one- and two-particle densities of an *equilibrium* system are related via

$$-k_{\text{B}} T \rho(\mathbf{r}) \nabla c^{(1)}(\mathbf{r}) = \int \mathrm{d}\mathbf{r}' \; \rho^{(2)}(\mathbf{r}, \mathbf{r}') \nabla V_{\text{int}}(|\mathbf{r} - \mathbf{r}'|). \tag{1.22}$$

The so-called *adiabatic approximation* [158,159] assumes that the equilibrium relation (1.22) also holds in a *dynamical* context. As a more physical interpretation, the adiabatic approximation states that pair correlations relax much faster to the equilibrium configuration than the one-particle density [160]. Using equation (1.14) together with the adiabatic approximation, equation (1.21) becomes

$$\frac{\partial \rho(\mathbf{r}, t)}{\partial t} = D\nabla^2 \rho(\mathbf{r}, t) + \frac{1}{\xi}\nabla \cdot \left(\rho(\mathbf{r}, t) \nabla V_{\text{ext}}(\mathbf{r}, t) + \rho(\mathbf{r}, t) \nabla \frac{\delta \mathcal{F}_{\text{exc}}[\rho]}{\delta \rho(\mathbf{r}, t)} \right). \tag{1.23}$$

Additionally, the diffusion term $\nabla^2 \rho(\mathbf{r}, t)$ and the external potential can be expressed as

$$k_{\text{B}} T \nabla \rho(\mathbf{r}, t) = \rho(\mathbf{r}, t) \nabla \frac{\delta \mathcal{F}_{\text{id}}[\rho]}{\delta \rho \mathbf{r}, t}, \tag{1.24}$$

$$V_{\text{ext}}(\mathbf{r}, t) = \frac{\delta}{\delta \rho(\mathbf{r}, t)} \int \mathrm{d}\mathbf{r}' \; \rho(\mathbf{r}', t) V_{\text{ext}}(\mathbf{r}, t). \tag{1.25}$$

Thus, we obtain from eq. (1.23) the DDFT

$$\xi \frac{\partial \rho(\mathbf{r}, t)}{\partial t} = \nabla \cdot \left(\rho(\mathbf{r}, t) \nabla \frac{\delta \mathcal{F}[\rho]}{\delta \rho(\mathbf{r}, t)} \right), \tag{1.26}$$

with the Helmholtz free energy functional $\mathcal{F}[\rho]$, see eq. (1.12).

Eq. (1.26) is the standard DDFT which has first been derived [154,155] and is also employed in the papers of chapter 3. The standard DDFT has some limitations, e.g.,

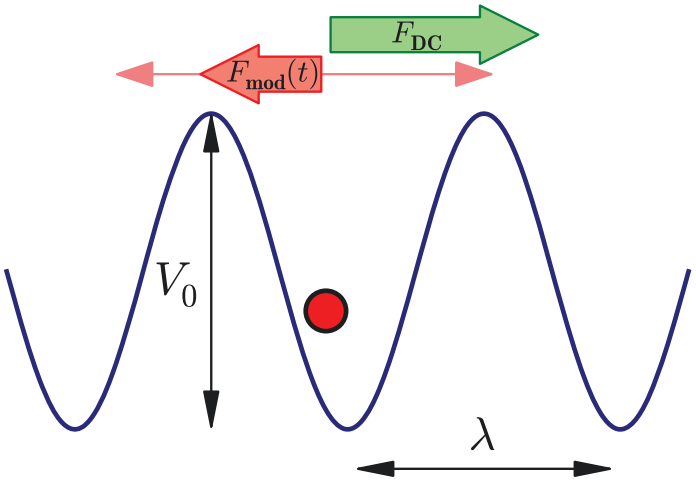

Abbildung 1.2: Sketch of the set-up in Paper I. A single colloidal particle in a sinusoidal energy potential landscape with amplitude V_0 and wavelength λ. The particle is subjected to a constant force F_{DC} (green arrow) and a modulated, time oscillating force $F_{\mathrm{mod}}(t)$ (red arrow).

no coupling to any flow field is included. We therefore limit ourselves to the study of direct external force fields in absence of hydrodynamic interactions. In principle, further elements can be included to the DDFT formalism, such as hydrodynamic interactions of the particles [161–163] or active drive in the case of self-propelled, active particles [163–166].

1.7 Outline of included scientific papers

The scientific publications included in chapter 3 explore various colloidal systems in non-equilibrium. This section gives an overview of the system set-ups used in the respective papers. Furthermore, we summarize the main results with a focus on the DDFT data. Finally, we comment on the scope of the publications in concluding remarks.

1.7.1 Mode locking in modulated system with periodic substrate potential

System

Paper I is a comprehensive study of the dynamics of a single particle – likewise, an ensemble of non-interacting particles – in an unbounded one-dimensional system. The dynamics of this setting are solely determined by the interplay of several external fields and thermal noise. The particle moves in a sinusoidal energy potential landscape with

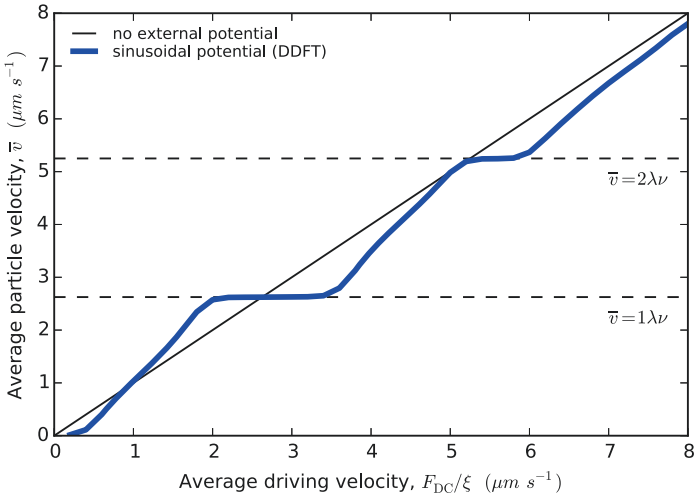

Abbildung 1.3: The time-averaged velocity $\bar{v}$ of the colloidal particle as a function of constant drive F_{DC} at fixed modulation amplitude $F_{\mathrm{AC}} = 5.2\,\mu$m/s and frequency $\nu = 0.75$ Hz. The blue curve is the average velocity calculated via DDFT. For comparison, we show the mean velocity of a particle in absence of the periodic potential landscape as the gray linear line. The dashed horizontal line at $\bar{v} = n\nu\lambda$, $n = 1, 2, \ldots$ indicate the discrete levels in mean velocity of the mode locked plateaus.

amplitude V_0 and wavelength λ. Additionally, an external driving force $F(t)$ acts on the particle, consisting of two components: a constant part F_{DC} and a time-modulated, oscillating part $F_{\mathrm{mod}}(t) = F_{\mathrm{AC}}\cos(2\pi\nu t)$ with F_{AC} the amplitude and ν the frequency of the modulated drive, see figure 1.2 for a sketch of the system. All external fields are direct interactions that do not affect the suspension medium. Note, that in this study the DDFT is equivalent to the Smoluchowski equation due to the absence of interparticle interactions and correlations.

Results

The modulated driving force $F_{\mathrm{AC}}\cos(2\pi\nu t)$ is an external stimulus that competes with the intrinsic frequency of periodic motion of the driven particle along the potential landscape. A matching of external and intrinsic frequencies result in a synchronization that divides the particle motion into modes of discrete motion properties. Within one oscillation cycle the particle travels an integer number of potential minima back and forth. This effect of synchronization is known as mode locking and it manifests in numerous ways.

Considering the time-averaged velocity of the particle as a function of the constant drive F_{DC}, we notice a step-like behavior, see figure 1.3. The curve of the average velocity is called ‘devil’s staircase’ or ‘Shapiro steps’. The levels of the plateaus at the

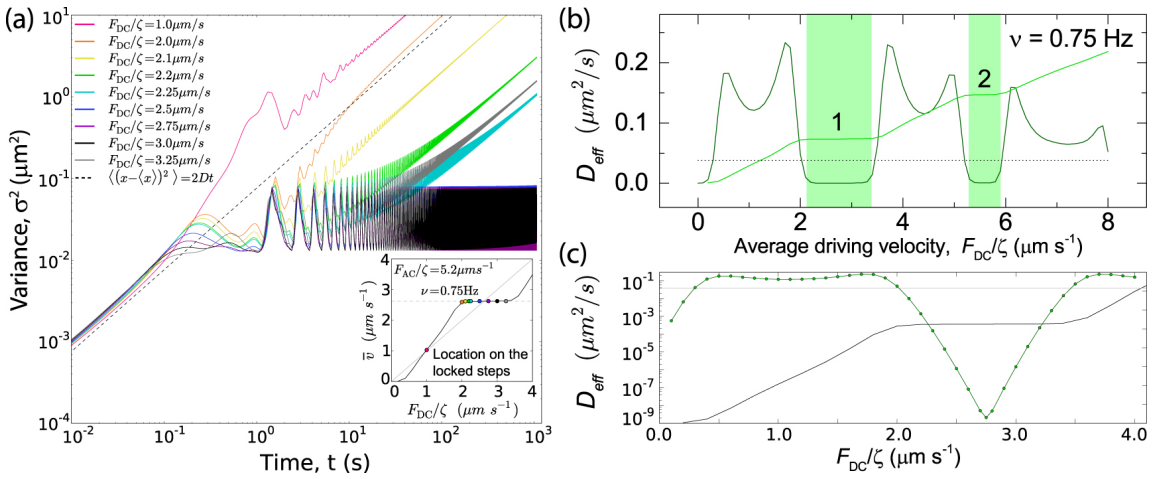

Abbildung 1.4: DDFT results for variance and effective long-time diffusion D_{eff} for various constant drives F_{DC} at fixed modulation amplitude $F_{\text{AC}} = 5.2\,\mu\text{m/s}$ and frequency $\nu = 0.75$ Hz. (a) Double logarithmic plot of the time evolution of the variance for different F_{DC}. The color codes of the curves refer to the respective state points on the devil's staircase shown in the inset. The dashed black line refers to a free colloidal particle, i.e., in absence of the external potential. (b) Effective long-time diffusion coefficients D_{eff} in dependence on the constant drive F_{DC} (dark green curve). The devil's staircase is shown as a light green curve but does not match to the scale of the y-axis. For comparison, the dotted black line shows the diffusion coefficient of a free particle. Green colored areas highlight the range of different mode locked configurations. (c) Log scaled plot of D_{eff} (see panel (b)) zoomed to the first step. Reproduced from Paper I.

devil's staircase are at $\bar{v} = n\nu\lambda$, $n = 1, 2, \ldots$ and are characteristic for particles in a mode locked state. A mode locked particle is forced to move only an integer number of potential minima in one oscillation cycle of the modulated force. Thermal motion disturbs the synchronized movement pattern, therefore the plateaus are not completely flat. The nearly linear increase in average velocity that connects the plateaus marks unlocked configurations in which the particle does not move periodically.

To further analyze the influence of thermal motion we consider the variance of the particle distribution

$$\sigma^2(t) = \langle [x(t) - \langle x \rangle(t)]^2 \rangle \tag{1.27}$$

as a measure of fluctuations with $x(t)$ the particle position at time t and $\langle \ldots \rangle$ the average. Figure 1.4 (a) displays how the variance at various states on the devil's staircase spreads in time, compared to a freely diffusing particle with $D = k_{\mathrm{B}}T/\xi$. The unlocked configurations show enhanced diffusivity whereas mode locked states remain on a long-lived plateau.

The increase in variance can be extrapolated to extract an effective long-time diffusion coefficient

$$D_{\mathrm{eff}} = \lim_{t\to\infty} \frac{\sigma^2(t)}{2t}, \tag{1.28}$$

which describes diffusion on a coarse-grained time and length scale. The fingerprint of mode locking can also be identified in the effective long-time diffusion D_{eff}. Figure 1.4 (b) displays D_{eff} for the range of the staircase. On the one hand, D_{eff} becomes very large for unlocked states, especially in states close to the mode locked regime. On the other hand we note an extreme decrease of D_{eff} in the mode locked regime. Figure 1.4 (c) emphasize this decrease by showing a logarithmic scaled y-axis, indicating that effective diffusion (i.e., away from the prescribed potential minimum) basically vanishes.

Being able to detect mode locking either by a periodic movement pattern of the particle or by dramatically decreased effective long-time diffusion, we investigate the synchronization with respect to various parameter combinations. In figure 1.5 (a) the amplitudes of both driving force components, F_{DC} and F_{AC}, are scanned at fixed modulation frequency and in figure 1.6 a state diagram of modulation frequency ν and constant drive F_{DC} is displayed for different fixed modulation amplitudes F_{AC}. The coloring in these figures highlight the respective mode, i.e., the netto number of potential minima a particle is displaced in each cycle. The effective long-time diffusion coefficient D_{eff}, showed in figure 1.5 (b), is especially large if the particle is at the border between a mode locked and an unlocked state. In this region, thermal motion becomes influential and can easily kick the particle out of a synchronized motion.

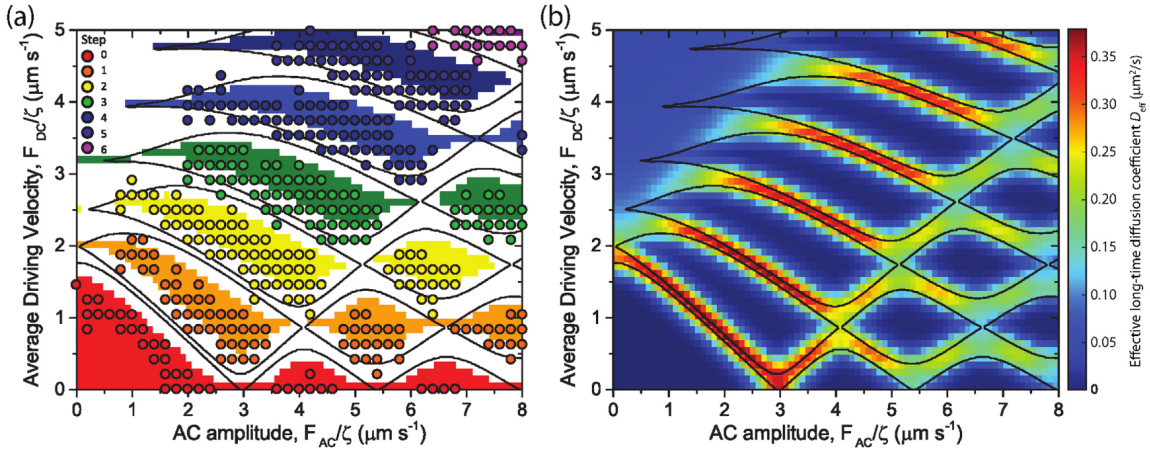

Abbildung 1.5: State diagram and variance for a range of constant drives F_{DC} and modulation amplitudes F_{AC} at fixed modulation frequency $\nu = 0.25$ Hz. (a) Mode locked states colored according to the number of potential minima travel in each modulation cycle. The background coloring is data from DDFT, colored circles are experimental datapoints, and black curves mark the border between locked and unlocked states calculated by simulations without thermal noise. The white areas refer to unlocked states. (b) Effective long-time diffusion coefficient D_{eff} calculated by DDFT and displayed via the color scale. Black curves represent borders between locked and unlocked state in absence of thermal noise, see (a). Reproduced from Paper I.

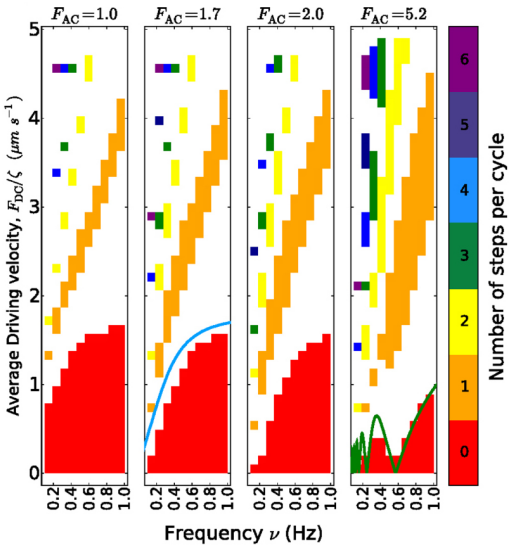

Abbildung 1.6: State diagram shows mode locked states in dependence on modulation frequency ν and constant driving force F_{DC} for various fixed modulation amplitudes F_{AC}. The color coding refers to the number of potential minima traveled in each modulation cycle, see figure 1.5 (a). Reproduced from Paper I.

Conclusions

We studied extensively how the particle motion is being influenced by various parameters of the external driving force. For certain combinations of constant drive F_{DC}, modulation amplitude F_{AC}, and modulation frequency ν mode locking happens, i.e., the particle movement synchronizes to a discrete mode. In the mode locked state the particle is trapped in a predominantly deterministic motion with a well-defined, discretized mean velocity. Furthermore, the effective long-time diffusion coefficient D_{eff} nearly vanishes, meaning that a particle in a thermal environment behaves in a nearly deterministic way. However, this can be changed by manipulating the driving force, either the constant force F_{DC}, the modulation amplitude F_{AC}, or the modulation frequency ν. This facilitates a precise control via external tuning of the transport behavior of a single particle.

1.7.2 Constricted microchannel

System

In Paper II we study a two-dimensional system of colloidal particles interacting via a repulsive dipolar potential, see eq. (1.5). The strength of the repulsive particle

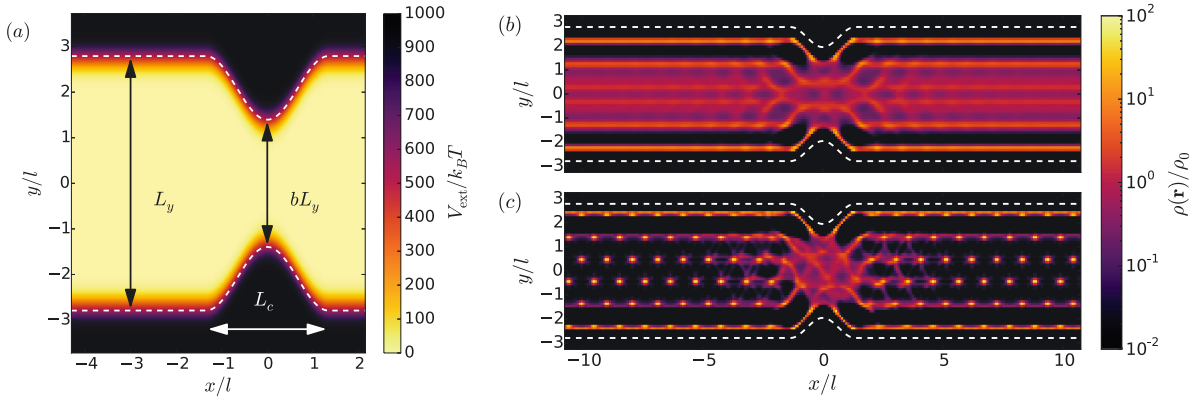

Abbildung 1.7: (a) Potential energy of the channel confinement with maximum potential height V_0, channel width L_y, lateral constriction length L_c and constriction width bL_y (here, $b = 0.5$). The white dashed lines mark the contour of the confinement at $V_0/2$. (b), (c) Snapshots of the one-particle density profile for (b) low particle interaction strength ($\Gamma = 20$, fluid) and (c) high interaction strength ($\Gamma = 60$, solid). The channel width L_y is chosen so that six particle layer fit into the confinement. The parameter of the constriction width is chosen as $b = 0.7$. White dashed lines display the profile of the confinement potential. Reproduced from Paper II.

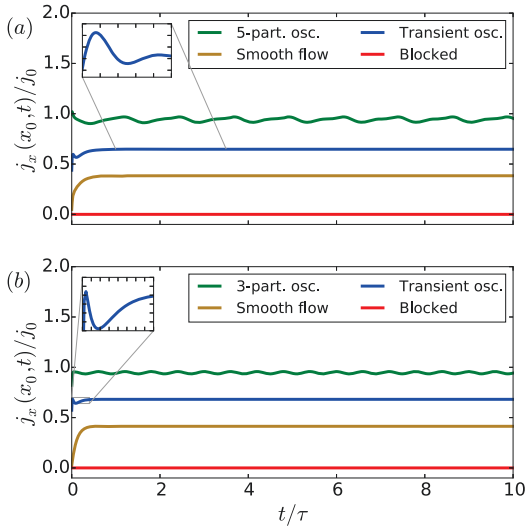

Abbildung 1.8: Particle flux along the channel relative to the flux j_0 of an unconstricted channel as a function of time in terms of Brownian times τ for channel widths L_y suitable to fit five (a) and six (b) particle layers in the channel. The driving force $F = 1k_BT/l$ has been switched on at $t = 0$ initiating the flow. The colored curves in each panel represent the various flow patterns and are obtained for different combinations of interaction strength Γ and constriction parameter b: top, green curve is for $\Gamma = 30$, $b = 0.9$, the other curves are for $\Gamma = 20$ and $b = 0.6, 0.3, 0.2$ (from top to bottom). Reproduced from Paper II.

interaction is characterized by the dimensionless coupling parameter Γ. The particles are confined in a microchannel that can support or hinder the emergence of an ordered phase and strongly influences its stability. In addition, a constriction is introduced into the channel that forces a re-ordering of the particle configuration. The open ends of the channel are connected via periodic boundary conditions. The confinement potential is depicted in figure 1.7 (a). Starting from an equilibrium configuration, we switch on a constant driving force F along the channel acting directly on the colloids. This sudden switch generates a particle flow that drives the system out of equilibrium. Two different channel widths are investigated, in which in the crystalline phase five and six layers fit, respectively. Within the DDFT we use the Ramakrishnan-Yussouff approach to incorporate particle-particle interactions. Typical snapshots of the one-particle density field are shown in figure 1.7 (b) for weak particle interactions (fluid state) and (c) for strong particle interactions (solid state).

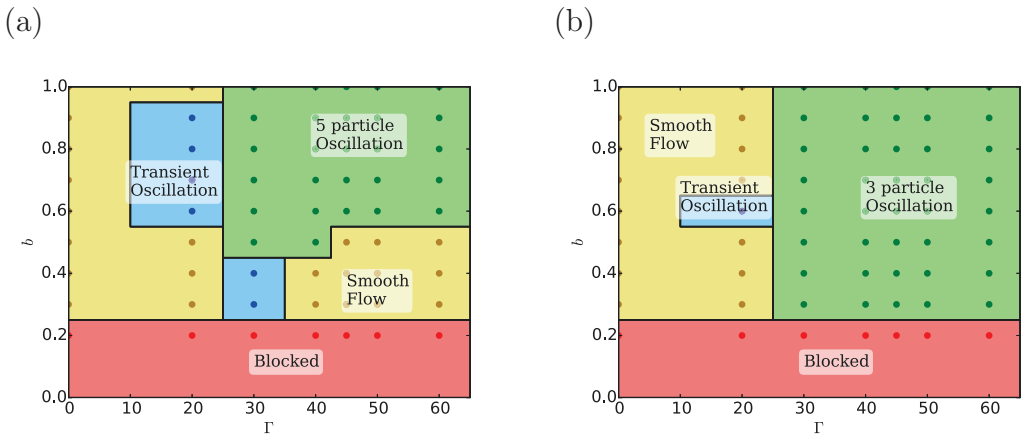

Abbildung 1.9: State diagram indicating the type of flow pattern for both channel widths that fit to (a) five particle layers and (b) six particle layers. Dark colored points are the indicate where the calculations were performed. Reproduced from Paper II.

Results

We study in which way the particle flow is affected by the width of the geometrical constriction in combination with the strength of the particle interaction. Upon switching on the driving force F, we observe four qualitatively different flow patterns.

Complete blockade: No particle flux occurs.

Smooth flow: After switching on the drive, the flux quickly converges to a constant level of particle flow.

Transient oscillation: The particle flux performs a damped, transient oscillation that converges to a constant level of particle flow.

Persistent oscillation: An undamped oscillation in the particle flow occurs. Depending on the number of particle layers (i.e., five or six layers), a qualitative difference is observable. For five particle layers the frequency of the oscillation is lower and on average five particles pass the constriction in a single oscillation cycle. In the case of six particle layers we notice a higher oscillation frequency with three particles crossing on average the constriction in a single oscillation cycle.

Figure 1.8 displays examples of the four flow patterns in a five and six layer channel system. Also, state diagrams of the respective flow patterns in dependence on particle interaction strength and constriction width are presented in figure 1.9.

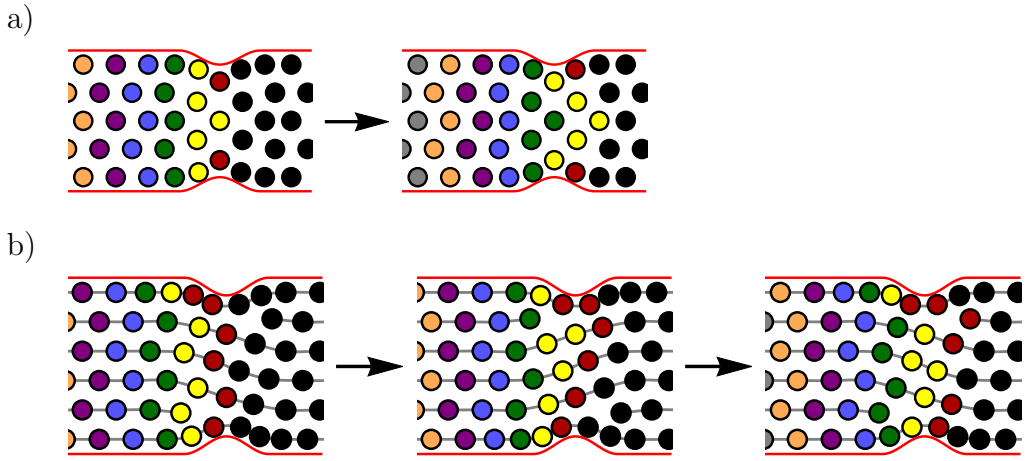

Abbildung 1.10: Schematic picture of the persistent oscillating flow observed for high interaction strength Γ and wide constrictions (large b). The figures are idealized snapshots of the system separated in time by exactly one oscillation period. Flow is from left to right. **(a)** For a channel width in which five crystal layers form, and one oscillation corresponds to the movement of the crystal by one lattice spacing. During this time, each particle assumes the position of the particle in front of it. **(b)** For a crystal with six layers, one oscillation period corresponds to the movement of the crystal by half of a lattice spacing. Note that in the case of six layers, the up-down symmetry in the system is broken, and we observe two symmetric dislocations in the crystal pattern, as indicated by the gray lattice lines. After one oscillation, the locations of the particles (and dislocations) are vertically mirrored with respect to the initial configuration (middle snapshot). After the next oscillation (right snapshot), we recover the original configuration. Reproduced from Paper II.

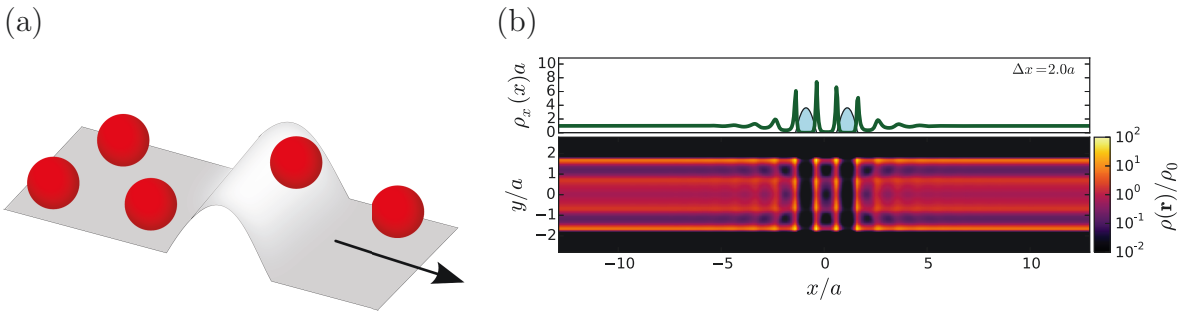

Abbildung 1.11: (a) Sketch of colloidal particles that cross a physical barriers. The arrow indicates the direction of driving force acting on the particles. (b) Snapshot of the one-particle density profile in presence of two potential barriers separated by distance $\Delta x = 2a$. Particle interaction strength is $\Gamma = 5$ at a weak driving force $F = 0.1 k_\mathrm{B}T/a$. The lower panel shows the two dimensional particle density with a logarithmic scaled colorbar. The upper panel displays the density as a projection on the x-axis (green curve). The barrier potentials are illustrated as black curves with blue filling and do not fit to the y-axis scale.

The qualitative difference in the persistent oscillation regime with respect to the two channel widths is further investigated. We can understand this effect by the up-down symmetry of the particle layers. If up-down symmetry is given, the whole particle layer in front of the constriction is being pushed through, see figure 1.10 (a). However, for an inverted up-down symmetry the process has two different stages before the initial configuration is recovered. The cartoon in figure 1.10 (b) depicts this three-particle oscillation process.

Conclusions

This study shows the interplay of a geometrical constriction with the interaction strength of the particles and the influence on the particle flow behavior. Most flow patterns relax to a steady state flow after a transient phase. However, the three- and five-particle oscillation is a dynamical flow pattern that remains persistent, although all external fields are independent of time.

1.7.3 Barrier obstacles in microchannel

System

The set-up of Paper III is a two-dimensional straight microchannel in which repulsive dipolar colloidal particles (see eq. (1.5)) are confined. The particles are subjected to a constant external driving force F generating a particle flow. Periodic boundary

conditions connect both open ends of the channel system. Up to two energetic barrier potentials are introduced in the channel. These obstacles can be overcome by the colloids, but some activation energy is required. The barriers reduce the particle flow, i.e., they impose a resistance to the flow. In order to test whether the resistances of two barriers are additive, we compare set-ups with a single barrier to systems with two barriers in various configurations and determine the overall resistance. Furthermore, we apply driving force of different strengths. In the DDFT framework the interparticle interactions are described using the Ramakrishnan-Yussouff approximation for the excess free energy functional. In the case of non-interacting colloidal particles we can find an analytical solution which is presented in an analytical study in chapter 2.

Results

To analyze the effect of introducing a second barrier into the microchannel we first calculate the resistance R_1 imposed by a single barrier which is linked to the steady state flux j_1 along the channel. The added resistance R_2 of the second barrier is determined by the difference in the steady state flux j_2 of the two barrier system compared to the one barrier system. Additivity of barrier resistances is given if $R_1 = R_2$. Clearly, as the separation distance Δx of the barriers becomes large, additivity is expected while a violation of additivity is apparent for small Δx.

Figure 1.12 shows R_2 relative to R_1 as a function of barrier separation distance Δx for various drives F. Interestingly, even for non-interacting particles (ideal gas) the resistances of the barriers are not additive, see figure 1.12 (a). To explain this effect we consider a particle in front of a single barrier with a driving force that is not strong enough the push it over the obstacle. The particle may cross the barrier only by thermal transport, i.e., diffusion. In this setting, we assume isotropic diffusion, meaning that the particle can diffuse over the barrier or away from it, even though the drive F adds a bias to the overall transport direction. Now we consider a particle trapped in the middle of two barriers at close distance. Similarly to the previous setting, the particle has to diffuse over the second obstacle but in this case the range the particle can diffuse away from the second barrier is limited by the first barrier. This limitation of transport away from the second barrier enhances the probability to cross it. Therefore, non-additivity of barrier resistances at short distances with non-interacting particles is governed by the relation of diffusion to driving force F. With increasing barrier separation distance Δx the added resistance of the second barrier R_2 converges exponentially to R_1, establishing additivity. A detailed analysis of this system with analytical solutions is presented in chapter 2.

Figure 1.12 (b) displays the quotient R_2/R_1 for a range of barrier separation distances Δx for the case of repulsive particles. In contrast to non-interacting particles, R_2 is a decaying oscillation around R_1 for repulsive particles eventually approaching R_1 at large separation distances. Consequently, depending on the barrier separation distance, the resistances are either superadditive or subadditive. Changing the posi-

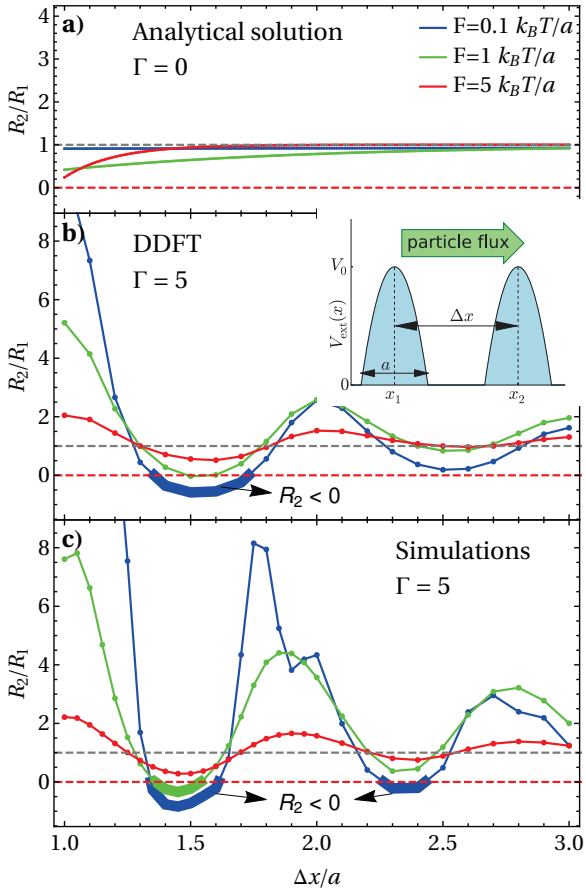

Abbildung 1.12: Resistance added by the second barrier R_2 relative to the resistance of the first barrier as a function of the barrier separation distance Δx at different driving forces for (a) non-interacting particles (analytical results), (b) DDFT calculations ($\Gamma = 5$), and (c) computer simulations ($\Gamma = 5$). Horizontal dashed lines mark special values: gray line indicates additivity and the red line is the onset of negative effective resistance. Negative effective resistance is highlighted by a thicker line section. Reproduced from Paper III.

tion of the second barrier relative to the first one can thus significantly increase or decrease the total resistance of the system.

A remarkable effect that can be observed for specific combinations of barrier separation distance and driving force is an effective negative resistance added by the second barrier. This means that a second potential barrier – if placed in the right spot – reduces the overall resistance of the system. A closer analysis of this phenomenon reveals that each barrier enforces an ordering in the colloidal fluid. This way, the average particle density is enhanced in some distances from the barrier and decreased in other places. Separating the barriers at a distance that does not fit this ordering leads to fluctuations in the particle density between the barriers and allows an enhanced crossing of barriers driven by these fluctuations.

Conclusions

In this simple setting we investigated the added resistance of two barriers and we found strong violations of additivity at distances comparable to the correlation length of the particles. While non-additivity in ideal gas setting can easily be understood by a competition of diffusion and driving force, we find ourselves faced to a considerably more complex situation when using interacting particles. The added resistance R_2 can either be much larger or smaller than R_1. Even the case of negative added resistance could be demonstrated which is of particular interest to colloidal applications as well as for comparable situations where an unavoidable resistance can effectively be lowered by placing a second obstacle in the right spot. Paper III is a study of just two identical potential barriers. More complex set-ups can are imaginable using multiple or differently shaped barriers that exploit the effect of effective negative resistance more efficiently.

1.7.4 Concluding remarks

The scope of this thesis is to investigate various colloidal systems in non-equilibrium, invoked by external force fields and using the DDFT as a theoretical framework. Three studies of colloidal systems are therefore presented in chapter 3, all of them analyzing non-equilibrium systems. Non-equilibrium is constituted by applying an external force, acting directly on the colloids while leaving the suspension at rest.

To study systems out of equilibrium, we first consider both categories of complexity: complexity of the system and complexity of the problem [25]. In the first study we reduce the complexity of the system by considering a single particle in one spatial dimension. However, the complexity of the problem is therefore high: periodic energy potential landscape, constant and time-modulated driving force. We can study the velocity and diffusion of that particle which is influenced by synchronization effects.

In the second study the complexity of the problem is reduced as there is no time-dependent external force field and apart from the constant drive we only consider a

geometrical confinement. Yet, we increase the complexity of the system by introducing particle-particle interactions and consider a two-dimensional system. Here, the focus lies on the flow behavior that emerges for various system parameters and the transient phase that converges to a steady state. Interestingly, although no external time dependency is present, we find a regime of persistent oscillation in the flow.

The set-up of the third study is similar to the second one, using as well repulsive dipolar particles in a two-dimensional microchannel confinement. Instead of constricting the confinement, we placed up to two energetic potential barriers in the channel that invoke a resistance to the steady state particle flow. We investigated the added resistance of various potential barrier configurations and found the overall resistance to be very sensitive to the separation distance of the barriers if it is comparable to the particle correlation length.

All presented studies demonstrate how the transport behavior of the colloidal suspension in these non-equilibrium systems can be dramatically changed by manipulating the external field. This property is important for many applications of colloidal suspensions because of the ability to dynamically tune a system.

2 Analytical study

In Paper III we tested additivity of resistances imposed by obstacles for colloids with repulsive particle-particle interactions. This analytical study considers the same set-up except for a fluid of ideal gas instead of interacting particles. Notably, this setting exhibits an analytical solution as demonstrated in this chapter.

2.1 Set-up

This section is a brief review of the settings used in this chapter. We consider non-interacting colloidal particles confined in a two-dimensional microchannel of width L_y. In this study we take into account two different boundary conditions: periodic boundaries and an infinite system. Both types are being discussed in section 2.5.

Obstacles are being introduced into the channel which we model as parabola shaped external potentials

$$V_{\text{ext}}(\mathbf{r}) \equiv V_{\text{ext}}(x) = \begin{cases} V_0 \left(1 - \left(\frac{x-x_0}{\lambda}\right)^2\right), & |x - x_0| < \lambda \\ 0, & |x - x_0| \geq \lambda \end{cases}, \tag{2.1}$$

with V_0 the height, λ the width, and x_0 the center of the barrier. Finally, a constant driving force $\mathbf{F} = F\hat{\mathbf{x}}$ acts on the colloids to generate a particle flow along the channel.

2.2 Governing differential equation

In this section we derive the differential equation that describes the steady state situation and adopt some simplifications to reduce the complexity of the problem.

2.2.1 Steady state equation

Starting from the continuity equation (1.6) and identifying the particle flux $\mathbf{J}$ with the right hand side of the DDFT (1.26) yields

$$\frac{\partial \rho}{\partial t} = -\nabla \cdot \mathbf{J} \tag{2.2}$$

where

$$\mathbf{J}(\mathbf{r}, t) = -D \left\{ \nabla \rho(\mathbf{r}, t) + \beta \rho(\mathbf{r}, t) [\nabla V_{\text{ext}}(\mathbf{r}, t) - F\hat{\mathbf{x}}] \right\}. \tag{2.3}$$

Note, the absence of the excess free energy function, $\mathcal{F}_{\text{exc}} \equiv 0$, due to non-interacting particles.

We are interested in the steady state in which the density profile is independent on time, i.e., $\frac{\partial \rho}{\partial t} = 0$. The left hand side of eq. (2.2) is zero, thus, integrating the continuity equation we obtain an inhomogeneous differential equation of first order,

$$\mathbf{J}(\mathbf{r}, t) \equiv \mathbf{J}_0 = D \left\{ \beta \rho(\mathbf{r}, t) [F \hat{\mathbf{x}} - \nabla V_{\text{ext}}(\mathbf{r}, t)] - \nabla \rho(\mathbf{r}, t) \right\}, \tag{2.4}$$

with constant steady state particle flux $\mathbf{J}_0$.

2.2.2 Reduction to one dimension

We choose the coordinate system in the middle of the channel such that the x-axis points along the channel and the channel walls are at $\pm L_y/2$. Note, that the non-confining external potential barriers in eq. (2.1) are not dependent on the y-direction. Since there are no particle-particle interactions, the density profile of the colloidal suspension is flat in y-direction inside the channel, i.e.,

$$\rho(x, y) = \begin{cases} \rho(x, 0) & \text{, if } -\frac{L_y}{2} \leq y \leq \frac{L_y}{2} \\ 0 & \text{, otherwise} \end{cases}. \tag{2.5}$$

Therefore, we can reduce the spatial dimension of the two-dimensional equation (2.4) to one dimension by integrating out the y-dependence via $\int \mathrm{d}y\, \hat{\mathbf{x}}$. The reduced differential equations reads

$$J_0 = D \left\{ \beta \rho(x) \left[F - \frac{\partial V_{\text{ext}}(x)}{\partial x} \right] - \frac{\partial \rho(x)}{\partial x} \right\}, \tag{2.6}$$

with one-dimensional particle density $\rho(x) = \int \mathrm{d}y\, \rho(\mathbf{r})$ and $J_0 = \int \mathrm{d}y\, \hat{\mathbf{x}} \cdot \mathbf{J}_0$ the total flux along the channel.

2.2.3 Dimensional analysis

For a less verbose notation and a simplified analysis we perform a non-dimensional scaling. Thus, we transform quantities with a physical dimension to dimensionless quantities. First we express all relevant quantities in terms of

- length l
- diffusion coefficient D
- thermal energy $k_{\text{B}}T$.

With these scales we can express the following quantities as:

$$x = lx^*, \qquad E = k_\mathrm{B}TE^*, \qquad \rho = \frac{\rho^*}{l}, \tag{2.7}$$

$$t = \frac{l^2}{D}t^*, \qquad F = \frac{k_\mathrm{B}T}{l}F^*, \qquad J = \frac{D}{l^2}J^*, \qquad \lambda = l\lambda^*, \tag{2.8}$$

with 'starred' quantities being non–dimensional. A rephrasing of equation (2.6) yields

$$\frac{D}{l^2}J_0^* = D\left\{\frac{1}{k_\mathrm{B}T}\frac{\rho^*(x^*)}{l}\left[\frac{k_\mathrm{B}TF^*}{l} - \frac{k_\mathrm{B}T}{l}\frac{\partial V_\mathrm{ext}^*(x^*)}{\partial x^*}\right] - \frac{1}{l^2}\frac{\partial\rho^*(x^*)}{\partial x^*}\right\} \tag{2.9}$$

$$\Rightarrow \qquad J_0^* = \rho^*(x^*)\left(F^* - \frac{\partial V_\mathrm{ext}^*(x^*)}{\partial x^*}\right) - \frac{\partial\rho^*(x^*)}{\partial x^*} \tag{2.10}$$

From here on, the 'starred' notation is dropped for convenience and all following calculations always refer to non-dimensional quantities.

2.2.4 Resulting differential equation

Introducing the effective force $f(x) = F - \frac{\partial V_\mathrm{ext}(x)}{\partial x}$, the final differential equation that describes the density profile of the colloidal suspension in steady state for arbitrary x-dependent external potentials reads

$$\frac{\partial\rho}{\partial x} - f(x)\rho = -J_0, \tag{2.11}$$

which is an inhomogeneous ordinary linear differential (ODE) equation of first order.

2.3 General solution of the differential equation

In this section we find the general solution of differential equation (2.11) that is independent of boundary conditions. The strategy to solve an inhomogeneous ODE is to find a solution of the homogeneous part and a specific solution for the inhomogeneous ODE. The general solution is then a linear combination of the homogeneous and the inhomogeneous solution.

2.3.1 Homogeneous solution

The homogeneous equation is

$$\frac{\partial\rho}{\partial x} - f(x)\rho = 0, \tag{2.12}$$

which can be easily solved using the separation of variables technique. The corresponding solution is

$$\rho_\mathrm{hom}(x) = \mathcal{C}_0 e^{\int^x \mathrm{d}x'\, f(x')}, \tag{2.13}$$

with $\mathcal{C}_0$ the constant of integration that is not yet determined.

2.3.2 Inhomogeneous solution

The solution to the full inhomogeneous ODE (2.11) can be found by using the homogeneous solution $\rho_{\text{hom}}(x)$ and perform a variation of parameters using

$$\rho_{\text{in}}(x) = \mathcal{C}_0(x) e^{\int^x \mathrm{d}x' \, f(x')}. \tag{2.14}$$

Putting $\rho_{\text{in}}(x)$ into the differential equation (2.11) yields:

$$\mathcal{C}_0(x) = -J_0 \int^x \mathrm{d}x' \; e^{-\int^{x'} \mathrm{d}x'' \, f(x'')}. \tag{2.15}$$

Thus, the inhomogeneous solution is:

$$\rho_{\text{in}}(x) = -J_0 e^{\int^x \mathrm{d}x' \, f(x')} \int^x \mathrm{d}x' \; e^{-\int^{x'} \mathrm{d}x'' \, f(x'')}. \tag{2.16}$$

2.3.3 General solution

The general solution is simply a superposition of the homogeneous and the inhomogeneous solution.

$$\begin{aligned} \rho(x) &= \mathcal{C}_0 e^{\int^x \mathrm{d}x' \, f(x')} - J_0 e^{\int^x \mathrm{d}x' \, f(x')} \int^x \mathrm{d}x' \; e^{-\int^{x'} \mathrm{d}x'' \, f(x'')} \\ &= e^{\int^x \mathrm{d}x' \, f(x')} \left\{ \mathcal{C}_0 - J_0 \int^x \mathrm{d}x' \; e^{-\int^{x'} \mathrm{d}x'' \, f(x'')} \right\}. \end{aligned} \tag{2.17}$$

2.4 Average passing time and resistance

The barrier potentials in the channel impede the particle flux, thus causing a resistance. To quantify the resistance we consider the average time T it takes a particle to move from one point to another. In steady state the particle flux $J_0 = \rho(x)\langle v(x)\rangle$ is constant with $\langle v(x)\rangle$ the average velocity of a particle. We can express the passing time via

$$\begin{aligned} T &= \int_{t_1}^{t_2} \mathrm{d}t \; = \int_{x_1}^{x_2} \mathrm{d}x \frac{\mathrm{d}t}{\mathrm{d}x} = \int_{x_1}^{x_2} \mathrm{d}x \; \frac{1}{\langle v(x)\rangle} \\ &= \frac{1}{J_0} \int_{x_1}^{x_2} \mathrm{d}x \; \rho(x). \end{aligned} \tag{2.18}$$

The resistance of any barrier configuration can be quantified by the *additional* time $\Delta T = T - T_0$ a particle needs to cross the obstacles (T), compared to a system without barriers (T_0).

2.5 Boundary Conditions

Boundary conditions have to be specified to determine the constant of integration $\mathcal{C}_0$ in the general solution. Moreover, they also incorporate topological information of the system. In the scope of this study we consider two different boundary conditions: an infinite and a periodically repeated system. Our aim is to investigate whether there is a qualitative difference in the solutions of the two discussed boundary conditions.

2.5.1 Infinite system

Assuming that the microchannel is very long we can describe it as an infinite system. In this picture, we propose that the density far away from the potential barriers is of a finite value ρ_0,

$$\lim_{x\to\pm\infty} \rho(x) = \rho_0. \tag{2.19}$$

Note, in this description the overall particle number is not conserved. As another consequence the steady state particle flux J is identical for all systems irrespective of the barrier configurations, i.e. $J \equiv J_0 = \rho_0 F$. The resistance in an infinite system according to eq. (2.18) is given by

$$\begin{aligned} \Delta T_\infty = T - T_0 &= \frac{1}{J_0}\int_{x_1}^{x_2} \mathrm{d}x\ \rho(x) - \frac{1}{J_0}\int_{x_1}^{x_2} \mathrm{d}x\ \rho_0 \\ &= \frac{1}{J_0}\int_{x_1}^{x_2} \mathrm{d}x\ (\rho(x) - \rho_0). \end{aligned} \tag{2.20}$$

This means the resistance in an infinite system is determined by the *excess* density over ρ_0.

2.5.2 Periodic Boundary Conditions

Periodic boundary conditions are for technical reasons more favorable in computation and therefore being used in the numerical implementations of the DDFT in Paper II and Paper III. For a periodic system of length L we require the following two properties for the density profile $\rho(x)$:

$$\rho(0) = \rho(L), \tag{2.21}$$

$$\frac{1}{L}\int_0^L \mathrm{d}x\ \ \rho(x) = \rho_0. \tag{2.22}$$

Note, that by (2.22) the total number of particles $N = \rho_0 L$ is conserved. This implicates an expression for the delay time ΔT_P that is different to ΔT_∞ of an infinite

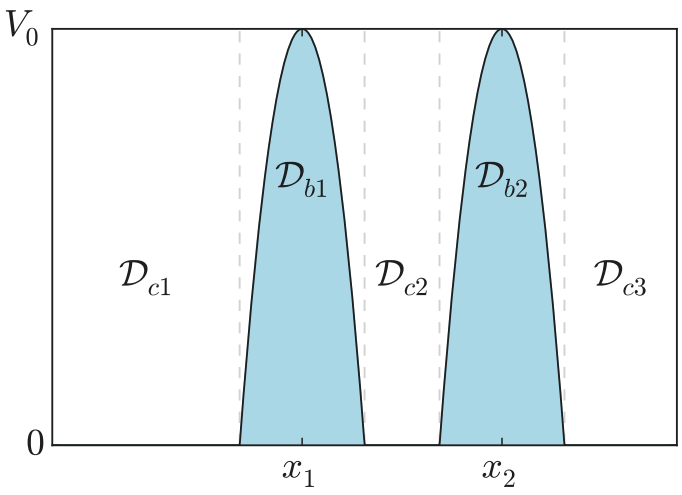

Abbildung 2.1: System with two potential barriers. The decomposition of the system into five domains is shown: two domains defined by the range of the potential barrier and three channel domains.

system. For periodic boundaries, the steady state particle flux varies for different barrier configurations and the delay time reads

$$\begin{aligned} \Delta T_P = T - T_0 &= \frac{1}{J}\int_{x_1}^{x_2} \mathrm{d}x\ \rho(x) - \frac{1}{J_0}\int_{x_1}^{x_2} \mathrm{d}x\ \rho_0 \\ &= L\rho_0 \left(\frac{1}{J} - \frac{1}{J_0}\right). \end{aligned} \tag{2.23}$$

Thus, the resistance is set by the steady state flux in a periodic system.

2.6 Domain separation

The external potential used in this system, see equation (2.1), is defined piecewise and thus affects only a limited region of the whole system. As an apparent strategy to reduce the overall complexity, we divide the whole system (either $\mathbb{R}$ or L) into separate domains. Each domain can be treated separately, meaning that a solution of the differential equation can be given independently of the other parts of the system. Finally, to get a global solution the boundary conditions of all partial solution have to be linked.

In the literature, we can find a solution for the particle flux given a general external

potential in periodic systems [67],

$$J_0 = \frac{L(1-e^{-\beta FL})}{I_+ I_- - (1-e^{-\beta FL})\int_0^{L_x}\mathrm{d}x\; e^{-\beta V_{\mathrm{ext}}(x)}\int_0^x \mathrm{d}x'\; e^{-V_{\mathrm{ext}}(x')}}, \tag{2.24}$$

with $I_\pm = \int_0^{L_x}\mathrm{d}x\; e^{\pm V_{\mathrm{ext}}(x)}$. However, for this expression does not apply to an infinite system and it becomes impractical if several piecewise defined potentials are given. The approach to divide the system into distinct domains as demonstrated here is conceptually simpler and easier to calculate.

In a system with n similar barriers we can identify two different types of domains:

- Barrier parts, where $V_{\mathrm{ext}} > 0$, referred by $\mathbb{B}$
- Channel parts, where $V_{\mathrm{ext}} \equiv 0$, referred by $\mathbb{C}$

See figure 2.1 for an illustration.

2.6.1 Solution in a channel domain

In the channel $f(x) = F$ is constant yielding a relatively simple expression from the general solution (2.17):

$$\begin{aligned} \rho_{\mathrm{hom}}(x) &= \mathcal{C}_0 e^{Fx} \\ \rho_{\mathrm{in}}(x) &= -J_0 e^{Fx}\int^x \mathrm{d}x'\; e^{-Fx'} \\ &= \frac{J_0}{F} \\ \Rightarrow \qquad \rho_{\mathbb{C}}(x) &= \frac{J_0}{F} + \mathcal{C}_0 e^{Fx}. \end{aligned} \tag{2.25}$$

2.6.2 Solution in a barrier domain

The situation in the barrier domain is clearly more complicated than the channel case. The effective force function is (affine) linear: $f(x) = F + \frac{2V_0}{\lambda^2}(x - x_0)$. We get

the following solution for the density profile:

$$\begin{aligned}
\rho_{\text{hom}}(x) &= \mathcal{C}_0' e^{(F-\frac{2V_0}{\lambda^2}x_0)x+\frac{V_0}{\lambda^2}x^2} \\
&= \mathcal{C}_0' e^{-\frac{V_0}{\lambda^2}\left(x_0-\frac{F\lambda^2}{2V_0}\right)^2} e^{\frac{V_0}{\lambda^2}\left((x-x_0)+\frac{F\lambda^2}{2V_0}\right)^2} \\
&= \mathcal{C}_0 e^{\frac{V_0}{\lambda^2}\left((x-x_0)+\frac{F\lambda^2}{2V_0}\right)^2} \\
\rho_{\text{in}}(x) &= -J_0 e^{\frac{V_0}{\lambda^2}\left((x-x_0)+\frac{F\lambda^2}{2V_0}\right)^2} \int^x \mathrm{d}x'\, e^{-\frac{V_0}{\lambda^2}\left((x'-x_0)+\frac{F\lambda^2}{2V_0}\right)^2} \\
&= -J_0\sqrt{\frac{\pi\lambda^2}{4V_0}}\, e^{\frac{V_0}{\lambda^2}\left((x-x_0)+\frac{F\lambda^2}{2V_0}\right)^2} \operatorname{erf}\left(\frac{\sqrt{V_0}}{\lambda}\left[(x-x_0)+\frac{F\lambda^2}{2V_0}\right]\right) \\
\Rightarrow \qquad \rho_{\mathbb{B}}(x) &= e^{\frac{V_0}{\lambda^2}\left((x-x_0)+\frac{F\lambda^2}{2V_0}\right)^2} \left\{\mathcal{C}_0 - J_0\sqrt{\frac{\pi\lambda^2}{4V_0}} \operatorname{erf}\left(\frac{\sqrt{V_0}}{\lambda}\left[(x-x_0)+\frac{F\lambda^2}{2V_0}\right]\right)\right\}
\end{aligned} \tag{2.26}$$

For convenience, we introduce the following abbreviations:

$$\begin{aligned}
\xi(x) &= \sqrt{V_0}\left(\frac{F\lambda}{2V_0}+\frac{x}{\lambda}\right), \\
\gamma &= \lambda\sqrt{\frac{\pi}{4V_0}},
\end{aligned} \tag{2.27}$$

Thus, we obtain a shorter expression for the density profile in a barrier domain

$$\rho_{\mathbb{B}}(x-x_0) = e^{\xi^2(x)}\left(\mathcal{C}_0 - J_0\gamma \operatorname{erf}(\xi(x))\right). \tag{2.28}$$

2.6.3 Decomposition into separate domains

Assuming non-overlapping barriers, we can decompose the system into an alternating series of theses domains. Let the barriers be located at $x_1, \ldots, x_n$ and the distance between the barriers $\Delta x_i = x_i - x_{i-1}$. Then, we have the following intervals:

- interval of barrier: $\mathcal{D}_{bi} = [x_i - \lambda, x_i + \lambda]$, length: $|\mathcal{D}_{bi}| = 2\lambda$
- interval of channel: $\mathcal{D}_{ci} = [x_{i-1} + \lambda, x_i - \lambda]$, length: $|\mathcal{D}_{ci}| = \Delta x_i - 2\lambda$

Infinite system

$$\begin{aligned}
\mathbb{R} &= \mathcal{D}_{c1} \cup \mathcal{D}_{b1} \cup \mathcal{D}_{c2} \cup \cdots \cup \mathcal{D}_{bn} \cup \mathcal{D}_{c(n+1)} \\
&= \bigcup_{i=1}^{n} (\mathcal{D}_{ci} \cup \mathcal{D}_{bi}) \cup \mathcal{D}_{c(n+1)} \\
\text{with } \mathcal{D}_{c1} &= [-\infty, x_1 - 1], \\
\mathcal{D}_{c(n+1)} &= [x_n + 1, \infty]
\end{aligned} \tag{2.29}$$

Periodic boundary conditions Choosing $x_n + 1 = L$, i.e. the last barrier domain ends at the periodic point, we have:

$$\begin{aligned} L &= \mathcal{D}_{c1} \cup \mathcal{D}_{b1} \cup \mathcal{D}_{c2} \cup \cdots \cup \mathcal{D}_{bn} \\ &= \bigcup_{i=1}^{n} (\mathcal{D}_{ci} \cup \mathcal{D}_{bi}) \end{aligned} \tag{2.30}$$

In the previous subsections we calculated the generic density profiles of each type of domain. Now we have to link all domains to get a global solution for $\rho(x)$. As a requirement, the global density profile has to be continuous. Thus, we can determine each constant of integration of every domain by solving a system of linear equations. In the case of an infinite system the constant of integration of the rightmost channel domain $\mathcal{D}_{c(n+1)}$ has to vanish. For the periodic system the rightmost domain is linked to the leftmost domain.

2.7 Solutions for one and two barrier systems

Although the strategy to calculate the density profile and delay time is clear the actual calculations are complicated. In this section we just present the results of one and two barriers in an infinite system as well as for periodic boundaries. Again, we make use of some abbreviations:

$$\begin{aligned} \xi_\pm &= \sqrt{V_0}\left(\frac{F\lambda}{2V_0} \pm 1\right) \equiv \xi(\pm\lambda), \\ \alpha &= \operatorname{erfi}(\xi_+) - \operatorname{erfi}(\xi_-), \\ \beta &= \operatorname{erf}(\xi_+) - \operatorname{erf}(\xi_-), \\ \Delta F &= \xi_+^2\, {}_2F_2\left(1, 1; \frac{3}{2}, 2; \xi_+\right) - \xi_-^2\, {}_2F_2\left(1, 1; \frac{3}{2}, 2; \xi_-\right), \\ h_L &= \frac{1 - e^{-F(L-2\lambda)}}{1 - e^{-FL}}, \\ m_{\Delta x} &= 2 - e^{-F(\Delta x - 2\lambda)}\left(1 - e^{-2F\lambda}\right), \\ \mu_{\Delta x} &= 2h_L - \frac{1 - e^{-2F\lambda}}{1 - e^{-FL}}\left(e^{-F(\Delta x - 2\lambda)} + e^{-F(L - \Delta x - 2\lambda)}\right), \end{aligned} \tag{2.31}$$

with $\operatorname{erfi}(x)$ the *imaginary* error function and ${}_2F_2\left(1, 1; \frac{3}{2}, 2; x\right)$ the generalized hypergeometric function.

Single barrier, infinite system

$$\Delta T_{\infty,1} = \frac{\gamma}{F}\left(\alpha e^{-\xi_+^2} + \beta e^{\xi_-^2}\right) + \alpha\gamma^2 \operatorname{erf}(\xi_+) - \frac{1 - e^{-2F\lambda}}{F^2} - \frac{\lambda^2 \Delta F}{2V_0} - \frac{2\lambda}{F} \tag{2.32}$$

Single barrier, periodic boundary condition

$$\begin{aligned}\Delta T_{P,1} =& \frac{\gamma}{F}\left(\alpha e^{-\xi_+^2} + \beta e^{\xi_-^2}\right) h_L + \frac{\alpha\gamma^2}{1-e^{-FL}}(\mathrm{erf}(\xi_+) - \mathrm{erf}(\xi_-)e^{-FL}) \\ & - \frac{h_L(1-e^{-2F\lambda})}{F^2} - \frac{\lambda^2\Delta F}{2V_0} - \frac{2\lambda}{F}\end{aligned} \tag{2.33}$$

Double barrier, infinite system

$$\begin{aligned}\Delta T_{\infty,2} =& \frac{\gamma m_{\Delta x}}{F}\left(\alpha e^{-\xi_+^2} + \beta e^{\xi_-^2}\right) + \alpha\gamma^2\left(2\,\mathrm{erf}(\xi_+) + e^{-F\Delta x}\beta\right) \\ & - \frac{m_{\Delta x}(1-e^{-2F\lambda})}{F^2} - \frac{\lambda^2\Delta F}{V_0} - \frac{4\lambda}{F}\end{aligned} \tag{2.34}$$

Double barrier, periodic boundary condition

$$\begin{aligned}\Delta T_{P,2} =& \frac{\gamma\mu_{\Delta x}}{F}\left(\alpha e^{-\xi_+^2} + \beta e^{\xi_-^2}\right) \\ & + \frac{\alpha\gamma^2}{1-e^{-FL}}\left(2(\mathrm{erf}(\xi_+) - \mathrm{erf}(\xi_-)e^{-FL}) + \beta(e^{-F\Delta x} + e^{-F(L-\Delta x)})\right) \\ & - \frac{\mu_{\Delta x}(1-e^{-2F\lambda})}{F^2} - \frac{\lambda^2\Delta F}{V_0} - \frac{4\lambda}{F}\end{aligned} \tag{2.35}$$

2.7.1 Conclusion

The analytical expressions for the delay time characterizing the added resistance of the barrier configuration are complicated. Nevertheless, similarities in the terms are recognizable. The expressions for periodic boundaries often include as a prefactor a function of e^{-FL}. We can indeed recover the respective infinite system expressions by considering the limit of large system size L. This result was not clear a priori since both situations are different in topology and properties, i.e., fixed density versus conserved number of particles. Our quantification of the resistance in 2.4 is therefore consistent.

3 Scientific Publications

This cumulative thesis includes three scientific publications that have been peer-reviewed or are in the process of peer-reviewing by the time of printing. In this chapter we provide reprints of the following three publications.

I M.P.N. Juniper, **U. Zimmermann**, A.V. Straube, R. Besseling, D.G.A.L. Aarts, H. Löwen, and R.P.A. Dullens, *Dynamic mode locking in a driven colloidal system: experiments and theory*, New J. Phys. **19**, 013010 (2017)

II **U. Zimmermann**, F. Smallenburg, and H. Löwen, *Flow of colloidal solids and fluids through constrictions: dynamical density functional theory versus simulation*, J. Phys.: Condens. Matter **28**, 244019 (2016)

III **U. Zimmermann**, H. Löwen, C. Kreuter, A. Erbe, P. Leiderer, and F. Smallenburg, *Negative resistance for colloids driven over two barriers in a microchannel*, submitted to Phys. Rev. Lett. (2017), published in arXiv: 1709.09711.

During the doctoral studies I have also contributed to two further publications that are not part of this thesis.

- M. Marechal, **U. Zimmermann**, and H. Löwen, *Freezing of parallel hard cubes with rounded edges*, J. Chem. Phys. **136**, 144506 (2012)
- H.H. Wensink, H. Löwen, M. Marechal, A. Härtel, R. Wittkowski, **U. Zimmermann**, A. Kaiser, and A.M. Menzel, *Differently shaped hard body colloids in confinement: from passive to active particles*, Eur. Phys. J.-Spec. Top. **222**, 3023 (2013)

Paper I Dynamic mode locking in a driven colloidal system: experiments and theory

M.P.N. Juniper, U. Zimmermann, A.V. Straube, R. Besseling, D.G.A.L. Aarts, H. Löwen, and R.P.A. Dullens,
Dynamic mode locking in a driven colloidal system: experiments and theory,
New J. Phys. **19**, 013010 (2017),
published by *IOP Publishing Ltd* and *Deutsche Physikalische Gesellschaft*.

Digital Object Identifier (DOI): 10.1088/1367-2630/aa53cd

Link to version of record:
`http://iopscience.iop.org/article/10.1088/1367-2630/aa53cd/meta`

Statement of contribution

MPNJ, AVS, RB, DGALA, and RPAD initiated the idea of this project. MPNJ performed the experiments under supervision of RPAD. AVS provided the Langevin dynamics computer simulations and derived the approximate analytical theory. UZ computed the numerical results of the DDFT under supervision of HL. MPNJ, UZ, and AVS discussed the results from experiment, theory, and numerical calculations. MPNJ, UZ, AVS wrote the paper supervised by HL and RPAD.

Copyright and license notice

IOP Publishing *New J. Phys.* **19** (2017) 013010 doi:10.1088/1367-2630/aa53cd

New Journal of Physics
The open access journal at the forefront of physics

Deutsche Physikalische Gesellschaft DPG
IOP Institute of Physics

Published in partnership with: Deutsche Physikalische Gesellschaft and the Institute of Physics

OPEN ACCESS

RECEIVED
3 October 2016

REVISED
5 December 2016

ACCEPTED FOR PUBLICATION
14 December 2016

PUBLISHED
12 January 2017

PAPER

Dynamic mode locking in a driven colloidal system: experiments and theory

Michael P N Juniper[1,2], Urs Zimmermann[3], Arthur V Straube[4], Rut Besseling[5], Dirk G A L Aarts[1], Hartmut Löwen[3] and Roel P A Dullens[1,6]

[1] Department of Chemistry, Physical and Theoretical Chemistry Laboratory, University of Oxford, South Parks Road, OX1 3QZ Oxford, UK
[2] The Francis Crick Institute, 1 Midland Road, London NW1 1AT, UK
[3] Institut für Theoretische Physik II—Soft Matter, Heinrich-Heine-Universität Düsseldorf, Universitätsstraße 1, D-40225 Düsseldorf, Germany
[4] Department of Mathematics and Computer Science, Freie Universität Berlin, Arnimallee 6, D-14195 Berlin, Germany
[5] InProcess-LSP, Molenstraat 110, 5342 CC, Oss, The Netherlands
[6] Author to whom any correspondence should be addressed.

E-mail: roel.dullens@chem.ox.ac.uk

Keywords: dynamic mode locking, colloids, optical potential energy landscape, optical trapping, nonlinear dynamics

Abstract

In this article we examine the dynamics of a colloidal particle driven by a modulated force over a sinusoidal optical potential energy landscape. Coupling between the competing frequencies of the modulated drive and that of particle motion over the periodic landscape leads to synchronisation of particle motion into discrete modes. This synchronisation manifests as steps in the average particle velocity, with mode locked steps covering a range of average driving velocities. The amplitude and frequency dependence of the steps are considered, and compared to results from analytic theory, Langevin dynamics simulations, and dynamic density functional theory. Furthermore, the critical driving velocity is studied, and simulation used to extend the range of conditions accessible in experiments alone. Finally, state diagrams from experiment, simulation, and theory are used to show the extent of the dynamically locked modes in two dimensions, as a function of both the amplitude and frequency of the modulated drive.

1. Introduction

Synchronisation is one of the most diverse fundamental physical phenomena [1]. From Huygens' pendulum clocks 350 years ago [2, 3] to fireflies [4], applause [5, 6], and animals' circadian rhythms [7], frequency entrainment occurs all over the natural and technological world. The phenomenon occurs when weakly coupled competing oscillators adjust their rhythms to match each other [4]. Synchronisation on the micro-scale is of technological importance, as the decreasing size of electronic and mechanical systems demands ever-smaller frequency references [8]. Recent developments include electromechanical [9, 10] and optomechanical oscillators [11, 12], but such systems are limited in their scalability [12].

Dynamic mode locking is a synchronisation phenomenon that occurs when systems with a natural internal frequency are driven by an external modulation. Competition between the two frequencies leads to coupling, causing the system to synchronise into repeating modes of motion. Previous work has sought to understand dynamic mode locking in superconductor vortex lattices [13–17], but the difficulty in visualising such systems makes model systems necessary [18]. Other systems showing such resonance behaviour include driven adatoms on atomic surfaces [19, 20], and Josephson junctions [21–23]. The AC Josephson effect occurs when the tunneling electron pairs at an insulated superconductor junction are driven with an AC and DC current [24]. Regions appear where resistance does not increase with increasing DC current [23, 24], and the shape of the resulting graph is known as 'Shapiro steps'. Charge density waves are another technologically significant system

demonstrating dynamic mode locking, and have been extensively studied experimentally and numerically [25–27].

Model systems composed of colloidal particles in periodic potentials have been studied for a number of years [28, 29], from simple double well potentials [30–33] to directed motion [34–39], particle sorting [40], and kink generation [41] in two-dimensional (2D) optical lattices. Colloidal systems are easy to manipulate, and have accessible length and time scales, making them attractive models for the study of synchronisation at the micro-scale. Noise in Brownian systems has been found in theory to induce anomalous diffusion [42] and stochastic resonance [43–45], and rocking-ratchet like potentials have been used in optical and magnetic systems [46, 47]. The possibility of resonance has also been explored in systems with feedback [48] and random pinning potentials [49]. Recent work studied the transport properties of a system of magnetically driven colloidal particles [50]. Recent theoretical work also examines the possibility of producing mode locking steps in 2D colloidal monolayers [51, 52].

Here, a system of Brownian particles is driven over a sinusoidal optical potential energy landscape by a driving force consisting of constant and modulated parts. The natural frequency of the particle driven over the optical potential energy landscape by the DC component of the driving force couples to the frequency of the AC component. As we have shown previously [53], this coupling leads to dynamic mode locking. This work considers the frequency and amplitude dependence of the synchronisation, through experiments, Langevin dynamics (LD) simulations and dynamic density functional theory (DDFT). The three complementary approaches are used together to build a comprehensive picture of dynamic mode locking. Firstly, the theoretical and simulation approaches are introduced in section 2, including an analytical approximation. The experimental methods are described in section 3. Results from all of the approaches are described and discussed in section 4, including mode locked steps, state diagrams, and critical driving forces.

2. Theory and computer simulations

2.1. Langevin dynamics

To describe a Brownian particle driven by the sum of a constant and a modulated force across a periodic optical potential energy landscape, the overdamped Langevin equation is written as:

$$\zeta\, v(x,\, t) = \zeta \frac{\mathrm{d}x}{\mathrm{d}t} = F_{\mathrm{DC}} + F_{\mathrm{mod}}(t) + F_{\mathrm{T}}(x) + \xi(t), \tag{1}$$

where the particle velocity, v, at position x and time t depends on the force from the optical potential energy landscape, F_{T}, the Brownian force, $\xi(t)$ (modelled as Gaussian white noise with a mean of zero and variance of $2\zeta k_{\mathrm{B}} T$, where $k_{\mathrm{B}} T$ is thermal energy), the constant driving force, F_{DC}, the friction coefficient, ζ, and the oscillating driving force,

$$F_{\mathrm{mod}}(t) = F_{\mathrm{AC}} \cos(\omega t). \tag{2}$$

Here, F_{AC} is the amplitude of the modulated driving force, and $\omega = 2\pi\nu$ is the angular frequency, where ν is the frequency of the applied oscillation. Note that in this paper, 'DC' and 'AC' are used only in analogy to direct- and alternating-current, and refer to constant- and oscillating-velocity drives respectively.

The optical potential energy landscape, $U_{\mathrm{T}}(x)$, is taken to be sinusoidal, as described in [53–55]:

$$U_{\mathrm{T}}(x) = -\frac{2\sqrt{2\pi}\, V_0^{3/2}}{\lambda k^{1/2}} \left[\frac{1}{2} + \exp\left(-\frac{2\pi^2 V_0}{\lambda^2 k}\right) \cos\left(\frac{2\pi x}{\lambda}\right)\right], \tag{3}$$

where k is the trap stiffness, V_0 is the trap strength, and λ is the wavelength of the landscape. Equation (3) leads to an optical force [55]:

$$F_{\mathrm{T}} = -\frac{\partial U_{\mathrm{T}}}{\partial x} = -F_{\mathrm{C}} \sin\left(\frac{2\pi x}{\lambda}\right), \tag{4}$$

where the amplitude of the landscape, F_{C}, is given by the following equation [55]:

$$F_{\mathrm{C}} = \frac{4\sqrt{2}\,(\pi V_0)^{3/2}}{\lambda^2 k^{1/2}} \exp\left(-\frac{2\pi^2 V_0}{\lambda^2 k}\right). \tag{5}$$

Thus, the full equation of motion for a particle driven by DC and AC driving forces over a sinusoidal optical potential energy landscape is given by:

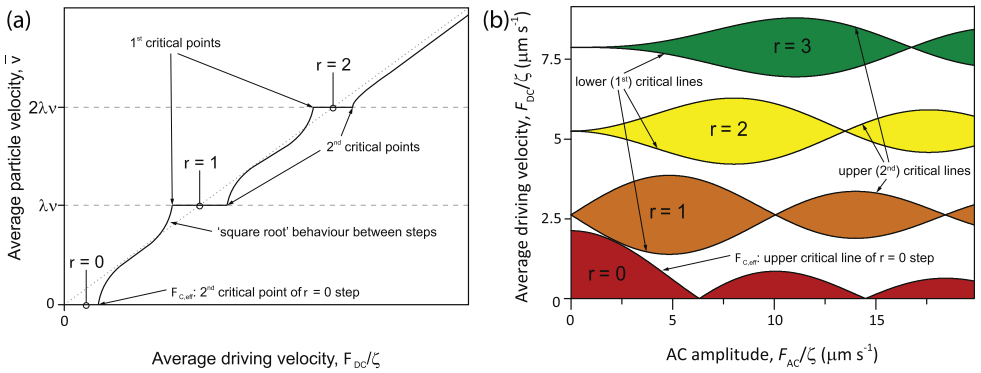

Figure 1. Mode locked steps and state diagram. (a) Schematic of average particle velocity as a function of average driving velocity (see equation (7); not to scale). Mode locked steps lie at $r\lambda\nu$, between pairs of critical points. (b) State diagram calculated from equation (8), for a periodic optical potential energy landscape with a trap spacing of $\lambda = 3.5\ \mu$m, and a frequency of $\nu = \frac{3}{4}$ Hz. Critical points defining a step in (a) become critical lines enclosing mode locked regions in the state diagram in (b).

$$\begin{aligned}\zeta\, v(x,\, t) &= \zeta\, \frac{\mathrm{d}x(t)}{\mathrm{d}t} \\ &= F_{\mathrm{DC}} + F_{\mathrm{AC}} \cos(2\pi\nu t) - F_{\mathrm{C}} \sin\left(\frac{2\pi x}{\lambda}\right) + \xi(t). \end{aligned} \tag{6}$$

Note that the amplitude of the landscape, F_{C}, is equal to the DC critical driving force described in [55], for the case of no temporal modulation and at zero temperature. In those conditions, the particle remains pinned to the landscape for driving forces below this critical value. As the total driving force in equation (6) is a sum of the DC and time dependent AC contributions, only an *effective* critical DC driving force, depending on the amplitude and frequency of the modulated component of the driving force, may be measured.

2.2. The 'high frequency' theory

While the equation of motion in equation (6) is not analytically soluble, useful insight can be obtained in the limit of high driving frequency ($\nu \gg F_{\mathrm{C}}/\lambda\zeta$) in the absence of noise. Within this approximation, it is possible to obtain an effective Adler equation [56, 57] similar to that found for the case of constant drive alone [55]. Thus an expression for the average velocity may be written (see appendix A for full details):

$$\bar{v} = \begin{cases} r\lambda\nu, & \text{if} \quad |\Delta F_{\mathrm{DC}}| < \left| F_{\mathrm{C}} J_{-r}\left(\frac{F_{\mathrm{AC}}}{\lambda\nu\zeta}\right)\right|; \\ r\lambda\nu \pm \dfrac{1}{\zeta}\sqrt{\Delta F_{\mathrm{DC}}^2 - F_{\mathrm{C}}^2 J_{-r}^2\left(\frac{F_{\mathrm{AC}}}{\lambda\nu\zeta}\right)}, & \text{if} \quad |\Delta F_{\mathrm{DC}}| > \left| F_{\mathrm{C}} J_{-r}\left(\frac{F_{\mathrm{AC}}}{\lambda\nu\zeta}\right)\right|, \quad \Delta F_{\mathrm{DC}} \gtrless 0, \end{cases} \tag{7}$$

where $\Delta F_{\mathrm{DC}} = F_{\mathrm{DC}} - r\lambda\nu\zeta$, $r = 0, \pm1, \pm2, \ldots$, and J_m is the mth order Bessel function of the first kind. This 'square root law' expression is the AC driven counterpart to the simpler form found for the case of DC drive alone [55]:

$$\bar{v} = \begin{cases} 0, & \text{if } F_{\mathrm{DC}} \leqslant F_{\mathrm{C}}; \\ \dfrac{1}{\zeta}\sqrt{F_{\mathrm{DC}}^2 - F_{\mathrm{C}}^2}, & \text{if } F_{\mathrm{DC}} > F_{\mathrm{C}}. \end{cases}$$

The condition for the approximation, $\nu \gg F_{\mathrm{C}}/\lambda\zeta$ (see equation (19), appendix A), means that on a landscape with a trap spacing of $\lambda = 3.5\ \mu$m ($F_{\mathrm{C}}/\zeta \approx 1.8\ \mu\mathrm{m\,s^{-1}}$), the high frequency regime is valid when $\nu \gg 0.5$ Hz.

The dependence of the average particle velocity, $\bar{v}$, on the driving velocity, F_{DC}/ζ, according to equation (7) is shown schematically in figure 1(a). Equation (7) describes mean particle velocity 'above' and 'below' critical points, with two critical points found for every absolute value of r, in contrast to the DC only case, which has only a single F_{C}. Between each pair of critical points, a 'subcritical' regime exists, where the particle velocity is constant, corresponding to mode locked steps. The form of this dependence is analogous to the Shapiro steps seen in Josephson junctions [23], and also in charge density wave systems [25] and vortex lattices [15–17, 58].

The two critical points F_{CRIT} at the ends of resonant step r are found by determining F_{DC} at the condition where the two different solutions in equation (7) coincide, $\Delta F_{\mathrm{DC}} = \pm|F_{\mathrm{C}} J_{-r}(F_{\mathrm{AC}}/(\lambda\nu\zeta))|$, at which point the square root vanishes. As a result, by recalling the definition of ΔF_{DC} and by replacing F_{DC} with F_{CRIT}, the following is obtained:

$$F_{\mathrm{CRIT}}/\zeta = r\lambda\nu \pm \frac{F_{\mathrm{C}}}{\zeta}\left| J_{-r}\left(\frac{F_{\mathrm{AC}}}{\lambda\nu\zeta}\right)\right|. \tag{8}$$

The amplitude (F_{AC}) and frequency (ν) dependence of F_{CRIT} defines state diagrams, with regions containing locked modes enclosed by pairs of critical lines. Figure 1(b) shows such a state diagram as a function of F_{AC}, for a particle driven with a frequency of $\nu = \frac{3}{4}$ Hz across an optical landscape with a trap spacing of $\lambda = 3.5\ \mu$m. Each colour and value of r represents a single mode locked velocity. The state diagram is formed from twisted 'Arnold Tongues' [1], where each separated region of the same colour actually represents a different dynamic mode with the same average velocity [53]. The second critical point of the 'zeroth' step appears as the effective critical driving velocity, $F_{\mathrm{C,eff}}$, below which the particle is pinned to the landscape and does not slide.

2.3. Dynamic density functional theory

The Langevin picture is stochastically equivalent to the Smoluchowski picture, in which the temporal evolution of the probability density distribution, $p(x,\ t)$, of the particle position is studied rather than the stochastic trajectories of individual particles. The Smoluchowski equation can be seen as a special case of the DDFT in the absence of interparticle interactions [59–61]. The governing equation for the probability density distribution is given by

$$\frac{\partial p(x,\ t)}{\partial t} = D\frac{\partial^2 p(x,\ t)}{\partial x^2} + \frac{1}{\zeta}\frac{\partial}{\partial x}(F(x,\ t)p(x,\ t)), \tag{9}$$

where $D = k_{\mathrm{B}}T/\zeta$ is the diffusion coefficient and $F(x,\ t) = F_{\mathrm{DC}} + F_{\mathrm{AC}}\cos(2\pi\nu t) - F_{\mathrm{C}}\sin(2\pi x/\lambda)$ is the total force acting on the particle. Equation (9) is solved numerically using a finite volume partial differential equation solver [62]. As an initial condition $p(x,\ t = 0)$, a very narrow Gaussian distribution is chosen. See appendix B for more details.

Within the Smoluchowski picture, averages of statistical quantities are defined by weighting these quantities with the particle probability distribution $p(x,\ t)$, i.e. $\langle a\rangle(t) = \int_{-\infty}^{\infty} \mathrm{d}x\ a(x)p(x,\ t)$. These averages are stochastically equivalent to noise averages performed in the Langevin picture. Thus, the mean particle position is $\langle x\rangle(t)$. The mean velocity is further defined as the change in the mean particle position in time:

$$\bar{v} = \overline{\frac{\mathrm{d}\langle x\rangle}{\mathrm{d}t}}, \tag{10}$$

where overbar denotes a time average. As a measure of the fluctuations around the mean particle trajectory, the variance of the particle probability distribution is considered:

$$\sigma^2(t) = \langle[x - \langle x\rangle]^2\rangle(t). \tag{11}$$

In the context of this work, if the standard deviation, $\sigma(t)$, is much smaller than the trap spacing then almost all possible particle trajectories end up in the same trap as the mean particle position after time t. If the standard deviation is larger than λ then possible particle trajectories end up distributed in potential wells surrounding the mean. Particle fluctuations around the mean position may be quantified using an effective long-time diffusion coefficient, defined from the variance:

$$D_{\mathrm{eff}} = \lim_{t\to\infty}\frac{\sigma^2(t)}{2t}. \tag{12}$$

3. Experimental methods

3.1. Colloidal model system

The colloidal system is composed of Dynabeads M-270 carboxylic acid (diameter 3 μm), in 20% $\mathrm{EtOH}_{\mathrm{aq}}$, held in a quartz glass sample cell (Hellma) with internal dimensions of $9 \times 20 \times 0.2$ mm. Particles are much more dense than the solvent, and sediment into a single layer near the bottom of the sample cell. The coefficient of friction, ζ, is found from diffusion to be 9.19×10^{-8} kg s^{-1}, slightly higher than expected from Stokes friction ($\zeta_{\mathrm{Stokes}} = 6\pi\eta a$ with η the viscosity), due to the proximity of the particles to the wall. Particle concentration is low, so that only a single particle is visible in the field of view.

3.2. Experimental setup and parameters

The experimental setup consists of an infra-red (1064 nm) laser, controlled using a pair of perpendicular acousto-optical deflectors, and focused using a 50×, NA = 0.55 microscope objective [54]. The one-dimensional periodic optical landscape, with trap spacing $\lambda = 3.5\ \mu$m, is generated in Aresis Tweez software controlled from a LabView interface. A landscape with this trap spacing may be treated as sinusoidal, as shown in [55]. The traps are time-shared at 5 kHz, such that on the time scale of the particles (with a Brownian time of

~50 s, and at least $\sim\frac{1}{3}$ s to be driven one trap spacing at a given F_{DC}), the traps form a constant potential energy landscape. The laser power and the total number of traps are held constant throughout the experiments, so that the laser power per trap is consistent. A laser power of 350 mW is set and 46 traps are used, corresponding to ~0.75 mW per trap at the sample. This gives typical values of trap stiffness, $k = 3.8 \times 10^{-7}$ kg s^{-2}, and trap strength, $V_0 = 90\, k_B T$ [54, 55].

The driving force is provided by a PI-542.2CD piezo-stage, controlled using the LabView interface, at driving velocities of $0.05 \leqslant F_{DC}/\zeta \leqslant 8\ \mu$m s^{-1}. AC driving velocity is added to the DC drive, with an amplitude $0.4 \leqslant F_{AC}/\zeta \leqslant 14\ \mu$m s^{-1}, and a frequency of $\frac{1}{10}$ Hz $\leqslant \nu \leqslant 2$ Hz.

Images are focused onto a Ximea CMOS camera using a 40×, NA = 0.50 microscope objective, and the particle position is recorded live at 40 Hz from the camera image.

3.3. Average velocity experiments

To obtain plots of average particle velocity against driving velocity, six repeats across the whole potential landscape are made at each driving velocity for each amplitude and frequency of the AC drive. Average velocity, $\overline{v}$, is found by linearly fitting the particle trajectory, $x(t)$, over an integer number of periods of the oscillation.

3.4. Critical driving velocity experiments

The critical DC driving velocity is defined as the DC driving velocity at which the particle starts to slide irreversibly across the optical potential energy landscape. It is found by iterating the DC driving velocity, with a maximum resolution of 0.05 μm s^{-1}. A particle is said to be pinned if it still returns to its starting lattice position after the stage has moved 100 μm, or three minutes has elapsed, whichever happens first. The region in which the particle does not irreversibly slide is essentially the zeroth mode locked step, and the effective critical driving velocity is therefore the second critical point of this step (see section 2.2).

The critical driving velocity found here is *not* the critical driving velocity found in our previous work [55], F_C/ζ, because the total driving force in equation (6) is a sum of the DC and time dependent AC contributions. Therefore the critical driving velocity measured here is an *effective* critical driving velocity, $F_{C,\mathrm{eff}}/\zeta$, as it is not purely a property of the landscape. However, clearly when $F_{AC} = 0$, $F_{C,\mathrm{eff}} \equiv F_C$.

4. Results and discussion

Results are presented which show the amplitude and frequency dependence of the mode locked steps and state diagrams illustrated in figure 1. Experimental results and DDFT computations are compared to LD simulations and the analytic approximation for the high frequency limit (section 2.2) as appropriate. In general, good quantitative agreement is found between the various approaches.

4.1. The mode locking steps

The effect of introducing the oscillating force term to the equation of motion (equation (6)) on $\overline{v}$ as a function of F_{DC}/ζ is shown in figure 2(a). Here, data with a modulated force of amplitude $F_{AC}/\zeta = 5.2\ \mu$m s^{-1} and frequency $\nu = \frac{3}{4}$ Hz (△) is compared to the $F_{AC} = 0$ (○), i.e. DC drive only) case for a landscape of trap spacing $\lambda = 3.5\ \mu$m (see [53, 55]). The case of $F_{AC} \neq 0$ follows the 'Shapiro steps' form illustrated in figure 1(a). The effective critical driving velocity for the modulated case is almost zero, after which $\overline{v}$ increases until it is significantly larger than that expected for a free particle (grey line), implying that the particle is moving on average more quickly than the piezo stage. The average velocity then plateaus on the first resonant step, at $\overline{v} = 1\lambda\nu = 2.625\ \mu$m s^{-1}. The step extends over a range of driving velocities, and then $\overline{v}$ increases after the second critical point, to meet another step, at twice the average particle velocity of the first.

The solid and dashed lines on figure 2(a) show results from LD simulations, both with and without the noise term. The steps found from the experiments are faithfully reproduced by the simulations, with the inclusion of noise obviously important in this system of Brownian particles. The effect of noise is important in the vicinity of the critical points, where it is seen to round the edges of the steps. Figure 2(b) compares results from DDFT (upper panel), and the high frequency approximation (lower panel, see section 2.2) to the experimental data. The DDFT lines here overlap with results from the LD simulations with the same intensity of thermal noise (i.e. the same temperature and friction constant, as $D = k_B T/\zeta$). For this reason we only show one set of results (those from LD simulations) on figures 4(a) and (b) and 8(a) and (b). The high frequency theory results, from equation (7), are calculated with respect to each critical point, and it is notable that although the step positions are largely captured, the results between steps, from adjacent critical points, do not necessarily agree.

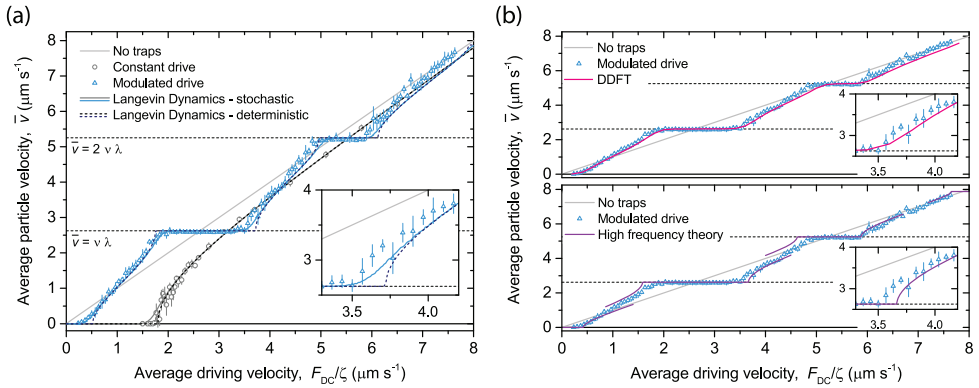

Figure 2. Average particle velocity, $\bar{v}$, against average driving velocity, F_{DC}/ζ, for both constant and modulated drives, from experiments, simulations, high frequency theory, and dynamic density functional theory (DDFT). (a) Comparison of experimental data and Langevin dynamics simulations. ○ constant drive: $F_{AC} = 0$; △ modulated drive: $F_{AC}/\zeta = 5.2\ \mu\text{m s}^{-1}$, $\nu = \frac{3}{4}$ Hz (error bars represent the standard deviation of the repeats); solid lines: Langevin dynamics results; dashed lines: Langevin dynamics results with no noise term; grey line: no traps calibration; horizontal dashed lines: step positions $\bar{v} = n\lambda\nu$. Includes experimental data from [53, 55]. (b) Comparison of experimental data with DDFT results (upper panel), and high frequency theory (lower panel). Insets highlight the second critical point of the first step.

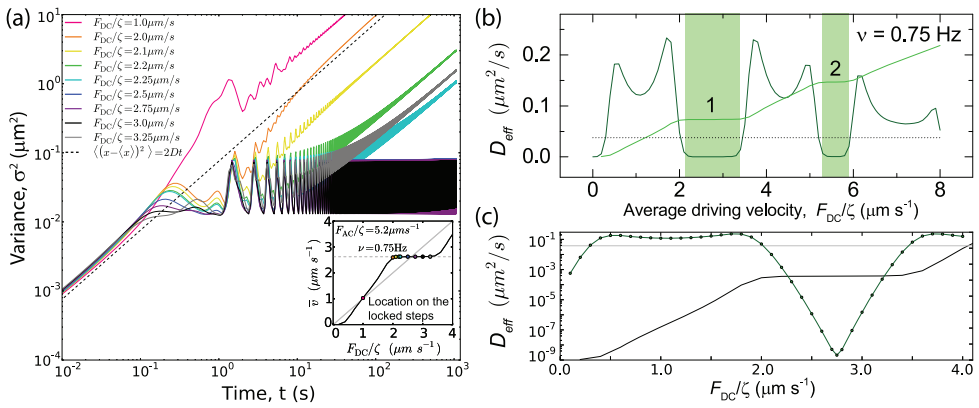

Figure 3. Variance and long-time diffusion from DDFT calculations, for $\nu = \frac{3}{4}$ Hz and $F_{AC}/\zeta = 5.2\ \mu\text{m s}^{-1}$. (a) Double logarithmic plot of variance versus time for various drives F_{DC}. The black dashed line refers to a Brownian particle in the absence of an external potential. The inset shows the location of the respective state points on the locked steps for the lines in the main panel. (b) Effective long-time diffusion coefficient as a function of average driving velocity. Dark line shows D_{eff}, pale line shows the mode locked staircase calculated from DDFT for comparison, and does not match the y-axis scale. Step extents are highlighted by the coloured bands, and the dotted line indicates the diffusion coefficient of a free particle. (c) D_{eff} for the first step, plotted on a log scale.

4.1.1. Variance and diffusion

Next, we perform DDFT calculations and consider fluctuations around the mean particle position, which strongly depend on whether or not the system is mode locked. In figure 3(a) the variance is shown as a function of time for the conditions considered above ($F_{AC}/\zeta = 5.2\ \mu\text{m s}^{-1}$, $\nu = \frac{3}{4}$ Hz). The displayed numerical data correspond to states on the mode locked steps around the first step (see inset). For unlocked states ($1.0 \leqslant F_{DC}/\zeta \leqslant 2.0\ \mu\text{m s}^{-1}$) the variance grows rapidly, corresponding to an effective diffusion much larger than the free diffusion (dashed line). In the mode locked states ($2.5 \leqslant F_{DC}/\zeta \leqslant 3.25\ \mu\text{m s}^{-1}$) the variance reaches a long-lived plateau where the diffusion is (nearly) zero, before eventually crossing over. Similar intermediate plateaus have also been observed in underdamped systems [63–65] and static systems ($F_{AC} = 0$) [66, 67].

The effective long-time diffusion coefficient (equation (12)) is the limit of $\sigma^2(t)/2t$ as $t \to \infty$. Plotting D_{eff} as a function of average driving velocity offers additional insight into the mode locked steps. Figure 3(b) shows that effective diffusion is close to zero at the mode locked steps, and much higher between. The typical double-peak signature for D_{eff}, as described in [44], is recovered. The low D_{eff} values in the locked regions result from a

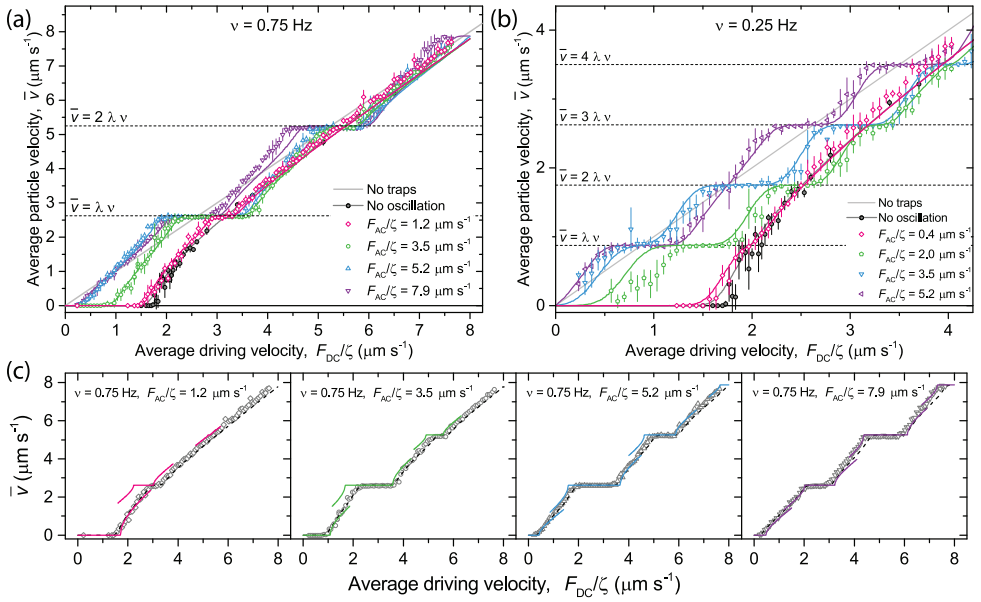

Figure 4. Average particle velocity as a function of average driving velocity, at constant AC frequency of (a) $\frac{3}{4}$ Hz and (b) $\frac{1}{4}$ Hz. Symbols show experimental data, solid lines show results of Langevin dynamics simulations. Dashed lines indicate step positions $n\lambda\nu$. Dark grey circles and line indicate case for no oscillation [55], light grey line indicates case for no traps. (c) Results for high frequency theory (solid lines), for each of the cases in panel (a) for $\nu = \frac{3}{4}$ Hz, compared to LD simulations (dashed lines) and experiments (symbols).

vanishing influence of thermal noise which can also be found in related systems [68, 69]. This is a symptom of the predictability of the locked state: when the particle is locked into a particular mode of motion, its position on the periodic landscape after a certain time depends purely on the driving conditions. D_{eff} is highest in unlocked states on the cusp of synchronisation conditions, as a small perturbation may cause the particle to jump to the next potential well, or stay in the present one. This corresponds to the discontinuities at the critical points in the schematic in figure 1(a). Figure 3(c) shows D_{eff} for the first step on a log scale, showing that it decreases by ~8 orders of magnitude between the unlocked and locked states. To put this into context, the lowest effective long-time diffusion coefficient $D_{\text{eff}} \approx 2.1 \times 10^{-9}\ \mu\text{m}^2\ \text{s}^{-1}$ corresponds to the particle being one lattice spacing away from the predicted position after approximately 45 years.

4.2. Dependence on the amplitude

As the synchronisation condition depends only on the trap spacing and the modulation frequency, changing the modulation amplitude alone does not alter the step velocities. Figure 4(a) shows mode locking steps obtained from both experiment and LD simulations for four different amplitudes, at a frequency of $\nu = \frac{3}{4}$ Hz. This shows that there is, however, a strong dependence of the width of the locked step on the oscillation amplitude. For very low amplitude there is a small visible first step, giving a deviation from the zero oscillation data, but no second step is observed; the points lie on top of the $F_{\text{AC}} = 0$ line. As amplitude increases, the first step increases in width, and a second step appears and widens. The first step then appears to narrow. There is generally a good agreement between the experimental data and the LD simulations, with small deviations possibly due to experimental uncertainties such as the variability of the laser power during the experiment.

Figure 4(b) shows data at a lower frequency of $\nu = \frac{1}{4}$ Hz, for four amplitudes. The lower frequency means that a larger number of steps appear in the same range of particle velocities. Four steps are visible in the range shown (which is smaller than that in figure 4(a)), with step width varying widely. Notably, the $F_{\text{AC}}/\zeta = 5.2\ \mu\text{m s}^{-1}$ line has three steps at $n = 1, 3$ and 4, but no step is visible at $n = 2$.

It is pertinent at this juncture to compare the results for $\nu = \frac{3}{4}$ Hz to the high frequency theory (equation (7)). Figure 4(c) shows each of the four sets of conditions in panel (a), with the results for each critical point from equation (7) (solid lines) compared to the LD results (dashed lines) and experimental results (symbols) from panel (a). The first observation is that the high frequency approximation appears to better match the data at higher amplitudes. The most likely reason for this is that the Bessel function in equation (7) gets smaller as the argument, which is proportional to F_{AC}, increases (see equation (19) in appendix A). This means

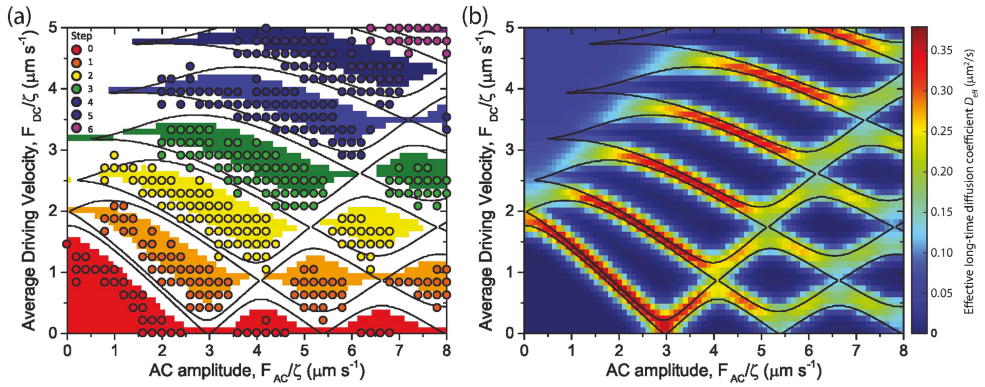

Figure 5. State diagram showing locked dynamic modes at a driving frequency of $\frac{1}{4}$ Hz. (a) Coloured dots: locked states found in experiments (data from [53]). Step numbers, n, are the net number of steps taken by the particle: regions of the same colour represent the same net forward particle motion. Coloured regions in the background represent locked states determined from DDFT; white regions are unlocked. Solid lines show critical lines calculated from LD simulations in the absence of noise. (b) Colour scale represents the effective diffusion coefficient, D_{eff}, calculated from DDFT, solid lines are critical lines found from LD simulations as in (a).

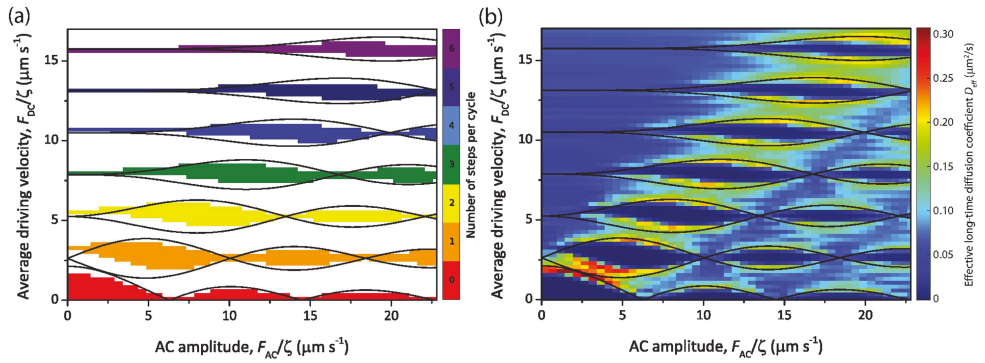

Figure 6. State diagram showing all locked dynamic modes at a driving frequency of $\frac{3}{4}$ Hz, over a range of AC amplitudes and average driving velocities. (a) Coloured regions represent locked states as determined from DDFT, white regions are unlocked. Locked states are numbered by an integer n, the net number of steps taken by the particle. Solid lines show critical lines calculated from equation (8), and represent theoretical state boundaries. (b) Colour scale represents the effective diffusion coefficient, D_{eff}, calculated from DDFT, solid lines are again calculated from equation (8). Locked states appear as dark blue.

that at a given frequency the condition setting the validity of the high frequency approximation is fulfilled better for higher F_{AC}. Note also that the theory consistently overestimates the step width, as it is deterministic, whereas the critical points in experiments and simulations are somewhat rounded by noise. Finally, it may be seen that as in figure 2(b), the lines between steps determined from different critical points do not overlap, as the 'square-root law' sections are only valid in the close vicinity of their critical points.

4.2.1. State diagram: low frequency regime

As was shown in figure 1(b), state diagrams may be constructed which show the extent of dynamic mode locking as a function of F_{AC}/ζ and F_{DC}/ζ. In our previous work [53], we used such a plot to locate numerous dynamic modes for a driving frequency of $\frac{1}{4}$ Hz. In figure 5(a) we compare these prior experimental results (circles coloured according to the integer step number, n) with locked regions from DDFT (background colour) and critical lines from LD simulations in the absence of noise. Note that points corresponding to unlocked states are not shown, for ease of interpretation. There is very good agreement between the DDFT and the deterministic LD results, with the only difference being that the regions calculated from DDFT are smaller, due to the presence of the noise that is incorporated into the DDFT. Both are in good agreement with the experimental data, except that locked states appear to be found at a slightly higher range of driving velocities in the simulations.

Figure 5(b) again shows critical lines from LD simulations, plotted over the effective diffusion coefficient, D_{eff}, obtained from DDFT. Locked states appear as dark blue regions, with fairly broad boundaries where step edges are smoothed by noise. Between the locked states the effective diffusion is higher, as was seen in figure 3(b). D_{eff} is particularly high between closely spaced locked modes, as a small perturbation may lead to the particle becoming temporarily trapped in one mode or the other. The related enhanced increase in variance manifests in the experimental data as wider error bars between the modes in figure 4(b). That the diffusion is so high in these regions probably contributes to the mismatch between the experimental and simulation data in panel (a)—a small change in the experimental conditions could cause the particle to cross mode boundaries.

It is nice to observe in figure 5 that the mode boundary lines oscillate, with the first and second critical lines crossing and swapping identity between the modes. The upshot of this oscillation is that there are conditions in which certain locked modes do not appear, for example it is clear that $F_{\text{AC}}/\zeta = 5.2\ \mu\text{m s}^{-1}$ lies between two regions with $n = 2$, which corresponds exactly to the missing step observed in figure 4(b). This effect is of course mirrored in the critical driving velocity line, being the upper mode boundary of the zeroth step, resulting in some conditions where the critical driving velocity is zero, for example $F_{\text{AC}}/\zeta = 5.2\ \mu\text{m s}^{-1}$ again.

4.2.2. State diagram: high frequency regime

In section 2.2, an analytical expression (equation (8)) was obtained which could predict the locations of the first and second critical points for each mode locked step. It was found that this expression should be valid in the region where $\nu \gg 0.5$ Hz. It is not possible to probe this region in detail in the experiments, as at higher frequencies, increased particle velocities are required to obtain higher modes, with a resulting loss in resolution. However, using DDFT it is possible to examine this regime, and obtain a state diagram similar to that from experiment. Figure 6(a) shows a state diagram calculated via DDFT for $\nu = \frac{3}{4}$ Hz, with the mode locked regions being represented by colours, as in figure 5(a). Also plotted on figure 6(a) are lines calculated from equation (8). There is a remarkably good agreement between the DDFT results and the analytical prediction, showing that the approximation is valid to surprisingly low frequencies. The main deviation occurs at lower amplitudes, as was seen in figure 4(c). As in figure 5(a), the locked regions from DDFT are slightly smaller than the space between the critical lines, due to the noise term which must necessarily be ommited from the theory.

The mode locking footprint can also be seen in the effective diffusion coefficient: figure 6(b) shows the same calculated lines as panel (a), overlayed on D_{eff}, represented by a colour scale. The locked states are clearly visible as the dark blue regions on the state diagram, where the effective diffusion coefficient drops dramatically as seen in figure 3(c). The unlocked states range from blue, where the particle position is largely predictable, to the yellow and red regions between the mode locked steps. An interesting observation may be made in the region between the zeroth and first modes, where the theory predicts no gap between the second critical line of the zeroth mode and the first critical line of the first mode. The effective diffusion in this region is especially high, indicating that in the stochastic system the particle trajectory is highly unpredictable. It is probable that in this region, the particle rapidly jumps between periods of being pinned to the landscape, and being in the first mode.

4.2.3. Critical driving velocity

The state diagrams in figures 5 and 6 show that the critical driving velocity, $F_{\text{C,eff}}$, oscillates as a function of modulation amplitude. In figure 7 the critical driving velocities are shown in isolation, and experimental results are compared to LD simulations and the high frequency theory. Both sets of data, for $\nu = \frac{1}{4}$ Hz and $\nu = \frac{3}{4}$ Hz show a Bessel-function-like form, with the range of the oscillations determined by the frequency. Each peak actually represents a different pinned mode [53], and regions occur between the modes where the critical force is close to zero and thermal motion is sufficient to overcome the barriers. The theoretical prediction for the high frequency regime (equation (8)) predicts the shape of the experimental data reasonably well, but the LD simulations provide a somewhat better quantitative fit.

4.3. Dependence on the frequency

The frequency dependence of the step velocities is expressed in the synchronisation condition, $\overline{v} = n\lambda\nu$. Figure 8(a) shows $\overline{v}$ as a function of F_{DC}/ζ at three different frequencies, for an amplitude of $F_{\text{AC}}/\zeta = 2.0\ \mu\text{m s}^{-1}$. At a lower frequency more steps are seen over the same range of particle velocities as more harmonics are attainable. Indeed at the lowest frequency, $\nu = \frac{1}{4}$ Hz, the mean particle velocity shows three steps corresponding to the first three integer multiples of $\nu\lambda$. The second and third steps at this frequency therefore coincide with the first steps for the other two frequencies, of $\nu = \frac{1}{2}$ Hz and $\nu = \frac{3}{4}$ Hz. As was seen in figures 4(a) and (b), there is generally a good agreement between the LD simulations and the experiments.

Figure 8(b) shows the frequency dependence of the average particle velocity for an amplitude of $F_{\text{AC}}/\zeta = 5.2\ \mu\text{m s}^{-1}$, for frequencies ranging from $\nu = \frac{1}{4}$ Hz to $\nu = \frac{3}{2}$ Hz. It is worth noting that, as was seen in figure 4(b), not all possible steps appear; for example there is no visible step at $\overline{v} = \frac{1}{2}\lambda\ \text{s}^{-1}$ for $\nu = \frac{1}{4}$ Hz. Both

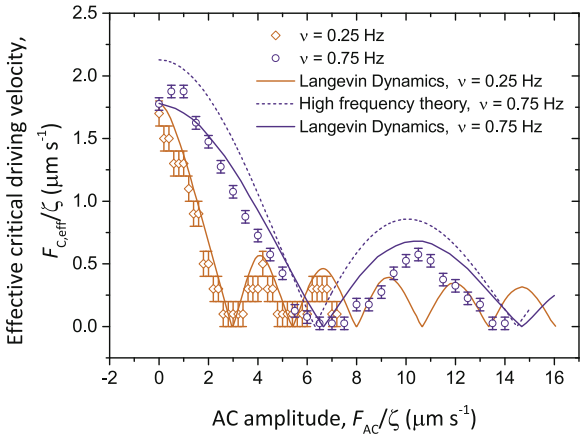

Figure 7. Critical driving velocity, $F_{C,eff}/\zeta$, as a function of modulation amplitude, F_{AC}/ζ, for $\nu = \frac{1}{4}$ Hz and $\nu = \frac{3}{4}$ Hz. Symbols show experimental data, solid lines show LD simulation results, and the dashed line shows the high frequency approximation.

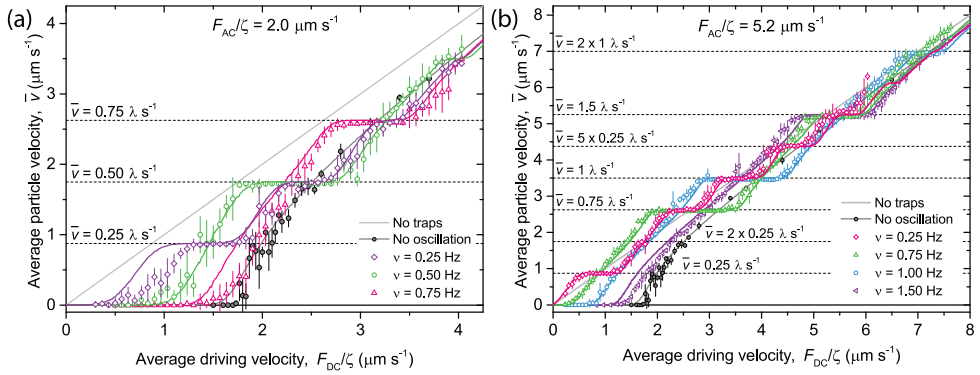

Figure 8. Average particle velocity as a function of average driving velocity, at constant AC amplitude of (a) $F_{AC}/\zeta = 2.0\ \mu$m s^{-1} and (b) $F_{AC}/\zeta = 5.2\ \mu$m s^{-1}. Symbols show experimental data, solid lines show results of Langevin dynamics simulations. Dashed lines indicate the position of the first step for each frequency, and some higher n steps for completeness. Dark grey circles and line indicate case for no oscillation [55], light grey line indicates case for no traps.

figures 8(a) and (b) show that step width is frequency dependent, in addition to the amplitude dependence shown above. Furthermore, the effective critical driving velocity clearly depends on the frequency: in both cases it is seen to increase with ν, approaching the oscillation-free critical driving velocity of $F_C/\zeta \approx 1.8\ \mu$m s^{-1}.

4.3.1. State diagrams and critical driving velocity

DDFT computation is used to produce frequency-dependence state diagrams, which are not feasable experimentally as very low frequencies require extremely long run times. Figure 9(a) shows four such state diagrams, at a range of amplitudes from $F_{AC} < F_C$ to $F_{AC} > F_C$. Also included on two of the state diagrams are effective critical driving velocity lines determined from LD simulations. As with the experiments, the run times required to produce further LD data, particularly at low frequencies, are prohibitively long. From the data presented, however, the origin of the increasing effective critical driving velocity seen in figures 8(a) and (b) is clear, although the LD line on the $F_{AC}/\zeta = 5.2\ \mu$m s^{-1} plot in particular highlights that the picture is more complex. At $F_{AC} > F_C$ (where F_C is the DC critical driving velocity), a series of bumps appear at low frequency, which are too fine to be resolved by the DDFT data. Below F_C, however (i.e. at $F_{AC}/\zeta = 1.7\ \mu$m s^{-1}), these bumps disappear, and the depinning transition is defined as a single monotonic increase. This effect has been noted previously for the Frenkel Kontorova model, for a chain of interacting particles [39, 45, 70].

Figure 9(b) shows the frequency dependent effective critical driving velocity for $F_{AC} > F_C$ in more detail. Experimentally determined values for F_C are shown, along with the LD simulation result. The experimental data shows a single smaller bump similar to that seen in the DDFT data, as it is also unable to resolve the numerous

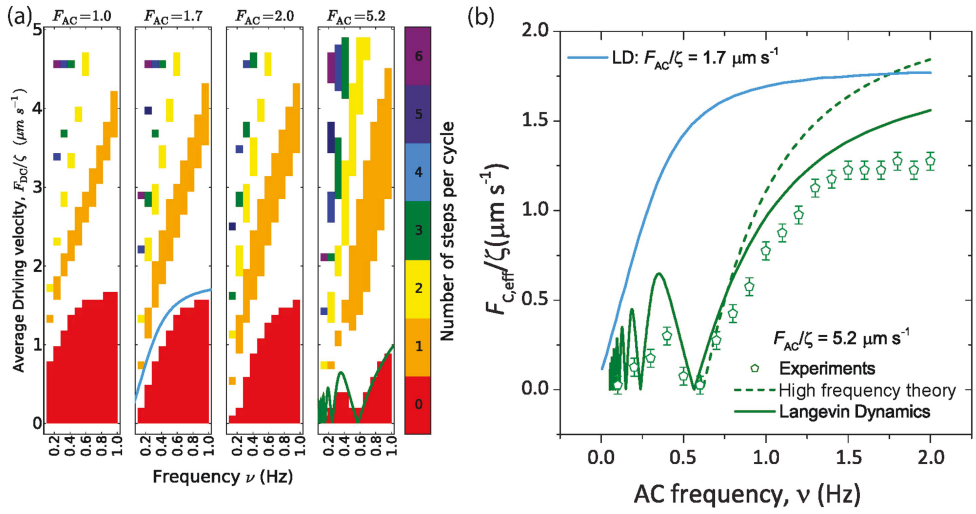

Figure 9. Frequency-dependence state diagrams and effective critical driving velocity. (a) State diagrams show locked dynamic modes for fixed amplitudes of $F_{AC}/\zeta = 1.0, 1.7, 2.0,$ and 5.2 μm s^{-1}. Coloured regions represent locked states as determined from DDFT, white regions are unlocked. Locked states are numbered by an integer step number, n. Solid lines show LD simulation results. (b) Effective critical driving velocity, $F_{C,\mathrm{eff}}/\zeta$, as a function of frequency for $F_{AC}/\zeta = 5.2$ μm s^{-1}. Symbols show experimental data, solid lines show LD simulation results, dashed line shows high-frequency theory (equation (8)). Also shown in blue is the LD simulation result for $F_{AC}/\zeta = 1.7$ μm s^{-1}.

smaller bumps shown by the LD data. The large bump at higher frequency, which plateaus at the DC-only critical driving velocity F_C, represents the truly pinned state, where the particle does not move at all during a cycle of the oscillation, whereas the smaller bumps at lower frequency represent states where the *net* particle motion is zero, as it moves but returns to the same potential well at the end of every cycle. Also presented in figure 9(b) is the prediction of the high frequency approximation, which captures the form of the experimental data, but has a higher magnitude due to the absence of a noise term in equation (8), and the LD line for $F_{AC}/\zeta = 1.7$ μm s^{-1}, for comparison.

5. Conclusions

Colloidal particles driven by the sum of constant and oscillating forces through a quasi-one-dimensional periodic optical potential energy landscape have been shown to exhibit rich nonlinear dynamical behaviour. Experiments showed that when an oscillating drive is applied, the average particle velocity has a staircase-like dependence on the average driving velocity, where the steps represent states of synchronisation between the particle motion and the substrate potential. These results could be faithfuly reproduced using LD simulations and DDFT, and in conditions of a high driving frequency the data mapped surprisingly well to an analytic approximation. Probing the variance in the particle position and the trajectory diffusion using DDFT showed that the effective diffusion coefficient drops dramatically at the resonant mode-locked steps, explaining why the analytic theory (calculated at 'zero temperature' with no fluctuations) is so successful.

The use of simulation and computation in addition to experimental results allowed a full exploration of the amplitude and frequency dependence of dynamic mode locking. State diagrams showing both the amplitude and frequency dependence of the extent of the locked modes exposed the oscillating nature of the critical lines which define the mode locked steps. These critical lines enclose regions which have been previously shown to represent different dynamic modes with the same net particle motion. Finally, the effective critical driving velocity below which a particle is pinned to the potential landscape has been studied, and it has been shown to have an oscillating dependence on the modulation amplitude, with some conditions having no effective critical driving velocity. The frequency dependence has been shown to be more complex, depending on whether the amplitude of the oscillation is above or below the critical driving velocity defined by the landscape.

By using a combination of experiments, computation, and analytic theory, it has been possible to explore the effect of a very wide range of conditions on dynamic mode locking, thereby giving a solid experimental and theoretical foundation to this dynamic synchronisation phenomenon.

IOP Publishing New J. Phys. 19 (2017) 013010 M P N Juniper et al

Acknowledgments

We thank Alice Thorneywork and Arran Curran for fruitful discussions. MPNJ, DGALA, and RPAD acknowledge EPSRC for financial support. UZ acknowledges support from the German Academic Exchange Service (DAAD).

Appendix

Appendix A. High frequency theory—further details

In order to solve equation (6) for a certain range of driving frequencies, the work of Cotteverte *et al* [71], Chow *et al* [72], and Reichhardt *et al* [58] is followed. Ideas developed in these previous works are used to draw an analytical approximation in this work. The first step in solving equation (6) is to neglect noise and split the particle trajectory, $x(t)$, into a part due to the terms independent of $x(t)$ and a deviation from it, caused by terms dependent on $x(t)$:

$$x(t) = x_0(t) + \delta(t). \tag{13}$$

Accordingly, the equation for $x_0(t)$ is taken to contain the DC and AC parts of the driving force,

$$\zeta \frac{\mathrm{d}x_0(t)}{\mathrm{d}t} = F_{\mathrm{DC}} + F_{\mathrm{AC}} \cos(\omega t), \tag{14}$$

which can be integrated to yield

$$\zeta\, x_0(t) = F_{\mathrm{DC}} t + \frac{F_{\mathrm{AC}}}{\omega} \sin(\omega t). \tag{15}$$

For the second part, $\delta(t)$, we obtain from equation (6):

$$\begin{aligned} \zeta \frac{\mathrm{d}\delta(t)}{\mathrm{d}t} &= -F_{\mathrm{C}} \sin\left[\frac{2\pi}{\lambda}(x_0(t) + \delta(t))\right] \\ &= -F_{\mathrm{C}} \sin\left[\frac{2\pi}{\lambda}\left(\frac{F_{\mathrm{DC}}}{\zeta} t + \frac{F_{\mathrm{AC}}}{\zeta\omega} \sin(\omega t) + \delta(t)\right)\right], \end{aligned} \tag{16}$$

where we have accounted for equations (14) and (15). Using the identity: $\sin\ [A\ \sin\ (\omega t) + B] \equiv \sum_{m=-\infty}^{\infty} J_m(A) \sin(B + m\omega t)$, where J_m is the mth order Bessel function of the first kind, $A = 2\pi F_{\mathrm{AC}}/(\zeta\omega\lambda)$ and $B = (2\pi/\lambda)(F_{\mathrm{DC}} t/\zeta + \delta)$, equation (16) becomes:

$$\zeta \frac{\mathrm{d}\delta(t)}{\mathrm{d}t} = -F_{\mathrm{C}} \sum_{m=-\infty}^{\infty} J_m\left(\frac{2\pi}{\lambda}\frac{F_{\mathrm{AC}}}{\zeta\omega}\right) \sin\left[\left(\frac{2\pi}{\lambda}\frac{F_{\mathrm{DC}}}{\zeta} + m\omega\right) t + \frac{2\pi}{\lambda}\delta(t)\right]. \tag{17}$$

Equation (17) is difficult to solve, so an approximation is made that only the leading term of the sum is retained, where

$$m\omega = -r\omega \approx -\frac{2\pi F_{\mathrm{DC}}}{\lambda\zeta} \quad (r = 0, \pm 1, \pm 2, \ldots), \tag{18}$$

determines the mode locking. This approximation is valid at high enough frequencies. Indeed, the variation with time of the leading term with $m = -r$ given by equation (18) is the slowest relative to ωt, $2\omega t$, ... of the next to leading terms with $m = r \pm 1$, $r \pm 2$, ... Provided that the dependence on $\delta(t)$ can be neglected in all next to leading terms, their averages over a period of the external modulation vanish. The scale of $\delta(t)$ can be estimated by noticing from equation (17) that $\mathrm{d}\delta(t)/\mathrm{dt} \sim F_{\mathrm{C}}/\zeta$ (see [72]) or, more accurately, $\mathrm{d}\delta(t)/\mathrm{dt} \sim J_{-r}(A) F_{\mathrm{C}}/\zeta$ and hence $\delta(t) \sim J_{-r}(A) F_{\mathrm{C}} t/\zeta$. By considering the term with the next to slowest variation, $m = -r \pm 1$, we require that $\omega t \gg \delta(t)$ to arrive at the condition for the validity of our high-frequency approximation:

$$\omega \gg \frac{2\pi}{\lambda}\frac{F_{\mathrm{C}}}{\zeta} J_{-r}\left(\frac{2\pi}{\lambda}\frac{F_{\mathrm{AC}}}{\zeta\omega}\right) \quad \text{or} \quad \nu \gg \frac{F_{\mathrm{C}}}{\lambda\zeta} J_{-r}\left(\frac{F_{\mathrm{AC}}}{\lambda\nu\zeta}\right). \tag{19}$$

Equation (17) therefore becomes:

$$\zeta \frac{\mathrm{d}\delta(t)}{\mathrm{d}t} = -F_{\mathrm{C}} J_{-r}\left(\frac{F_{\mathrm{AC}}}{\lambda\nu\zeta}\right) \sin\left[\frac{2\pi}{\lambda}\left(\frac{\Delta F_{\mathrm{DC}}}{\zeta} t + \delta(t)\right)\right], \tag{20}$$

where $\Delta F_{\mathrm{DC}} = F_{\mathrm{DC}} - r\lambda\nu\zeta$ is a small change in the constant part of the driving force, F_{DC}. Introducing a variable $q(t) = (\Delta F_{\mathrm{DC}}/\zeta) t + \delta(t)$ further reduces equation (20) to the form of an Adler equation [56, 57], equivalent to that found for the case of constant drive alone [55]:

$$\zeta \frac{\mathrm{d}q(t)}{\mathrm{d}t} = \Delta F_{\mathrm{DC}} - F_{\mathrm{C}} J_{-r}\left(\frac{F_{\mathrm{AC}}}{\lambda\nu\zeta}\right) \sin\left[\frac{2\pi}{\lambda} q(t)\right]. \tag{21}$$

The expression for the average velocity may then be written, by noting that $\bar{v} = \left\langle \frac{\mathrm{d}x(t)}{\mathrm{d}t} \right\rangle = F_{\mathrm{DC}}/\zeta + \left\langle \frac{\mathrm{d}\delta(t)}{\mathrm{d}t} \right\rangle = r\lambda\nu + \left\langle \frac{\mathrm{d}q(t)}{\mathrm{d}t} \right\rangle$, as the oscillating force term (the modulated part of the driving velocity) becomes zero after time averaging:

$$\bar{v} = \begin{cases} r\lambda\nu, & \text{if} \quad |\Delta F_{\mathrm{DC}}| < \left| F_{\mathrm{C}} J_{-r}\left(\frac{F_{\mathrm{AC}}}{\lambda\nu\zeta}\right) \right|; \\ r\lambda\nu \pm \frac{1}{\zeta}\sqrt{\Delta F_{\mathrm{DC}}^2 - F_{\mathrm{C}}^2 J_{-r}^2\left(\frac{F_{\mathrm{AC}}}{\lambda\nu\zeta}\right)}, & \text{if} \quad |\Delta F_{\mathrm{DC}}| > \left| F_{\mathrm{C}} J_{-r}\left(\frac{F_{\mathrm{AC}}}{\lambda\nu\zeta}\right) \right|, \quad \Delta F_{\mathrm{DC}} \gtrless 0, \end{cases} \tag{22}$$

for $r = 0, \pm 1, \pm 2, \ldots$.

Appendix B. DDFT—further details

Implementation details: The finite volume partial differential equation solver FiPy 3.1 [62] is used to perform the integration of the Smoluchowski equation. The grid of the computer system consists of 10 000 cells and has a total length of 50 μm ($\approx$14 potential wells) with periodic boundary conditions. The computations were terminated whenever the probability distribution was so widely spread that effects of periodicity could not be neglected.

Initial conditions: The mean particle trajectory enters in general a short transient state before sychronising with the external AC driving force. This synchronised state is characterised by a periodic phase that modulates the linear drift of the mean trajectory. In order to suppress effects of the transient state we first estimate the mean position in the synchronised state of the respective system. Then we start the computation with a very narrow Gaussian function located in the determined position as the initial probability density $p(x,\ t = 0)$.

Effective diffusion coefficient: In the mode locked states the limit of equation (12) could not be reached within the time span of our computations due to intermediate plateaus as shown in figure 3(a). In these cases the linear increase of the plateaus for 500 oscillations was calculated and used to determine D_{eff}.

References

[1] Pikovsky A, Rosenblum M and Kurths J 2001 *Synchronization a Universal Concept in Nonlinear Sciences* (*Cambridge Nonlinear Science Series*) (Cambridge: Cambridge University Press)
[2] Birch T 1756 *The History of the Royal Society of London* (London: A Millar)
[3] Bennett M, Schatz M F, Rockwood H and Wiesenfeld K 2002 *Proc. R. Soc.* A **458** 563
[4] Agrawal D K, Woodhouse J and Seshia A A 2013 *Phys. Rev. Lett.* **111** 084101
[5] Neda Z, Ravasz E, Brechet Y, Vicsek T and Barabasi A L 2000 *Nature* **403** 849
[6] Neda Z, Ravasz E, Vicsek T, Brechet Y and Barabasi A L 2000 *Phys. Rev.* E **61** 6987
[7] Nicolis S C, Fernández J, Pérez-Penichet C, Noda C, Tejera F, Ramos O, Sumpter D J T and Altshuler E 2013 *Phys. Rev. Lett.* **110** 268104
[8] Feng X L, White C J, Hajimiri A and Roukes M L 2008 *Nat. Nanotechnol.* **3** 342
[9] Antonio D, Zanette D H and Lopez D 2012 *Nat. Commun.* **3** 806
[10] Shim S B, Imboden M and Mohanty P 2007 *Science* **316** 95
[11] Zalalutdinov M, Aubin K L, Pandey M, Zehnder A T, Rand R H, Craighead H G, Parpia J M and Houston B H 2003 *Appl. Phys. Lett.* **83** 3281
[12] Zhang M A, Wiederhecker G S, Manipatruni S, Barnard A, McEuen P and Lipson M 2012 *Phys. Rev. Lett.* **109** 233906
[13] Besseling R, Kes P H, Drose T and Vinokur V M 2005 *New J. Phys.* **7** 71
[14] Olson C J, Reichhardt C and Nori F 1998 *Phys. Rev. Lett.* **81** 3757
[15] Kokubo N, Besseling R and Kes P H 2004 *Phys. Rev.* B **69** 064504
[16] Kokubo N, Besseling R, Vinokur V M and Kes P H 2002 *Phys. Rev. Lett.* **88** 247004
[17] Kolton A B, Dominguez D and Gronbech-Jensen N 2001 *Phys. Rev. Lett.* **86** 4112
[18] Grigorieva I V 1994 *Supercond. Sci. Technol.* **7** 161
[19] Aubry S 1978 The new concept of transitions by breaking of analyticity in a crystallographic model *Solitons and Condensed Matter Physics* (*Springer Series in Solid-State Sciences*) ed T Bishop and A R Schneider (Berlin: Springer) pp 264–77
[20] Talkner P, Hershkovitz E, Pollak E and Hanggi P 1999 *Surf. Sci.* **437** 198
[21] Kvale M and Hebboul S E 1991 *Phys. Rev.* B **43** 3720
[22] Burkov S E 1991 *Phys. Rev.* B **44** 2850
[23] Grimes C C and Shapiro S 1968 *Phys. Rev.* **169** 397
[24] Josephson B D 1962 *Phys. Lett.* **1** 251
[25] Grüner G 1988 *Rev. Mod. Phys.* **60** 1129
[26] Carpinelli J M, Weitering H H, Plummer E W and Stumpf R 1996 *Nature* **381** 398
[27] Eichberger M, Schafer H, Krumova M, Beyer M, Demsar J, Berger H, Moriena G, Sciaini G and Miller R J D 2010 *Nature* **468** 799
[28] Sancho J M and Lacasta A M 2010 *Eur. Phys. J. Spec. Top.* **187** 49
[29] Dobnikar J, Snezhko A and Yethiraj A 2013 *Soft Matter* **9** 3693
[30] Simon A and Libchaber A 1992 *Phys. Rev. Lett.* **68** 3375
[31] Curran A, Lee M P, Leonardo R D and Padgett J M C M J 2012 *Phys. Rev. Lett.* **108** 240601

[32] Schmitt C, Dybiec B, Hänggi P and Bechinger C 2006 *Europhys. Lett.* **74** 937
[33] Babic D, Schmitt C, Poberaj I and Bechinger C 2004 *Europhys. Lett.* **67** 158
[34] Hennig D, Burbanks A D and Osbaldestin A H 2010 *Chem. Phys.* **375** 492
[35] Hasnain J, Jungblut S and Dellago C 2013 *Soft Matter* **9** 5867
[36] McDermott D, Amelang J, Lopatina L M, Reichhardt C J O and Reichhardt C 2013 *Soft Matter* **9** 4607
[37] Zaidouny L, Bohlein T, Roth R and Bechinger C 2013 *Soft Matter* **9** 9230
[38] Wang C L, Tekic J, Duan W S, Shao Z G and Yang L 2013 *J. Chem. Phys.* **138** 034307
[39] Tekic J and Mali P 2015 *The AC Driven Frenkel-Kontorova Model* (Serbia: Faculty of Science, University of Novi Sad)
[40] Pelton M, Ladavac K and Grier D G 2004 *Phys. Rev.* E **70** 031108
[41] Bohlein T, Mikhael J and Bechinger C 2012 *Nat. Mater.* **11** 126
[42] Lindenberg K, Lacasta A M, Sancho J M and Romero A H 2005 *New J. Phys.* **7** 29
[43] Shi N and Ugaz V M 2014 *Phys. Rev.* E **89** 012138
[44] Reguera D, Reimann P, Hanggi P and Rubi J M 2002 *Europhys. Lett.* **57** 644
[45] Tekic J and Hu B 2008 *Phys. Rev.* B **78** 104305
[46] Arzola A V, Volke-Sepúlveda K and Mateos J L 2013 *Phys. Rev.* E **87** 062910
[47] Herrera-Velarde S and Castaneda-Priego R 2008 *Phys. Rev.* E **77** 041407
[48] Lichtner K, Pototsky A and Klapp S H L 2012 *Phys. Rev.* E **86** 051405
[49] Chen J X and Jiao Z K 2007 *Chin. Phys. Lett.* **24** 1095
[50] Straube A V and Tierno P 2013 *Europhys. Lett.* **103** 28001
[51] Song K N, Wang H L, Ren J and Cao Y G 2015 *Physica* A **417** 102
[52] Ticco S V P, Fornasier G, Manini N, Santoro G E, Tosatti E and Vanossi A 2016 *J. Phys.: Condens. Matter* **28** 134006
[53] Juniper M P N, Straube A V, Besseling R, Aarts D G A L and Dullens R P A 2015 *Nat. Commun.* **6** 7187
[54] Juniper M P N, Besseling R, Aarts D G A L and Dullens R P A 2012 *Opt. Express* **27** 28707
[55] Juniper M P N, Straube A V, Aarts D G A L and Dullens R P A 2016 *Phys. Rev.* E **93** 012608
[56] Adler R 1946 *Proc. IRE* **34** 351
[57] Goldstein R E, Polin M and Tuval I 2009 *Phys. Rev. Lett.* **103** 168103
[58] Reichhardt C, Scalettar R T, Zimanyi G T and Gronbech-Jensen N 2000 *Physica* C **332** 1
[59] Marconi U M B and Tarazona P 1999 *J. Chem. Phys.* **110** 8032
[60] Archer A J and Evans R 2004 *J. Chem. Phys.* **121** 4246
[61] Español P and Löwen H 2009 *J. Chem. Phys.* **131** 244101
[62] Guyer J E, Wheeler D and Warren J A 2009 *Comput. Sci. Eng.* **11** 6
[63] Guo W, Du L-C, Mei D-C and Stat J 2014 *J. Stat. Mech.* P04025
[64] Marchenko I G and Marchenko I I 2012 *JETP Lett.* **95** 137
[65] Saikia S and Mahato M C 2009 *Phys. Rev.* E **80** 062102
[66] Lindenberg K, Sancho J M, Lacasta A M and Sokolov I M 2007 *Phys. Rev. Lett.* **98** 020602
[67] Emary R, Gernert C and Klapp S H L 2012 *Phys. Rev.* E **86** 061135
[68] Wiesenfeld K and Satija I 1987 *Phys. Rev.* B **36** 2483
[69] Crommie M F, Craig K, Sherwin M S and Zettl A 1991 *Phys. Rev.* B **43** 13699
[70] Hu B and Tekic J 2007 *Phys. Rev.* E **75** 056608
[71] Cotteverte J C, Bretenaker F and Lefloch A 1994 *Phys. Rev.* A **49** 2868
[72] Chow W W, Geabanacloche J, Pedrotti L M, Sanders V E, Schleich W and Scully M O 1985 *Rev. Mod. Phys.* **57** 61

Paper II Flow of colloidal solids and fluids through constrictions: dynamical density functional theory versus simulation

U. Zimmermann, F. Smallenburg, and H. Löwen,
Flow of colloidal solids and fluids through constrictions: dynamical density functional theory versus simulation,
J. Phys.: Condens. Matter **28**, 244019 (2016),
published by *IOP Publishing Ltd.*

Digital Object Identifier (DOI): /10.1088/0953-8984/28/24/244019

Link to version of record:
`http://iopscience.iop.org/article/10.1088/0953-8984/28/24/244019/meta`

Statement of contribution

UZ, FS, and HL developed the idea of this project. UZ designed the set-up and performed the numerical DDFT calculations supervised by HL. FS made the BD computer simulations. UZ, FS, and HL discussed the results and wrote the manuscript.

Copyright and license notice

IOP Publishing Journal of Physics: Condensed Matter

J. Phys.: Condens. Matter **28** (2016) 244019 (10pp) doi:10.1088/0953-8984/28/24/244019

Flow of colloidal solids and fluids through constrictions: dynamical density functional theory versus simulation

Urs Zimmermann, Frank Smallenburg and Hartmut Löwen

Institut für Theoretische Physik II: Weiche Materie, Heinrich-Heine-Universität Düsseldorf, D-40225 Düsseldorf, Germany

E-mail: Urs.Zimmermann@uni-duesseldorf.de

Received 30 November 2015, revised 12 February 2016
Accepted for publication 8 March 2016
Published 26 April 2016

Abstract

Using both dynamical density functional theory and particle-resolved Brownian dynamics simulations, we explore the flow of two-dimensional colloidal solids and fluids driven through a linear channel with a constriction. The flow is generated by a constant external force acting on all colloids. The initial configuration is equilibrated in the absence of flow and then the external force is switched on instantaneously. Upon starting the flow, we observe four different scenarios: a complete blockade, a monotonic decay to a constant particle flux (typical for a fluid), a damped oscillatory behaviour in the particle flux, and a long-lived stop-and-go behaviour in the flow (typical for a solid). The dynamical density functional theory describes all four situations but predicts infinitely long undamped oscillations in the flow which are always damped in the simulations. We attribute the mechanisms of the underlying stop-and-go flow to symmetry conditions on the flowing solid. Our predictions are verifiable in real-space experiments on magnetic colloidal monolayers which are driven through structured microchannels and can be exploited to steer the flow throughput in microfluidics.

Keywords: density functional theory, dynamical density functional theory, confinement, non-equilibrium, Brownian dynamics simulations

S Online supplementary data available from stacks.iop.org/JPhysCM/28/244019/mmedia

(Some figures may appear in colour only in the online journal)

1. Introduction

Particle flow through constrictions occurs in widely different situations ranging from nanofluidics [1–3] to medicine [4–6] and crowd management [7]. On the nanoscale, the permeation of molecules through pores is controlled by constrictions [8]. On the mesoscale, colloidal suspensions [9–11], dusty plasmas [12], and micron-sized bacteria [13, 14] passing through micro-patterned channels as well as vascular clogging by parasitized red blood cells [15] are important examples. Finally, in the macroscopic world, granulate fluxes through silos [16–19] and the escape of pedestrians or animals through narrow doors [20–23] illustrate the relevance of constricted flow phenomena.

Despite its relevance, flow through geometric constrictions is still not understood from a non-equilibrium statistical physics point of view within a fundamental microscopic theory. Classical density functional theory (DFT) [24–28] constitutes such a microscopic approach in equilibrium. In principle, DFT can be used to calculate the equilibrium phase diagram—including the freezing and melting lines—for given interparticle interactions and thermodynamic conditions (such as prescribed temperature and chemical potential). This is done by minimizing the appropriate free-energy functional with respect to the one-particle density distribution, which captures the structural properties of each phase. Although the theory is in practice approximative, as the exact functional is not known, there are very good approximation schemes

J. Phys.: Condens. Matter **28** (2016) 244019 U Zimmermann *et al*

(e.g. for hard spheres and hard disks) with remarkable predictive power [28–30]. A constriction can be conveniently modelled by an external curved wall, a set-up which can directly be accessed by density functional theory. Particle flow, however, is a non-equilibrium situation, such that standard equilibrium DFT cannot be applied directly. For completely overdamped Brownian dynamics, i.e. for mesoscopic colloidal particles in a solvent, it was shown that DFT can be generalized to describe the non-equilibrium relaxation dynamics of the time-dependent one-particle density [31–34]. The resulting dynamical density functional theory (DDFT) has been applied to a variety of non-equilibrium phenomena. These include colloids in external shear fields such they are advected by the solvent flow [35–39], microrheology where a particle is driven through a colloidal background [40], solvent-mediated hydrodynamic interactions [41–48], diffusion in hard sphere fluids at high volume fractions [49] and in binary mixtures [50], feedback control of colloids [51] and the collapse of a colloidal monolayer as governed by attractive interactions [52]. Moreover colloidal crystal growth [53–56] and quasicrystal growth [57, 58] (see [59] for a recent experiment) have been tackled by DDFT-like approaches. Finally, active colloids [60–63] and even granulate dynamics [64–68] have been described using DDFT.

In this paper, we apply DDFT to the flow of Brownian particles through a constriction. This is realized by colloidal particles flowing through microchannels [10, 11]. Here we restrict ourselves to two spatial dimensions and consider the flow of colloids in a stationary solvent, driven through a structured channel [69]. This model was motivated by experiments of superparamagnetic colloids in two dimensions [70, 71]. We use an equilibrium density functional for two-dimensional parallel dipoles similar to earlier work [72], which reproduces the fluid-solid transition in two dimensions. We then employ DDFT to describe a flow situation in a linear channel where particles are driven by a constant external force, such as gravity, and the solvent stays at rest. The channel includes a constriction, where the channel gets narrower. We systematically explore the influence of this constriction on the net particle flow, using both DDFT and Brownian dynamics computer simulations. In both methods, we equilibrate the system in the absence of flow, and measure the time-dependent flow through the constriction after instantaneously switching on the external driving force.

Within DDFT we find that the averaged flow through the constriction is qualitatively different for solids and fluids: in the fluid the flow is constant (i.e. time-independent) while in the solid it is periodically oscillating as a function of time. This interesting intermittent flow is induced by the constriction as it vanishes in the pure linear channel in the absence of any constriction. Therefore it is not a trivial passing of particle layers but rather a self-organized oscillation generated by the constraint breaking the one-dimensional translation symmetry along the channel. The computer simulations corroborate the theoretical findings qualitatively insofar as a different behaviour is revealed in the time-dependent flow in the solid and in the fluid. For solids there is an intermittent flow with damped oscillatory correlations in time while for fluids these oscillations are overdamped. This can be expected as DDFT is a mean-field theory which averages in a global and approximative sense, while the simulations contain explicit stochastic noise, responsible for damping the oscillatory behaviour.

In more detail, depending on the initial state (fluid or solid) and on the width of the constriction, we identify four different situations: (i) a complete blockade on the time scale of the calculations, (ii) a monotonic convergence to a constant particle flux (typical for a fluid), (iii) strongly damped oscillations in the particle flux, and (iv) a long-lived stop-and-go behaviour in the flow (typical for a solid). We attribute the underlying stop-and-go flow to symmetry conditions on the flowing solid by studying the case of five and six crystalline layers as an example. Our predictions are verifiable in real-space experiments on magnetic colloidal monolayers which are driven through structured microchannels, e.g. by gravity. They can further be exploited to steer the flow throughput in microfluidics and to tailor the pouring of colloidal particles through nozzles.

The paper is organized as follows: in section 2 we describe the details of the system under investigation. In section 3 the dynamical density functional theory approach is presented and in section 4 we describe the computer simulations. Results of both methods are presented and discussed in section 5. Our conclusions are presented in section 6.

2. The model

2.1. Interaction

We consider point-like Brownian particles in two spatial dimensions which interact via a pairwise potential

$$u(r) = \frac{u_0}{r^3}, \tag{1}$$

where r is the distance between two particles and the amplitude $u_0 > 0$ sets the interaction strength. A real-world analogue of this system is given by superparamagnetic particles that are confined in a $2d$ plane with an uniform external magnetic field $\mathbf{B}_{\text{ext}}$ applied perpendicular to the plane. The external magnetic field $\mathbf{B}_{\text{ext}}$ induces a dipole–dipole interaction between the colloidal particles, which can be tuned by changing its strength. In bulk, the only relevant length scale present in this system is the typical interparticle distance, which is given by

$$l = \rho_0^{-1/2}, \tag{2}$$

with

$$\rho_0 = N/A_0 \tag{3}$$

the number density of the system, N the number of particles, and A_0 the accessible area, which will be defined later. Due to the inverse power law scaling of equation (1), a change in density of the system is equivalent to a change in the interaction strength u_0. It is therefore convenient to rewrite equation (1) as

$$\frac{u(r)}{k_{\text{B}}T} = \frac{\Gamma}{(r/l)^3} \tag{4}$$

where $\Gamma = u_0\rho_0^{3/2}/(k_BT)$ is a dimensionless coupling parameter. The bulk phase behaviour of these particles is characterized by a fluid at low $\Gamma \lesssim 11$, and a hexagonally ordered solid phase at high $\Gamma \gtrsim 12$ [73, 74].

Naturally, this phase diagram is expected to change significantly in the confinement of a channel, as considered here. In particular, as the system is effectively one-dimensional, we expect only short-range ordering in the channel, and no true fluid to crystal transition. Nonetheless, at high Γ we do expect local ordering into a hexagonal lattice, aligned with the boundaries of the channel [74].

2.2. Channel confinement

Inside the $2d$ plane the particles are additionally confined in a channel geometry along the x-axis, represented by an external potential $V_{\text{ext}}(x, y)$. The lateral profile of the channel is modelled as error-function steps at the walls of the channel so the external potential is given by

$$V_{\text{ext}}(x,y) = V_0\left[1 - \frac{1}{2}\text{erf}\left(\frac{y+g(x)}{\sqrt{2}\,w}\right) + \frac{1}{2}\text{erf}\left(\frac{y-g(x)}{\sqrt{2}\,w}\right)\right], \tag{5}$$

with V_0 being the maximum potential height, $\pm g(x)$ describing the contour lines of the channel walls and w characterizing the softness of the walls. For a straight channel with width L_y and without constriction the contour functions are simply $g(x) \equiv \frac{L_y}{2}$. The constriction is modelled as a single cosine wave of length L_c at x_0 that is added smoothly to the channel contour. Therefore, $g(x)$ is given by

$$g(x) = \begin{cases} \dfrac{L_y}{2} - \alpha\left[1 + \cos\left(2\pi\dfrac{x-x_0}{L_c}\right)\right], \text{ if } |x-x_0| < \dfrac{L_c}{2} \\ \dfrac{L_y}{2}, \text{otherwise} \end{cases} \tag{6}$$

with amplitude $\alpha = \frac{L_y}{4}(1-b)$. Here, we introduced the parameter b as the ratio of constriction width over the total channel width. Consequently, $0 \leqslant b \leqslant 1$, where $b = 0$ refers to a completely blocked channel and $b = 1$ is a channel without constriction. See figure 1(a) for an illustrative sketch of $V_{\text{ext}}(x, y)$. Note that the form of the potential in equation (5) was chosen simply to provide a steeply repulsive wall-particle interaction. Experimentally, this can be realized via e.g. optical forces or barriers which are permeable to the solvent.

We define the accessible area as the region between the midlines of the two walls, i.e.

$$A_0 = 2\int_{-L_x/2}^{L_x/2} g(x)\mathrm{d}x. \tag{7}$$

By definition, the number density in the system is given by $\rho_0 = N/A_0 = 1/l^2$, with l our unit of length. In this work, we focus on channels with a width chosen such that either five or six crystalline layers reliably form within the channel, oriented such that lines of nearest-neighbours are aligned with the channel walls (see figure 1(b)). However, the number of

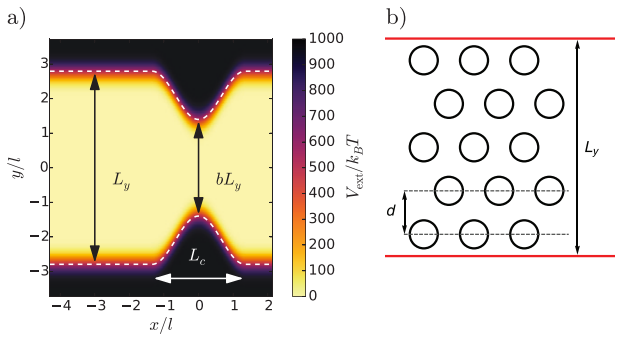

Figure 1. (a) Potential energy $V_{\text{ext}}(x, y)$ in the channel, for $b = 0.5$, $L_c = 2.686l$, $L_y = 6d$, $w = 0.25l$ and $x_0 = 0$. The dashed lines represent $\pm g(x)$ and enclose the accessible area A_0. (b) Schematic representation of the channel dimensions and the typical hexagonal lattice observed within the channel at high Γ. Note that d is defined in a perfect hexagonal lattice and may vary in the channel.

defects in this crystal strongly depends on the commensurability between the channel width and the lattice spacing of the crystal [74]. In a perfect hexagonal lattice at density $\rho_0 = 1/l^2$, the distance between two crystal layers is

$$d = \sqrt{\frac{\sqrt{3}}{2}}\,l, \tag{8}$$

and we will adopt this definition of d for our confined system as well. In order to accommodate a crystal with a low number of defects, we therefore choose the channel width to be $L_y = nd$, with $n = 5$ or 6. Both DDFT and simulations show that this indeed leads to crystals with the desired number of layers.

In order to further reduce parameter space, we fix the constriction length $L_c = 2.686l$, wall softness $w = 0.25l$ and $V_0 = 1000k_BT$.

2.3. Equations of motion

We model the dynamics of the particles in the channel via simple, overdamped Brownian dynamics, where we assume the solvent to be at rest. The equations of motions are given by:

$$\dot{\mathbf{r}}_i = \frac{D}{k_BT}\mathbf{F}_i(\mathbf{r}^N) + \sqrt{2D}\,\boldsymbol{\xi}_i(t), \tag{9}$$

where $\mathbf{r}_i$ are the coordinates of the ith particle and $\mathbf{r}^N \equiv (\mathbf{r}_1, \ldots, \mathbf{r}_N)$ is a short-hand notation for the coordinates of all particles, D is the diffusion constant of a single particle without external forces, $\mathbf{F}_i(\mathbf{r}^N)$ is the total force acting on the ith particle composed of pair interactions, external potential, and driving force:

$$\mathbf{F}_i = -\sum_{j\neq i}\nabla_i u(|\mathbf{r}_i - \mathbf{r}_j|) - \nabla_i V_{\text{ext}}(\mathbf{r}_i) + f\hat{\mathbf{x}}, \tag{10}$$

with $u(r)$ given by equation (4) and ∇_i being the gradient operator with respect to particle coordinates $\mathbf{r}_i$ and the unit vector in x-direction $\hat{\mathbf{x}}$. The external force responsible for the flow of particles through the channel is modelled via a constant force f along the x-axis. Finally, $\boldsymbol{\xi}_i(t)$ is a delta-correlated Gaussian noise process modelling the thermal fluctuations. In the remainder of this work, we will fix the driving force

$f = 1k_BT/l$. As a unit of time, we will use the time it takes a particle to diffuse by a typical distance of l, i.e.

$$\tau = \frac{l^2}{D}. \tag{11}$$

A stochastically equivalent description of equation (9) is given by the Smoluchowski picture in which the time-dependent N-particle probability distribution $p(\mathbf{r}^N, t)$ is considered. The Smoluchowski equation is given by

$$\frac{\partial p(\mathbf{r}^N, t)}{\partial t} = D\sum_{i=1}^{N} \nabla_i [k_BT\nabla_i + \mathbf{F}_i] p(\mathbf{r}^N, t). \tag{12}$$

An integration over the probability distribution $p(\mathbf{r}, t)$ with respect to all but one coordinate gives the one-particle density

$$\rho(\mathbf{r}_1, t) = N \int \mathrm{d}\mathbf{r}_2 \ldots \int \mathrm{d}\mathbf{r}_N p(\mathbf{r}^N, t), \tag{13}$$

which describes the ensemble averaged particle density at time t and is the basic quantity in the DDFT.

3. Dynamical density functional theory

3.1. General theory

Dynamical density functional theory (DDFT) is conveniently derived from the Smoluchowski equation (12) by projecting onto the one-particle density and invoking the additional adiabatic approximation [32]. As a result, DDFT is an approximative theory. It can be written as a continuity equation

$$\frac{\partial \rho(\mathbf{r}, t)}{\partial t} = D\nabla\left(\rho(\mathbf{r}, t)\nabla\frac{\delta\mathcal{F}[\rho]}{\delta\rho(\mathbf{r}, t)}\right), \tag{14}$$

which expresses the particle number concentration $\rho(\mathbf{r}, t)$. The current density $\mathbf{j}(\mathbf{r}, t)$ is explicitly given by a generalized Fick's law:

$$\mathbf{j}(\mathbf{r}, t) = -D\rho(\mathbf{r}, t)\nabla\frac{\delta\mathcal{F}[\rho]}{\delta\rho(\mathbf{r}, t)}, \tag{15}$$

with the Helmholtz free energy functional

$$\mathcal{F}[\rho] = \mathcal{F}_{\mathrm{id}}[\rho] + \mathcal{F}_{\mathrm{ext}}[\rho] + \mathcal{F}_{\mathrm{exc}}[\rho] \tag{16}$$

which can be split in three principal contributions. The ideal gas term

$$\mathcal{F}_{\mathrm{id}}[\rho] = k_BT \int \mathrm{d}\mathbf{r}\, \rho(\mathbf{r}, t)(\log(\Lambda^2\rho(\mathbf{r}, t)) - 1) \tag{17}$$

and the external potential contribution

$$\mathcal{F}_{\mathrm{ext}}[\rho] = \int \mathrm{d}\mathbf{r}\, \rho(\mathbf{r})(V_{\mathrm{ext}}(\mathbf{r}) - fx) \tag{18}$$

with thermal de Broglie wavelength Λ are known expressions. In contrast, the excess free energy functional $\mathcal{F}_{\mathrm{exc}}[\rho]$, which describes the particle interactions, is unknown and has to be approximated. Here, we use the Ramakrishnan–Yussouff functional described in the next section. Substituting the first two terms in equation (15), the current is thus given explicitly by

$$\mathbf{j}(\mathbf{r}, t) = -D\nabla\rho(\mathbf{r}, t) + \rho(\mathbf{r}, t)\nabla\left(V_{\mathrm{ext}}(\mathbf{r}) - fx + \frac{\delta\mathcal{F}_{\mathrm{exc}}[\rho]}{\delta\rho(\mathbf{r}, t)}\right). \tag{19}$$

Since we are only interested in the flux along the channel, we define the particle flow in the x-direction, i.e.

$$j_x(x, t) = \int_{-\infty}^{\infty} \mathrm{d}y\, \mathbf{j}(\mathbf{r}, t) \cdot \hat{\mathbf{x}}. \tag{20}$$

The average flow through the channel $\bar{j}_x$ can then simply be defined as the long-time average value of $j_x(x, t)$:

$$\bar{j}_x = \lim_{T\to\infty} \frac{1}{T} \int_0^T \mathrm{d}t\, j_x(x, t). \tag{21}$$

Note that as the particle density is a conserved quantity, $\bar{j}_x$ is independent of the position x.

3.2. Excess functional

We chose the Ramakrishnan–Yussouff expression [75] as an approximate excess free energy functional, which is a convenient way to model soft and long-ranged particle interactions. The functional derivative of the Ramakrishnan–Yussouff functional is given as a convolution of $\rho(\mathbf{r}, t)$ and the pair (two-point) direct correlation function $c_0^{(2)}(r; \rho_0, \Gamma)$ of an isotropic and homogeneous reference fluid with the prescribed density $\rho_0 = 1/l^2$, at interaction strength Γ:

$$\frac{\delta\mathcal{F}_{\mathrm{exc}}[\rho]}{\delta\rho(\mathbf{r}, t)} = -k_BT \int \mathrm{d}\mathbf{r}'\, \rho(\mathbf{r}', t) c_0^{(2)}(|\mathbf{r} - \mathbf{r}'|; \rho_0, \Gamma). \tag{22}$$

We use the direct correlation functions obtained by liquid integral theory with the Rogers–Young closure which were calculated in [76], where it was shown that despite its simplicity the Ramakrishnan–Yussouff functional accounts for the freezing transition in two dimensions at $\Gamma \gtrsim 36.2$.

Since the functional derivative of the excess functional equation (22) is a convolution of $\rho(\mathbf{r}, t)$ and $c_0^{(2)}(r; \rho_0, \Gamma)$ we can efficiently compute its value using fast Fourier transform.

3.3. Protocol

The overall length of the system is chosen as $L_x = 21.5l$ with periodic boundary conditions along the x-direction. As a discretisation we used $N_x \times N_y = 256 \times 64$ gridpoints. With prescribed density ρ_0 we have about $N = 113$–120 particles in our system, depending on the constriction width b.

Starting from several initial density profiles, we solve the DDFT equation without any driving force to obtain an equilibrium density profile $\rho^{(0)}(\mathbf{r})$. We confirmed that the equilibrium profile does not depend on the initial profile. Depending on the coupling parameter Γ we either obtain an inhomogeneous fluid (figure 2(a)) or a crystalline profile of hexagonal order (figure 2(b)). The one-dimensional crystal in channel confinement can be observed for $\Gamma \gtrsim 30$, for both investigated channel widths $L_y = 5d$ and $L_y = 6d$.

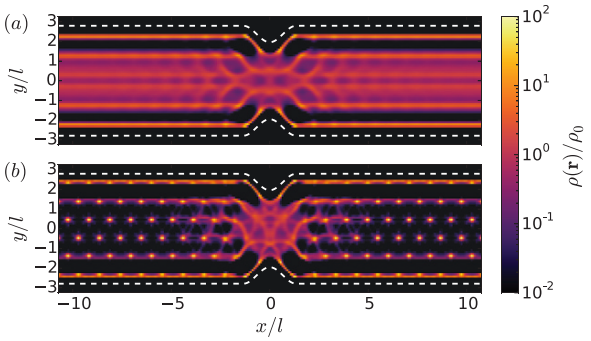

Figure 2. Equilibrium density profiles $\rho^{(0)}(\mathbf{r})$ as obtained from DDFT calculations without driving force ($f = 0$) for (a) low interaction strength $\Gamma = 20$ (fluid) and (b) high interaction strength $\Gamma = 60$ (solid) at $L_y = 6d$ and $b = 0.7$.

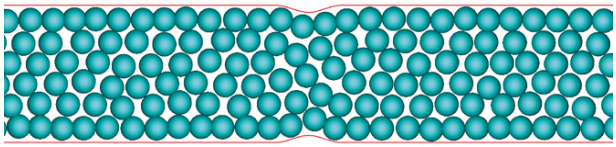

Figure 3. Typical simulation snapshot of the system after equilibration without flow at $\Gamma = 20$, $L_y = 6d$, and $b = 0.9$.

For $t > 0$ we switch on the driving force f, initiating the flow through the constriction. We solve equation (14) numerically using a finite volume partial differential equation solver [77].

4. Brownian dynamics simulations

In addition to DDFT calculations, we perform Brownian dynamics simulations of the same system. In particular, we simulate $N = 200$ particles with the same interparticle and particle-wall interactions as described above, using the equations of motion in equation (9). As in the DDFT calculations, we assume periodic boundary conditions along the x-direction. In our simulations, we randomly place the particles into the channel, and let the system equilibrate in the absence of an external flow ($f = 0$). At sufficiently high interaction strength Γ, this typically results in a rapid ordering of the particles into a hexagonal crystal-like structure aligned with the confining walls. It should be noted that even in the absence of a constriction, this crystal is never defect-free: the two layers closest to the walls typically contain significantly more particles than those in the interior layers. This can be attributed to the long-ranged repulsion between the particles. Part of a typical snapshot of an equilibrated crystal is shown in figure 3. Larger defects (such as local square ordering) are occasionally observed at very high Γ, where the system can get trapped into a local energy minimum. However, these defects typically vanish rapidly once the flow is started.

Upon turning on the flow in the channel, the particles start moving (on average) in the direction of the flow. After an initial relaxation time, the flow through the channel reaches a steady state. In order to quantitatively examine the flow of particles in the channel, we directly measure the particle flux $j_x(x = x_0, t)$ through the constriction by counting in each timestep the number of particles passing through $x = x_0$. We average this flux over a large number ($\sim 10^4$) of runs. To do this, we run the simulation with flow for 100 τ, then stop the flow and re-equilibrate the system first at a substantially lower effective interaction strength $\Gamma_{\text{relax}} = \Gamma/10$ in order to allow for significant particle reorganization, and then re-equilibrate again at the original Γ. We then restart the flow and perform another measurement. Averaging over these runs, we obtain flow relaxation profiles for a range of combinations of Γ and b.

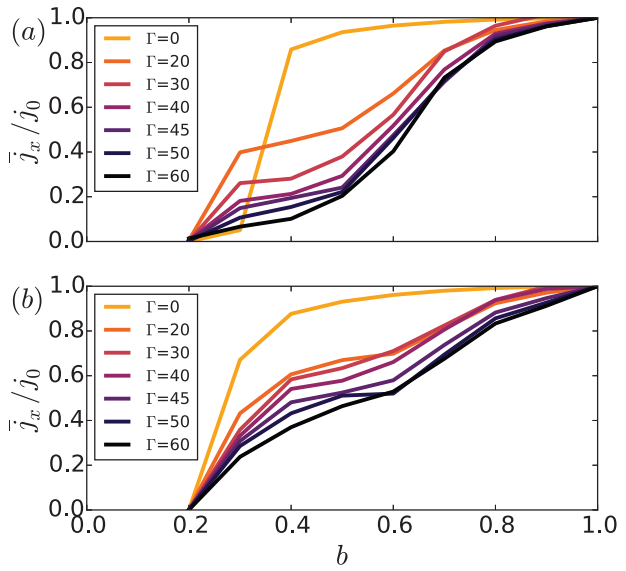

Figure 4. Average particle flux $\bar{j}_x$ along the channel, as obtained from DDFT for channel widths (a) $L_y = 5d$, and (b) $L_y = 6d$. The flux is normalized by the average flux of an unconstricted system along the channel j_0.

5. Results

5.1. Average flux

The average flux in the system $\bar{j}_x$ for a range of coupling parameters Γ and constriction widths b is shown in figures 4 and 5. In general, we observe that for stronger particle interactions the average flux is smaller, as the particles more effectively block each other from passing through the constriction. As expected, we also observe a decrease in average flux with decreasing constriction width b. We note, however, that in the simulations this trend is not always monotonic: there are regions where $\bar{j}_x$ decreases with increasing b.

We observe qualitative agreement between the DDFT and simulation results. The main difference occurs at high Γ, where the simulations observe complete blocking ($\bar{j}_x = 0$), while the DDFT calculations predict a finite flux. Additionally, the DDFT calculations predict only a monotonous increase in $\bar{j}_x$ with b for the investigated parameter range.

It should be noted here that the observed results are expected to be influenced strongly by the length of the channel: at constant number density, a longer channel implies that the driving

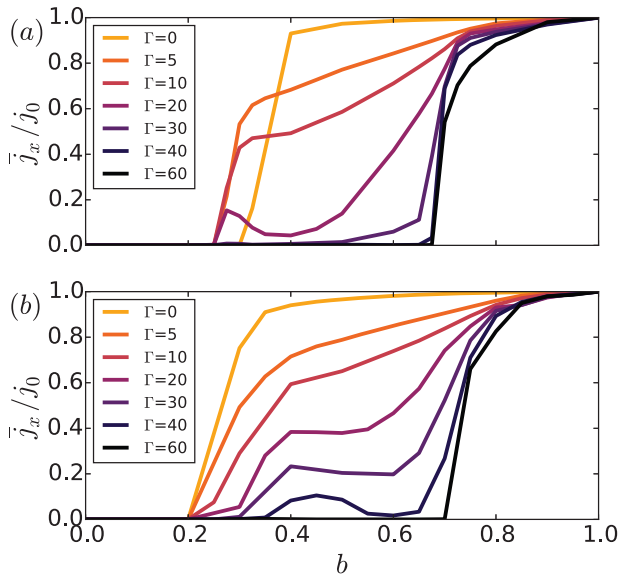

Figure 5. Average particle flux $\bar{j}_x$ in the channel, as obtained from Brownian dynamics simulations for channel widths (a) $L_y = 5d$, and (b) $L_y = 6d$. The flux is normalized by the average flux of free particles in an unconstricted channel j_0.

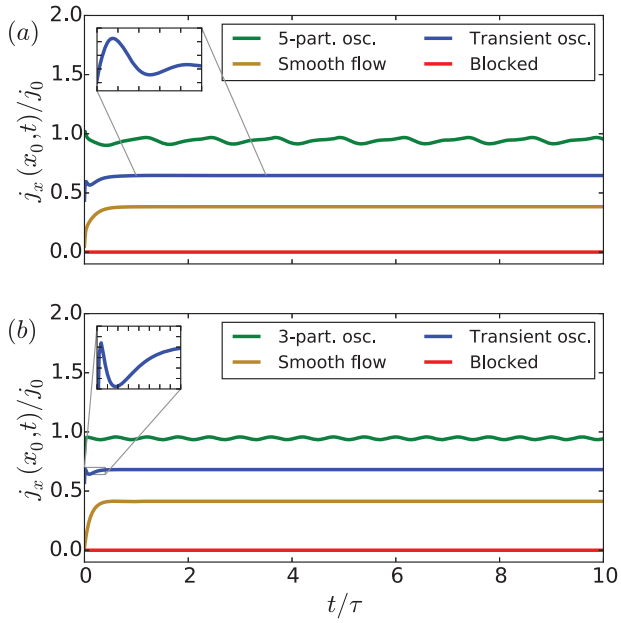

Figure 6. Average particle flux $j_x(x_0, t)$ along the channel through the constriction as a function of time t elapsed since starting the flow, as obtained from DDFT calculations for channel widths (a) $L_y = 5d$, and (b) $L_y = 6\,d$ for $\Gamma = 30$, $b = 0.9$ (top, green) and $\Gamma = 20$ with constriction width $b = 0.6$, 0.3 and 0.2 (bottom, red). These selected examples illustrate the different states as shown in figure 8. The flux is normalized by its average value j_0 in an unconstricted channel (i.e. $\bar{j}_x$ at $b = 1$) at the same f. The inset shows a zoom of the particle flux in the transient state and highlights a weak and decaying oscillation.

force f is applied to a larger number of particles in front of the constriction. This results in a proportional increase in the pressure near the constriction, which is expected to enhance

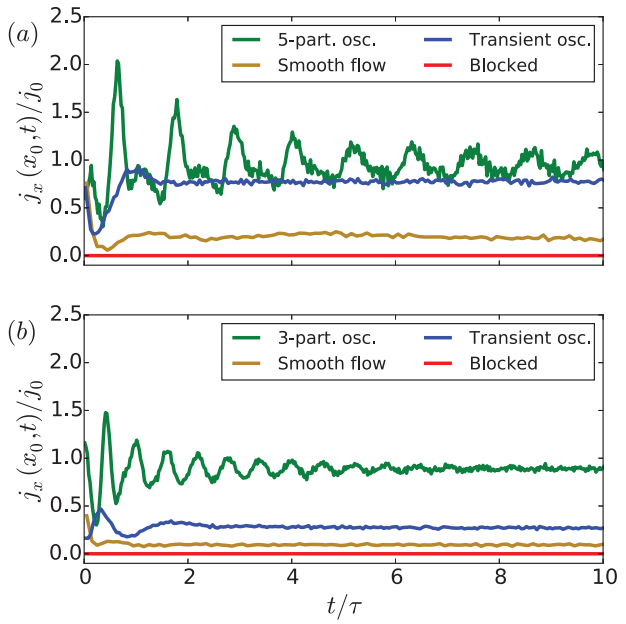

Figure 7. Plots of the average particle flux $j_x(x_0, t)$ through the middle of the constriction as a function of time t elapsed since starting the flow, as obtained from Brownian dynamics simulations for channel widths (a) $L_y = 5d$, with $\Gamma = 20$, and (b) $L_y = 6d$, with $\Gamma = 40$. For both widths, the constriction widths are given by $b = 0.8$ (top, green), 0.7, 0.5 and 0.2 (bottom, red). The flux is normalized by its average value in an unconstricted channel (i.e. $\bar{j}_x$ at $b = 1$) at the same f.

the flow of particles. Indeed, simulations on larger systems ($N = 400$) and on systems with larger external forces confirm that doubling the channel length is approximately equivalent to doubling the external driving force on the particles.

5.2. Flow behavior

After starting the flow, we observe four qualitatively different types of flow behavior in both our DDFT results and our simulations. First, we distinguish between systems that show a complete blockade (i.e. zero particle flow $\bar{j}_x$), and systems that show a finite flow of particles. In the case of a finite flow, the average flux through the constriction eventually reaches a constant value in the simulations. However, shortly after starting the flow, we often observe oscillations in the flux that decay over time. In this regime, we observe three types of decay: an almost immediate decay to a smooth flow, a brief period of transient oscillations without a clearly defined periodicity, and a long-time oscillation with a period which is independent of b and Γ. In the DDFT calculations we observe the same regimes. However, due to the lack of stochastic noise, in the long-time oscillation regime, the DDFT calculations predict periodic (i.e. non-decaying) oscillations. Below, we discuss each type of flow in detail. In figures 6 and 7, we plot the average flux through the constriction as a function of time as obtained from DDFT and simulations, respectively, for each of the four types of flow, and for channel widths $L_y = 5d$ and $L_y = 6d$. Additionally, in figure 8, we show state diagrams

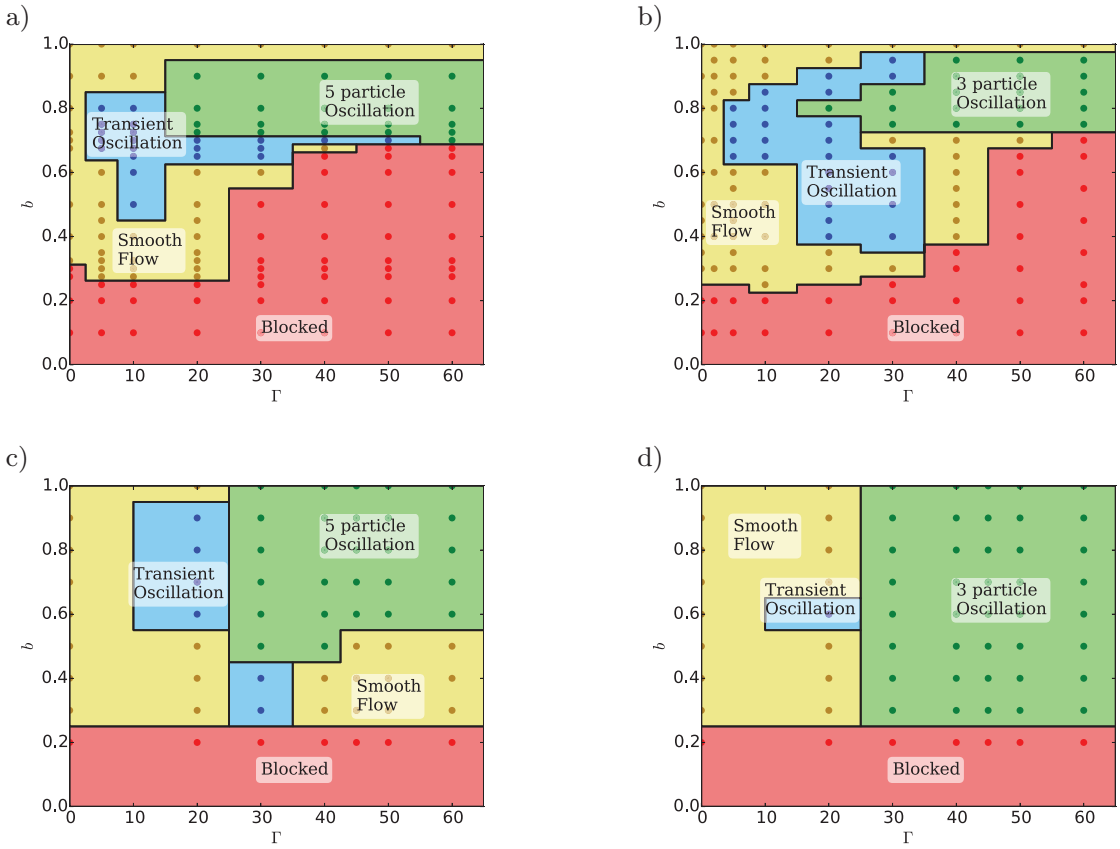

Figure 8. State diagrams indicating the types of flow observed for channels of width (a), (c) $L_y = 5d$ and (b), (d) $L_y = 6d$, as obtained from Brownian dynamics simulations (a), (b) and DDFT calculations (c), (d). The dark coloured points indicate points where DDFT calculation and simulations were performed.

for the same two channel widths from both simulations and DDFT, where we show the type of flow observed for a range of investigated values of b and Γ.

5.2.1. Blockade. A blockade of the particle flow in the system (as observed on the time scale of the calculation) occurs at narrow constrictions $b \lesssim 0.2$ for all Γ. This is an effect of the softness of the confining potential V_{ext}. Due to this softness, a potential barrier on the order $k_{\text{B}}T$ starts appearing in the center of the channel around $b \simeq 0.3$ for both channel widths considered, which increases rapidly for smaller b.

For high particle interaction strengths $\Gamma \gtrsim 40$ an additional blockade situation for wider constrictions can be observed in the computer simulations. At sufficiently high Γ, the highly ordered lattice resists the deformations necessary to allow the flow of particles through the constriction. In the DDFT calculations, this effect is not observed, likely due to the insufficient treatment of particle correlations within the Ramakrishnan–Yussouff approximation.

5.2.2. Smooth flow. This flow behavior is characterised by an overdamped transient flow that converges to a constant level almost immediately. It can be observed in the fluid phase at intermediate constriction widths. For larger Γ values we can find the smooth flow behavior also in the 5 layer DDFT system and the 6 layer simulation system.

5.2.3. Three or five-particle Oscillation. For intermediate to strong particle interactions and for intermediate to wide constrictions we observe strong oscillatory behavior in the particle flow. While in the Brownian dynamics simulations the oscillation is damped we can find for the DDFT results an undamped oscillation that is periodic after a brief transient phase. This can be understood from the fact that the damping in the simulation is due to the presence of fluctuations, which are missed in the mean-field approach of the DDFT. We expect that the fluctuations which destroy long-ranged periodic order in one dimension are also responsible for washing out the correlations in the flow dynamics. The frequency of the oscillation depends on the number of particle layers in the system. For a five layer system the frequency is lower and corresponds to five particles passing the constriction during one oscillation period. In contrast, in the six layer system we observe a higher frequency in the flow oscillation, corresponding to three particles passing the constriction. In figure 9 we illustrate the mechanism that is responsible for this qualitative difference. For both channel widths, the oscillation period represents the smallest number of particles that can pass through the constriction in such a way that the system reverts to its original configuration. In the case of an odd number of layers (i.e. five), this is simply five particles, such that the crystalline lattice shifts by one lattice spacing. For an even number of crystalline layers (i.e. $L_y = 6d$), this period instead

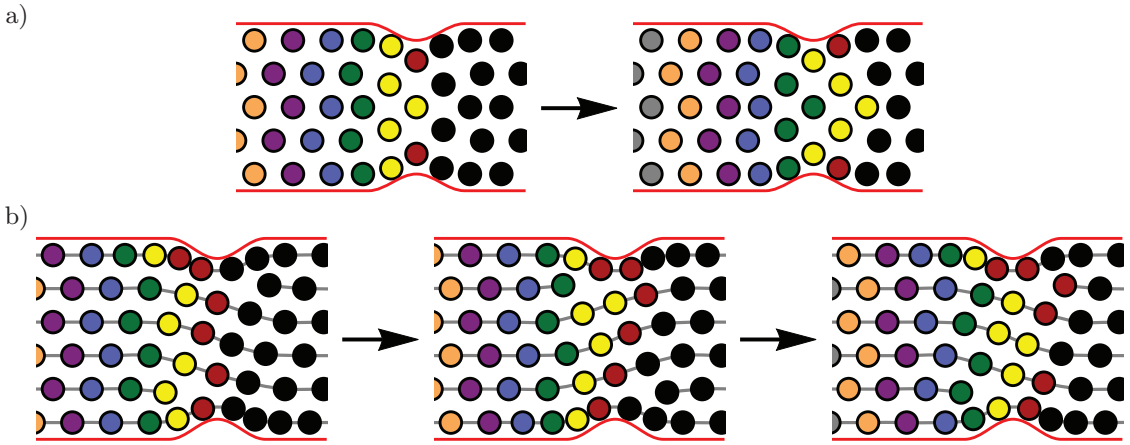

Figure 9. Schematic picture of the periodic flow of the crystal observed for high interaction strength Γ and wide constrictions (large b). The figures are idealized snapshots of the system separated in time by exactly one oscillation period. Flow is from left to right. (a) For a channel width $L_y = 5d$, five crystal layers form, and one oscillation corresponds to the movement of the crystal by one lattice spacing. During this time, each particle assumes the position of the particle in front of it. (b) For a crystal with six layers ($L_y = 6d$), one oscillation period corresponds to the movement of the crystal by half of a lattice spacing. Note that in the case of six layers, the up-down symmetry in the system is broken, and we observe two symmetric dislocations in the crystal pattern, as indicated by the gray lattice lines. After one oscillation, the locations of the particles (and dislocations) are vertically mirrored with respect to the initial configuration (middle snapshot). After the next oscillation (right snapshot), we recover the original configuration. Note that for both channel widths, the higher concentration of particles in the top and bottom layers of the crystal results in a lower velocity of the particles in those layers.

corresponds to three particles passing through the constriction, such that the lattice moves by half a lattice spacing, and then coincides with a vertically mirrored version of the initial lattice. We have confirmed with simulations that the same mechanism occurs for other (small) numbers of layers.

In the supplementary material stacks.iop.org/JPhysCM/28/244019/mmedia we include two movies of these dynamics in a system with $L_y = 6d$ and $b = 0.8$ as obtained from DDFT and simulations.

As can be seen in figure 8, in our DDFT findings this type of oscillatory flow is dominant in a significantly larger region of the (b, Γ) parameter space. In the simulations, this mechanism only occurs around $b \simeq 0.8$. Likely, this can be attributed to the approximative excess functional which cannot account for complex crystal configurations that are responsible for the blockade in front of the constriction.

5.2.4. Transient oscillation. In addition to the overdamped decay to a smooth flow and the long-time mechanism described above, we also observe short transient fluctuations that converge to a constant level within a few oscillations. Unlike the smooth flow the transient regime is not overdamped but performs several oscillations around the final level. It can be found for intermediate particle interaction strengths and wide constrictions. Note that while these transient oscillations are clearly distinguishable from the long-term fluctuations described above via their period, the distinction between the overdamped decay to a smooth flow and these transient fluctuations are often less clear. In particular, in the simulations, the presence of statistical noise makes determining the presence of secondary or tertiary peaks in the flow profile difficult if their amplitude is small. Due to the absence of statistical noise in the DDFT calculations transient fluctuations are better distinguishable from the smooth flow.

6. Conclusions

In conclusion, we have explored the flow of two-dimensional solids and fluids through constrictions on a particle-resolved level by using models describing the Brownian dynamics of strongly interacting colloids in a linear channel. Upon starting the flow, four different situations were identified using dynamical density functional theory and particle-resolved computer simulations: (i) a complete blockade, (ii) a smooth flow, (iii) an oscillatory behaviour in the particle flux, (iv) a long-lived stop-and-go behaviour in the flow. Though the dynamical density functional theory is an approximative mean-field theory, it qualitatively describes most of the states and trends.

Our predictions can be confirmed by using magnetic colloidal particles driven through microchannels [11, 78] as already used for the flow over energetic barriers but in the absence of constrictions [79]. For this realization, flow and diffusion through linear channels involving 4–8 layers has been considered before [80–82] and a layer reduction was found. Although an extreme geometric narrowing in the channel was not studied in previous work, this could in principle be done by using micropatterned channels [10].

Future work should address three-dimensional constrictions (like an colloidal hour-glass) although clearly the numerical evaluation of DDFT in three dimensions is harder. It would be nice to explore colloidal mixtures driven through constrictions [83] where we expect a rich scenario of flow states depending on the microscopic interactions.

We note that in our model the constriction was seen only by the colloids only but not by the solvent. Such barriers can be prepared using laser-optical forces which only act on the colloids but are invisible by the solvent, i.e. they allow for a full solvent penetration. Real geometric constrictions governed by the shape of the channel also affect the solvent flow.

The same is true when the flow is generated by a pressure gradient in the solvent. These situations require a more detailed modelling regarding the solvent flow field which provides additional advective drag forces to the colloids. For a single particle moving through a constriction, the solvent effect was taken into account by Martens and coworkers [84, 85], for another situation see [86]. More realistic calculations which include the hydrodynamics of the solvent and the hydrodynamic interactions between the colloids are still to be done in future studies.

Acknowledgments

This work was financially supported by the ERC Advanced Grant INTERCOCOS (Grant No. 267499). FS acknowledges support from the Alexander von Humboldt-Foundation.

References

[1] Eijkel J C T and van den Berg A 2005 *Microfluid. Nanofluid.* **1** 249
[2] Schoch R B, Han J and Renaud P 2008 *Rev. Mod. Phys.* **80** 839
[3] Bocquet L and Charlaix E 2010 *Chem. Soc. Rev.* **39** 1073
[4] Fallah M A, Myles V M, Krüger T, Sritharan K, Wixforth A, Varnik F, Schneider S W and Schneider M F 2010 *Biomicrofluidics* **4** 024106
[5] Noguchi H, Gompper G, Schmid L, Wixforth A and Franke T 2010 *Europhys. Lett.* **89** 28002
[6] Bernabeu M O, Nash R W, Groen D, Carver H B, Hetherington J, Krüger T and Coveney P V 2013 *Interface Focus* **3** 0120094
[7] Peacock R D, Kuligowski E D and Averill J D 2011 *Pedestrian and Evacuation Dynamics* 1st edn (Berlin: Springer) p 910
[8] Dzubiella J and Hansen J P 2005 *J. Chem. Phys.* **122** 234706
[9] Wyss H M, Blair D L, Morris J F, Stone H A and Weitz D A 2006 *Phys. Rev.* E **74** 061402
[10] Genovese D and Sprakel J 2011 *Soft Matter* **7** 3889
[11] Kreuter C, Siems U, Nielaba P, Leiderer P and Erbe A 2013 *Eur. Phys. J. Spec. Top.* **222** 2923
[12] Ivlev A V, Löwen H, Morfill G E and Royall C P 2012 *Complex Plasmas and Colloidal Dispersions: Particle-Resolved Studies of Classical Liquids and Solids* (*Series in Soft Condensed Matter* vol 5) 1st edn (Singapore: World Scientific) p 336
[13] Hulme S E, DiLuzio W R, Shevkoplyas S S, Turner L, Mayer M, Berg H C and Whitesides G M 2008 *Lab Chip* **8** 1888
[14] Altshuler E, Mino G, Pérez-Penichet C, del Río L, Lindner A, Rousselet A and Clément E 2013 *Soft Matter* **9** 1864
[15] Patnaik J K, Das B S, Mishra S K, Mohanty S, Satpathy S K and Mohanty D 1994 *Am. J. Trop. Med. Hyg.* **51** 642
[16] Zuriguel I, Janda A, Garcimartín A, Lozano C, Arévalo R and Maza D 2011 *Phys. Rev. Lett.* **107** 278001
[17] Thomas C C and Durian D J 2015 *Phys. Rev. Lett.* **114** 178001
[18] Tang J and Behringer R P 2015 arXiv:1510.07940
[19] Lumay G, Schockmel J, Henndez-Enrquez D, Dorbolo S, Vandewalle N and Pacheco-Vzquez F 2015 *Pap. Phys.* **7** 070013
[20] Helbing D, Farkas I and Vicsek T 2000 *Nature* **407** 487
[21] Kirchner A, Nishinari K and Schadschneider A 2003 *Phys. Rev.* E **67** 056122
[22] Zuriguel I, Parisi D R, Hidalgo R C, Lozano C, Janda A, Gago P A, Peralta J P, Ferrer L M, Pugnaloni L A, Clément E, Maza D, Pagonabarraga I and Garcimartín A 2014 *Sci. Rep.* **4** 7324
[23] Garcimartín A, Pastor J M, Ferrer L M, Ramos J J, Martín-Gómez C and Zuriguel I 2015 *Phys. Rev.* E **91** 022808
[24] Evans R 1979 *Adv. Phys.* **28** 143
[25] Löwen H 1994 *Phys. Rep.* **237** 249
[26] Singh Y 1991 *Phys. Rep.* **207** 351
[27] Tarazona P, Cuesta J A and Martínez-Ratón Y 2008 *Theory and Simulation of Hard-Sphere Fluids and Related Systems* (*Lecture Notes in Physics* vol 753) 1st edn, ed Á Mulero (Berlin: Springer) chapter 7, pp 247–341
[28] Roth R 2010 *J. Phys.: Condens. Matter* **22** 063102
[29] Oettel M, Görig S, Härtel A, Löwen H, Radu M and Schilling T 2010 *Phys. Rev.* E **82** 051404
[30] Härtel A, Oettel M, Rozas R E, Egelhaaf S U, Horbach J and Löwen H 2012 *Phys. Rev. Lett.* **108** 226101
[31] Marconi U M B and Tarazona P 1999 *J. Chem. Phys.* **110** 8032
[32] Archer A J and Evans R 2004 *J. Chem. Phys.* **121** 4246
[33] Espanol P and Löwen H 2009 *J. Chem. Phys.* **131** 244101
[34] Wittkowski R, Löwen H and Brand H R 2010 *Phys. Rev.* E **82** 031708
[35] Rauscher M, Domínguez A, Krüger M and Penna F 2007 *J. Chem. Phys.* **127** 244906
[36] Brader J and Krüger M 2011 *Mol. Phys.* **109** 1029
[37] Krüger M and Brader J M 2011 *Europhys. Lett.* **96** 68006
[38] Reinhardt J, Weysser F and Brader J M 2013 *Europhys. Lett.* **102** 28011
[39] Aerov A A and Krüger M 2014 *J. Chem. Phys.* **140** 094701
[40] Almenar L and Rauscher M 2011 *J. Phys.: Condens. Matter* **23** 184115
[41] Rex M and Löwen H 2008 *Phys. Rev. Lett.* **101** 148302
[42] Rex M and Löwen H 2009 *Eur. Phys. J.* E **28** 139
[43] Rauscher M 2010 *J. Phys.: Condens. Matter* **22** J4109
[44] Goddard B D, Pavliotis G A and Kalliadasis S 2012 *Multiscale Model. Simul.* **10** 633
[45] Goddard B D, Nold A, Savva N, Pavliotis G A and Kalliadasis S 2012 *Phys. Rev. Lett.* **109** 120603
[46] Goddard B D, Nold A, Savva N, Yatsyshin P and Kalliadasis S 2013 *J. Phys.: Condens. Matter* **25** 035101
[47] Goddard B D, Nold A and Kalliadasis S 2013 *J. Chem. Phys.* **138** 144904
[48] Donev A and Vanden-Eijnden E 2014 *J. Chem. Phys.* **140** 234115
[49] Stopper D, Marolt K, Roth R and Hansen-Goos H 2015 *Phys. Rev.* E **92** 022151
[50] Malijevsky A and Archer A J 2013 *J. Chem. Phys.* **139** 144901
[51] Lichtner K, Pototsky A and Klapp S H L 2012 *Phys. Rev.* E **86** 051405
[52] Bleibel J, Dominguez A, Oettel M and Dietrich S 2014 *Soft Matter* **10** 4091
[53] van Teeffelen S, Likos C N and Löwen H 2008 *Phys. Rev. Lett.* **100** 108302
[54] van Teeffelen S, Backofen R, Voigt A and Löwen H 2009 *Phys. Rev.* E **79** 051404
[55] Neuhaus T, Schmiedeberg M and Löwen H 2013 *New J. Phys.* **15** 073013
[56] Neuhaus T, Schmiedeberg M and Löwen H 2013 *Phys. Rev.* E **88** 062316
[57] Achim C V, Schmiedeberg M and Löwen H 2014 *Phys. Rev. Lett.* **112** 255501
[58] Archer A J, Rucklidge A M and Knobloch E 2015 *Phys. Rev.* E **92** 012324
[59] Nagao K, Inuzuka T, Nishimoto K and Edagawa K 2015 *Phys. Rev. Lett.* **115** 075501
[60] Wensink H H and Löwen H 2008 *Phys. Rev.* E **78** 031409
[61] Wittkowski R and Löwen H 2011 *Mol. Phys.* **109** 2935
[62] Menzel A M and Löwen H 2013 *Phys. Rev. Lett.* **110** 055702
[63] Menzel A M, Saha A, Hoell C and Löwen H 2016 *J. Chem. Phys.* **144** 024115

[64] Marconi U M B and Melchionna S 2007 *J. Chem. Phys.* **126** 184109
[65] Marconi U M B, Tarazona P, Cecconi F and Melchionna S 2008 *J. Phys.: Condens. Matter* **20** 494233
[66] Marconi U M B and Melchionna S 2009 *J. Chem. Phys.* **131** 014105
[67] Marconi U M B and Melchionna S 2010 *J. Phys.: Condens. Matter* **22** 364110
[68] Marconi U M B and Melchionna S 2014 *Commun. Theor. Phys.* **62** 596
[69] Piacente G and Peeters F M 2005 *Phys. Rev.* B **72** 205208
[70] Straube A V, Louis A A, Baumgartl J, Bechinger C and Dullens R P A 2011 *Europhys. Lett.* **94** 48008
[71] Juniper M P, Straube A V, Besseling R, Aarts D G and Dullens R P 2015 *Nat. Commun.* **6** 7187
[72] van Teeffelen S, Likos C N, Hoffmann N and Löwen H 2006 *Europhys. Lett.* **75** 583
[73] Kalia R K and Vashishta P 1981 *J. Phys.* C **14** L643
[74] Haghgooie R and Doyle P S 2004 *Phys. Rev.* E **70** 061408
[75] Ramakrishnan T V and Yussouff M 1979 *Phys. Rev.* B **19** 2775
[76] Van Teeffelen S, Löwen H and Likos C N 2008 *J. Phys.: Condens. Matter* **20** 404217
[77] Guyer J E, Wheeler D and Warren J A 2009 *Comput. Sci. Eng.* **11** 6
[78] Siems U, Kreuter C, Erbe A, Schwierz N, Sengupta S, Leiderer P and Nielaba P 2012 *Sci. Rep.* **2** 1015
[79] Kreuter C, Siems U, Henseler P, Nielaba P, Leiderer P and Erbe A 2012 *J. Phys.: Condens. Matter* **24** 464120
[80] Köppl M, Henseler P, Erbe A, Nielaba P and Leiderer P 2006 *Phys. Rev. Lett.* **97** 208302
[81] Henseler P, Erbe A, Köppl M, Leiderer P and Nielaba P 2010 *Phys. Rev.* E **81** 041402
[82] Wilms D, Virnau P, Snook I K and Binder K 2012 *Phys. Rev.* E **86** 051404
[83] Glanz T, Wittkowski R and Löwen H 2015 arXiv:1511.02939
[84] Martens S, Straube A V, Schmid G, Schimansky-Geier L and Hänggi P 2013 *Phys. Rev. Lett.* **110** 010601
[85] Martens S, Straube A V, Schmid G, Schimansky-Geier L and Hänggi P 2014 *Eur. Phys. J. Spec. Top.* **223** 3095
[86] Malgaretti P, Pagonabarraga I and Rubi J M 2014 *Phys. Rev. Lett.* **113** 128301

Flow of colloidal solids and fluids through constrictions: dynamical density functional theory versus simulation: Supplemental Information

Urs Zimmermann, Frank Smallenburg and Hartmut Löwen

Included movie files:

- DDFT.avi – DDFT calculation of a density distribution with high interaction strength ($\Gamma = 60$) driven through a constriction ($b = 0.8$) at channel width $L_y = 6d$.

- simulation.avi – BD simulation of strongly interacting particles ($\Gamma = 60$) driven through a constriction ($b = 0.8$) at channel width $L_y = 6d$.

Paper III Negative resistance for colloids driven over two barriers in a microchannel

U. Zimmermann, H. Löwen, C. Kreuter, A. Erbe, P Leiderer, and F. Smallenburg,
Negative resistance for colloids driven over two barriers in a microchannel,
submitted to Phys. Rev. Lett. (2017),
preprint published at *arXiv:* 1709.09711.

Link to preprint version:
`https://arxiv.org/abs/1709.09711`

Statement of contribution

CK, PL, and HL initiated this project. UZ, HL, and FS developed the project further. CK performed the experiments under supervision of AE and PL. UZ computed the numerical DDFT results and derived the analytical solution. FS contributed Brownian dynamics computer simulation data. UZ, HL, FS, PL, and AE discussed the results. UZ, HL, and FS wrote the manuscript.

Copyright and license notice

Negative resistance for colloids driven over two barriers in a microchannel

Urs Zimmermann,[1,*] Hartmut Löwen,[1] Christian Kreuter,[2] Artur Erbe,[3] Paul Leiderer,[2] and Frank Smallenburg[1]

[1] *Institut für Theoretische Physik II: Weiche Materie, Heinrich-Heine-Universität Düsseldorf, D-40225 Düsseldorf, Germany*
[2] *Fachbereich Physik, Universität Konstanz, D-78457 Konstanz, Germany*
[3] *Institut für Ionenstrahlphysik und Materialforschung, Helmholtz-Zentrum Dresden-Rossendorf, D-01328 Dresden, Germany*

(Dated: September 29, 2017)

Ohm's law is one of the most central transport rules stating that the total resistance of sequential single resistances is additive. Here we test additivity of resistances in classical systems of interacting colloids driven over two energetic barriers in a microchannel, using real-space microscopy experiments, particle-resolved simulations, and dynamical density functional theory. If the barrier separation is comparable to the particle correlation length, the resistance is highly non-additive, such that the added resistance of the second barrier can be significantly higher or lower than that of the first. Surprisingly, for a barrier separation comparable to the particle interaction range, the second barrier can add a *negative* resistance, such that two identical barriers are easier to cross than a single one. We explain our results in terms of the structuring of particles trapped between the barriers.

One of the basic characteristics of any transport situation is the resistance, commonly known from electric circuits, which is in general defined as the ratio of the transport flux and the driving force, typically in the linear-response regime of small drives. For both electric circuits and classical transport, Ohm's law states that when resistors are put in series, their resistances simply add up. However, this macroscopic law is expected to break down on the microscopic scale, in particular when the distance between the two obstacles approaches the correlation length of the transported particles.

Knowing and controlling flow resistance is of particular importance when tuning the transport of solutes through channels. This type of transport is the basic situation in microfluidics [1], where the transported objects are typically micron-sized colloidal solutes, such that thermal fluctuations play a significant role [2]. Moreover, there are many other examples where individual "particles" (or agents) are propagating through channels. Examples include macroscopic objects like cars or pedestrians [3], animals [4] and bacteria [5–7] migrating collectively through channels, and the transport of ions through membranes via nanopores [8]. Obstacles in such channels naturally inhibit the overall steady-state rate at which the particles are able to traverse the channel, providing an effective resistance to the flow. In channels with multiple obstacles, we expect Ohmic (i.e. additive) behavior of the corresponding resistances when the separation between the obstacles is large, and a breakdown of Ohm's law for smaller distances. The crossover between these regimes is determined by the correlation length in the system, i.e. the length scale associated with local structure in the fluid of transported particles. Detailed knowledge of these non-additive effects is of vital importance for the design of efficient microfluidic devices, as well as for our broader understanding of constricted flow phenomena.

In this Letter, we explore the additivity of resistances in mesoscopic colloidal suspensions driven through a microchannel [9]. We first perform an experiment on repulsive colloidal particles confined to microchannels containing two step-like barriers on the substrate, and measure the current through the channels as a function of the strength of the gravitational driving force. Subsequently, we employ Brownian dynamics simulations and dynamical density functional theory to systematically explore the interplay between the two barriers. Our results show strong deviations from additivity for the resistance of two barriers when the separation between the two obstacles is comparable to the correlation length of the system, which is on the order of several interparticle spacings. Amazingly, if the barrier separation is comparable to the interaction range, we discover that the resistance contributed by the second barrier can even be *negative*. We explain this counterintuitive effect of negative resistance via the long-ranged particle interactions and the ordering of the particles trapped between the two barriers. When these particles are disordered, they exhibit spontaneous fluctuations which modulate their interactions with particles crossing the barriers, significantly enhancing barrier crossing rates [10, 11]. This surprising phenomenon provides a route for tuning and enhancing particle flow over an obstacle by the inclusion of additional barriers, reminiscent of the use of geometric obstacles to assist e.g. the flow of panicked crowds [12].

In our experiment, colloidal superparamagnetic particles are confined in a microchannel with obstacles, prepared using molds made via microlithography [9, 13], see Fig. 1. The experimental cell consists of two rectangular reservoirs, connected by multiple channels (to improve statistics). The colloidal particles are restricted to two-dimensional in-plane motion due to gravity. In each channel up to two U–shaped step-like barrier structures are

implemented perpendicular to the channel, for details see Supplemental Material [14]. A uniform external magnetic field $\mathbf{B}_{\text{ext}}$ is applied in the direction perpendicular to the plane in which the particles move. This magnetic field induces purely repulsive interactions between the colloidal particles.

We measure the particle current in the channel as a function of the gravitational driving force, controlled by the tilt angle of the setup, for channels with zero, one, and two barriers. In the absence of barriers, the current shows a trivial linear dependence on the driving force, shown by the blue line in Fig. 1d. For a single barrier (green line in Fig. 1d), we observe a crossover from a zero-flow regime at small driving forces (where the driving force is too weak to push particles across the barrier) to an approximately linear regime for large driving forces [9]. Hence, the barrier provides a resistance to the flow, which reduces the particle current. Adding a second barrier to a channel results in a clear non-additivity of the resistance of the two barriers. In particular, for two barriers separated by approximately 2.5 times the typical interparticle distance (red line in Fig. 1), the second barrier has a much stronger effect on the total particle current than the first one, indicating a higher effective resistance.

To explore this non-additivity in detail, we make use of overdamped Brownian dynamics simulations and dynamical density functional theory (DDFT) calculations. We consider a two-dimensional system with periodic boundary conditions along the channel (x-direction), containing N particles interacting via a dipolar repulsion

$$\beta V_{\text{int}}(r) = \Gamma \left(\frac{a}{r}\right)^3, \tag{1}$$

where $\beta = 1/k_B T$ with k_B Boltzmann's constant and T the temperature, Γ is the dimensionless interaction strength, and $a = \rho_0^{-1/2}$ sets the length scale of a typical interparticle spacing of a given mean number density ρ_0. The particles additionally experience a constant driving force $F\hat{\mathbf{x}}$ pushing the particles along the channel.

The confining channel and barriers are modeled as an external potential $V_{\text{ext}}(x, y) = V_{\text{channel}}(y) + V_{\text{barrier}}(x)$. The first term here is a steep repulsive wall potential confining the particles in one direction. V_{barrier} represents one or two parabola-shaped potential barriers with width a and height $V_0 = 10\, k_{\text{B}}T$, see Fig. 2b inset and Supplemental Material [14]. We choose the channel width $L_y = 4.65a$, and the channel length L_x such that the total number density $\rho_0 = N/(L_x L_y) = 1/a^2$ for a given particle number N.

In our DDFT calculations [15, 16], we choose the Ramakrishnan–Yussouff functional [17] to model interacting particles in a fluid state ($\Gamma = 5$). In addition to DDFT, we perform Brownian Dynamics simulations of particles experiencing the same potentials and external driving force. As a reference we provide an analytical solution for non-interacting particles ($\Gamma = 0$). See Supplemental Material [14] for details.

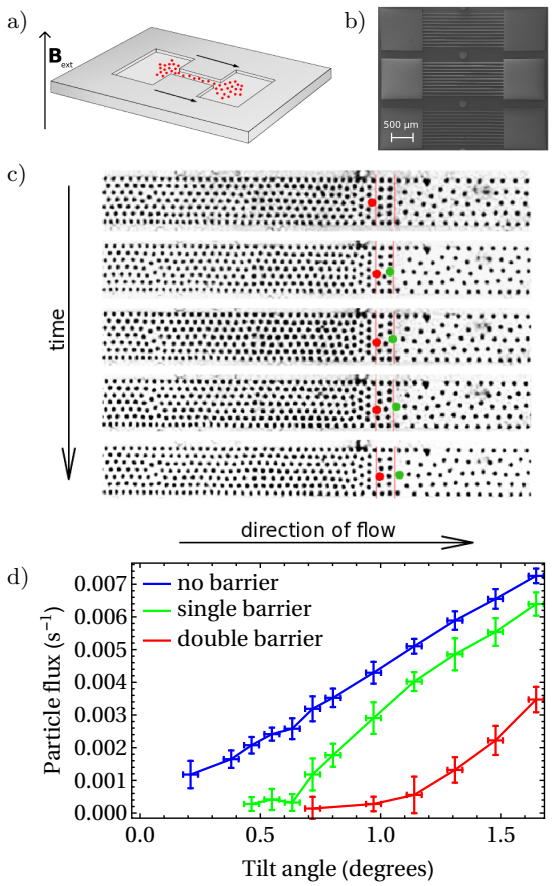

FIG. 1. a) Schematic setup of the experiment: two particle reservoirs are connected by a microfluidic channel through which particles are flowing due to gravity. b) Top view of the experimental system. c) Snapshots of a two barrier system for different times. The position of the barriers is indicated by a red vertical line. Two particles are highlighted in red and green. d) Flux as a function of tilt angle in a system with no barriers (blue line), single barrier (green line) and double barriers (red line). The initial density was $\rho_0 = (7.23 \pm 0.5) \times 10^{-3} \mu\text{m}^{-2}$, and the external field strength was 0.6 mT. The separation between the two barriers was 30μm.

Using both DDFT and simulations, we explore the relation between the total steady-state particle current J along the channel, the driving force F on the particles, and the distance Δx between the two barriers. The ratio of the driving force and current characterizes the total resistance of the system, $R^{\text{tot}} = \frac{F}{J}$. In a channel without barriers, the particles trivially adopt the average drift current $J_0 = F\rho_0 L_y \xi^{-1}$, where ξ is the friction coefficient of the background solvent, leading to an inherent background resistance $R_{\text{bg}} = \xi/(L_y \rho_0)$. In a single-barrier system, the resistance R_1 added by the barrier can be

extracted from the total resistance $R_s^{tot} = R_{bg} + R_1$ by measuring the single-barrier current J_s:

$$R_1 = R_s^{tot} - R_{bg} = F\left(\frac{1}{J_s} - \frac{1}{J_0}\right). \quad (2)$$

Similarly, in a double-barrier system (with current J_d), the total resistance is $R_d^{tot} = R_{bg} + R_1 + R_2$, and the effective resistance of the second barrier R_2 can be written as

$$R_2 = F\left(\frac{1}{J_d} - \frac{1}{J_s}\right). \quad (3)$$

In the case of additivity, the resistance R_2 of the second barrier will be equal to R_1 (the resistance of the first barrier), while deviations from this rule will indicate non-additivity.

In Fig. 2, we plot R_2/R_1 for a range of barrier separations Δx at different driving forces F, as obtained from analytical theory [14] (a), DDFT calculations (b), and computer simulations (c). For non-interacting particles R_2 is lowest when the two barriers are touching ($\Delta x = a$) and converges exponentially to R_1 for larger distances. In contrast, for interacting particles and for all investigated F, the resistance of the second barrier is highest at $\Delta x = a$. At this separation the resistance added by the second barrier can be many times higher than R_1, signaling strong non-additivity. More interestingly, for slightly larger separations ($\Delta x \simeq 1.5a$), R_2 becomes smaller than R_1, and even negative for sufficiently weak driving forces. In this regime, the addition of the second barrier *reduces* the overall resistance in the channel. At larger Δx, R_2 shows decaying oscillations, converging towards the additive case ($R_2 = R_1$), as expected at sufficiently large distances.

We can understand this observation by considering the interactions between the particles. Since these are dipolar in nature, they are sufficiently long-ranged to span across the barrier. Hence, a particle on top of the barrier experiences forces from particles between the two barriers, which depend on the density and structuring of those particles. In Fig. 3 we plot the density profile of the particles $\rho_x(x)$, projected onto the long axis of the channel, for various barrier separations Δx, as well as for a single barrier. In the single-barrier case, we always observe a high density peak in front of the barrier, and a slightly lower peak just after the barrier (see Fig. 3a). In the two-barrier cases, the additional peaks in between the two barriers vary in height based on Δx. For very small separations (Fig. 3b), where the resistance of the second barrier is high ($R_2 > R_1$), we find a single sharp density peak between the barriers, which is significantly higher than the peak observed after a single barrier. Here, particles between the barriers are arranged in a single line with little room for fluctuations, and hence provide a strong and relatively constant force on particles crossing

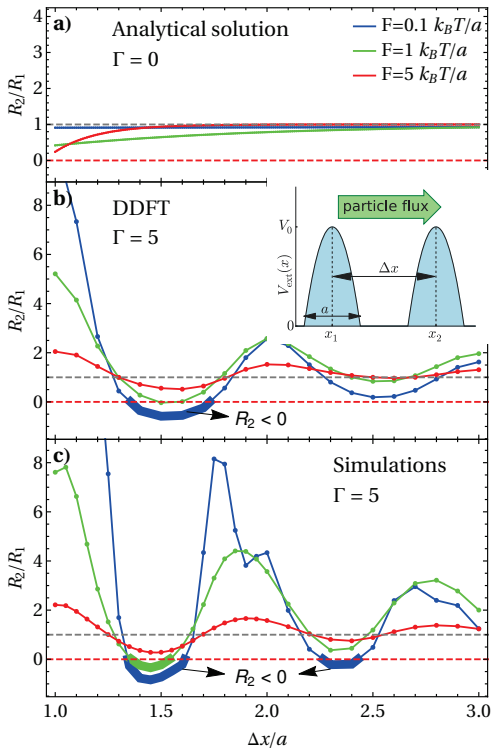

FIG. 2. (Color online) Effective resistance R_2 of the second barrier relative to the resistance R_1 of the first barrier, as a function of the barrier spacing Δx, at different driving forces. The dashed lines highlight special values of R_2: the gray line shows Ohmic additivity and the red line marks the onset of negative effective resistance. Results are shown for analytical theory [14] at $\Gamma = 0$ (a), DDFT at $\Gamma = 5$ (b), and simulations at $\Gamma = 5$ (c). A sketch of the barrier configuration is shown in inset b.

the first barrier, pushing them back. In the regime where $R_2 < R_1$ (Fig. 3c), we instead see two much lower peaks, indicating a structure with two layers and significantly larger fluctuations. These larger fluctuations not only provide space for particles entering via the first barrier, but also modulate the force exerted on particles crossing the barriers, resulting in a fluctuating effective barrier height. For weak driving forces, barrier crossings are rare events, whose rate depends exponentially on the barrier height. Fluctuations in barrier height are known to lead to significantly higher crossing rates [10, 11] and hence higher currents. Finally, for larger separations, where $R_2 > R_1$ again, we observe two higher peaks, indicating a more structured pair of layers between the barriers.

We confirm this intuitive picture by plotting in Fig. 4 the relative height of the first peak after the first barrier $\delta\rho^{peak} = \rho_d^{peak}/\rho_s^{peak}$, where ρ_s^{peak} is the height of the first peak after a single barrier, and ρ_d^{peak} is the height of the first peak after the first of two barriers. When plotted as a function of Δx, the peak height (blue in

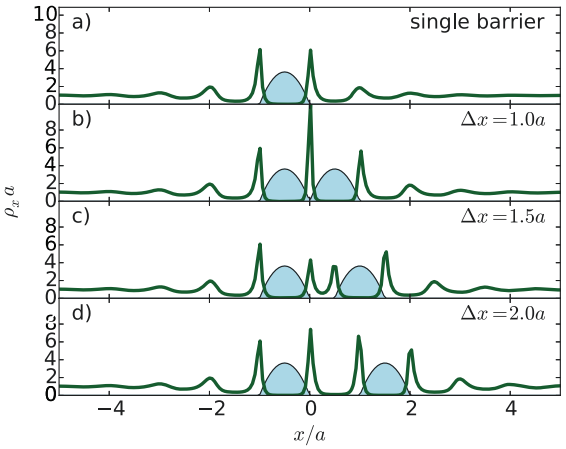

FIG. 3. Local density profiles as a function of distance along the channel at the same interaction strength ($\Gamma = 5$) and driving force $F = 0.1k_BT/a$, as obtained via DDFT. From top to bottom, we show a system with a single barrier, and systems with two barriers at separations $\Delta x/a = 1.0, 1.5$, and 2.0.

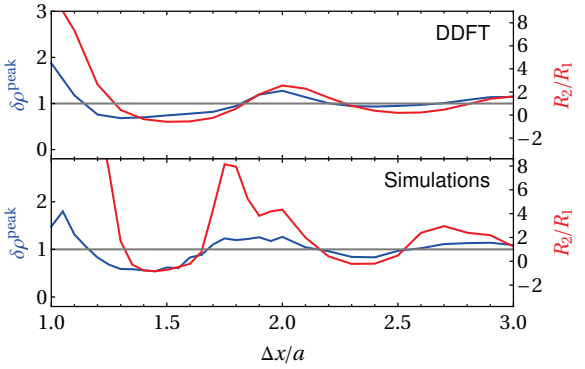

FIG. 4. Height of the first density peak after the first barrier (normalized by the height of the peak after a single barrier) as a function of barrier separation at fixed driving force $F = 0.1k_BT/a$ and interaction strength $\Gamma = 5$, as obtained from DDFT (top) and simulations (bottom).

Fig. 4) indeed strongly correlates with the particle current (red) in both the DDFT framework and the simulations. In our particle-resolved simulations, the additional fluctuations of the particles in between the two barriers are clearly visible. Moreover, examining simulation trajectories demonstrates that for most barrier separations, whenever a particle crosses the first barrier, the sudden increase in density between the barriers typically leads to the rapid expulsion of a particle over the second barrier. This observation confirms that the first of the two barriers can indeed be considered as the main bottleneck for the overall flow process. However, for $\Delta x \lesssim 1.3$, the bottleneck is instead the crossing of the *second* barrier. Here, particles form a single narrow layer between the two barriers, which inhibits the possibility of collectively pushing a particle across the second barrier. This may explain the reduced correlation between $\delta\rho_{\text{peak}}$ and R_2/R_1 for small Δx in Fig. 4.

In conclusion, we have explored the effect of sequential potential energy barriers on the flow of colloidal particles driven through microchannels. As our experiment shows, two barriers close together can result in drastically higher resistance than twice the resistance of a single barrier. Moreover, via a detailed investigation of this non-additivity using both simulations and dynamical density functional theory, we discover that depending on the barrier spacing, the second barrier can add an effective resistance that is higher than the resistance of a single barrier, lower, or even negative. In the negative regime, the presence of the second barrier helps particles cross the first barrier, contrary to what intuition would suggest. We show that this enhanced barrier-crossing rate can be attributed to the structuring of the layer of particles in between the two barriers: weaker structuring (evidenced by lower peaks in the density profile) increase the current. A vital component for this phenomenon is the requirement that particles on top of the barriers can still interact with the particles aggregated just before and after that barrier, necessitating sufficiently long-ranged interactions. Indeed, preliminary simulations show a clear reduction of the observed non-additivity when the barrier is wider in comparison to the interaction range. As a second requirement, the density should be high enough to enable significant ordering of particles. In the confined region between the barriers, the ordering will depend sensitively on the ratio of the barrier spacing Δx and the preferred spacing between neighboring layers of particles, as long as Δx is small compared to the correlation length in the system. Similar confinement effects have shown to result in oscillatory behavior in forces between plates or spheres immersed in a background of smaller particles [18]. Interestingly, the effect of negative resistance is reminiscent of the interplay between reflecting barriers in quantum-mechanical systems, where interference is known to lead to enhanced transmission for certain barrier spacings, as used in e.g. Fabry-Perot interferometers [19].

The sensitivity of the resistance to the barrier separation and microscopic particle interactions provide a method to tailor and control flow through channels [20–22] or porous media [23]. Interestingly, *geometric* obstacles have similarly been shown to enhance flow [24], as applied in e.g. the design of emergency exits [12, 25]. However, in these cases, enhanced flow rate is typically observed when the added obstacle is placed *before* the bottleneck, rather than behind it.

The possibility of mitigating a flow-resisting barrier by placing another barrier behind it might have important implications in microfluidic devices. Moreover, the specificity of this approach to relatively long-ranged interac-

tions suggests an opportunity for separating different particle species, or enhanced flow control via external fields modifying the interactions. Further applications include the directed transport of strongly charged dust particles in a plasma [26] and congestions in granulates [27], as well as jammed flow situations of colloids [28], or agents through constrictions [29]. In particular, a jammed situation near an obstacle may be avoided by adding further obstacles. An interesting question for future research is whether the effective total resistance could be further tuned by using a combination of three, four, or an infinite number of obstacles [30] (forming e.g. a ratchet [31, 32]), or by using barriers of differing heights.

We gratefully acknowledge funding from the German Research Foundation (DFG) within project LO 418/19-1. We thank Arjun Yodh, Laura Filion, and Marco Heinen for helpful discussions.

* urs.zimmermann@uni-duesseldorf.de

[1] T. M. Squires and S. R. Quake, Rev. Mod. Phys. **77**, 977 (2005).
[2] P. Hänggi, P. Talkner, and M. Borkovec, Rev. Mod. Phys. **62**, 251 (1990).
[3] D. Helbing, Rev. Mod. Phys. **73**, 1067 (2001).
[4] D. J. T. Sumpter, Phil. Trans. R. Soc. B **361**, 5 (2006).
[5] M. B. Wan, C. J. Olson Reichhardt, Z. Nussinov, and C. Reichhardt, Phys. Rev. Lett. **101**, 018102 (2008).
[6] H. H. Wensink, J. Dunkel, S. Heidenreich, K. Drescher, R. E. Goldstein, H. Löwen, and J. M. Yeomans, Proc. Natl. Acad. Sci. USA **109**, 14308 (2012).
[7] H. H. Wensink and H. Löwen, Phys. Rev. E **78**, 031409 (2008).
[8] J. Dzubiella and J.-P. Hansen, J. Chem. Phys. **122**, 234706 (2005).
[9] C. Kreuter, U. Siems, P. Henseler, P. Nielaba, P. Leiderer, and A. Erbe, J. Phys.: Condens. Matter **24**, 464120 (2012).
[10] D. L. Stein, R. G. Palmer, J. L. Van Hemmen, and C. R. Doering, Phys. Lett. A **136**, 353 (1989).
[11] P. Pechukas and P. Hänggi, Phys. Rev. Lett. **73**, 2772 (1994).
[12] N. Shiwakoti and M. Sarvi, Transp. Res. Part C: Emerg. Technol. **37**, 260 (2013).
[13] J. R. Anderson, D. T. Chiu, H. Wu, O. J. Schueller, and G. M. Whitesides, Electrophoresis **21**, 27 (2000).
[14] See Supplemental Material at xxx for additional details on the experimental setup, model, DDFT calculations, analytic theory, and simulations.
[15] U. M. B. Marconi and P. Tarazona, J. Chem. Phys. **110**, 8032 (1999).
[16] A. J. Archer and R. Evans, J. Chem. Phys. **121**, 4246 (2004).
[17] T. V. Ramakrishnan and M. Yussouff, Phys. Rev. B **19**, 2775 (1979).
[18] R. Roth, R. Evans, and S. Dietrich, Phys. Rev. E **62**, 5360 (2000).
[19] M. Vaughan, *The Fabry-Perot Interferometer: History, Theory, Practice and Applications*, *Series in Optics and Optoelectronics* (Taylor & Francis, New York (USA), 1989).
[20] B. Lindner and L. Schimansky-Geier, Phys. Rev. Lett. **89**, 230602 (2002).
[21] R. Gernert and S. H. L. Klapp, Phys. Rev. E **92**, 022132 (2015).
[22] M. F. Carusela and J. M. Rub, J. Chem. Phys. **146**, 184901 (2017).
[23] M. Spanner, F. Höfling, S. C. Kapfer, K. R. Mecke, G. E. Schröder-Turk, and T. Franosch, Phys. Rev. Lett. **116**, 060601 (2016).
[24] F. Alonso-Marroquin, S. I. Azeezullah, S. A. Galindo-Torres, and L. M. Olsen-Kettle, Phys. Rev. E **85**, 020301 (2012).
[25] J. Tanimoto, A. Hagishima, and Y. Tanaka, Physica A **389**, 5611 (2010).
[26] G. E. Morfill and A. V. Ivlev, Rev. Mod. Phys. **81**, 1353 (2009).
[27] I. Zuriguel, A. Garcimartín, D. Maza, L. A. Pugnaloni, and J. M. Pastor, Phys. Rev. E **71**, 051303 (2005).
[28] P. Kanehl and H. Stark, Phys. Rev. Lett. **119**, 018002 (2017).
[29] A. J. Liu and S. R. Nagel, Nature **396**, 21 (1998).
[30] U. Siems and P. Nielaba, Phys. Rev. E **91**, 022313 (2015).
[31] P. Hänggi, F. Marchesoni, and F. Nori, Ann. Phys. **14**, 51 (2005).
[32] M. Evstigneev, S. von Gehlen, and P. Reimann, Phys. Rev. E **79**, 011116 (2009).

Negative resistance for colloids driven over two barriers in a microchannel. Supplementary Information

Urs Zimmermann,[1,*] Hartmut Löwen,[1] Christian Kreuter,[2] Artur Erbe,[3] Paul Leiderer,[2] and Frank Smallenburg[1]

[1] *Institut für Theoretische Physik II: Weiche Materie, Heinrich-Heine-Universität Düsseldorf, D-40225 Düsseldorf, Germany*

[2] *Fachbereich Physik, Universität Konstanz, D-78457 Konstanz, Germany*

[3] *Institut für Ionenstrahlphysik und Materialforschung, Helmholtz-Zentrum Dresden-Rossendorf, D-01328 Dresden, Germany*

(Dated: September 21, 2017)

EXPERIMENTAL SETUP

Our experiments are based on repulsive microscopic particles, gravitationally driven through microchannels. We use superparamagnetic colloidal particles (Dynal M-450, diameter $\sigma = 4.50(5)$ μm, $\rho_m = 1500\,\mathrm{kg\,m^3}$) which are restricted to two-dimensional in-plane motion due to gravity. The cell consists of two rectangular reservoirs of side length 1 mm which are connected by multiple channels. The dimensions of each channel is 2 mm in length, 30 μm in width and 8 μm in height. In the channels, U–shaped step-like barrier structures are implemented along the channel, each of them with width 3 μm and height 500 nm near the channel walls and 250 nm in the middle of the channel.

The applied magnetic field $\mathbf{B}_{\mathrm{ext}}$ induces a dipole-dipole repulsion among the colloidal particles, and the strength of the dipole-dipole interaction can be tuned by changing the magnitude of the magnetic field. The repulsive in-plane interaction potential $V(r)$ is [1, 2]

$$V(r) = \begin{cases} \frac{\mu_0(\chi_{\mathrm{eff}}\mathbf{B}_{\mathrm{ext}})^2}{4\pi r^3}, & \text{for } r \geq \sigma, \\ \infty, & \text{for } r < \sigma, \end{cases} \tag{1}$$

where μ_0 is the vacuum permeability and $\chi_{\mathrm{eff}} = 7.88(8) \cdot 10^{-11}\mathrm{Am^2T^{-1}}$ is the effective magnetic susceptibility of the particles. Note that for sufficiently high field strengths, the particles never touch, such that the hard-core component of the interaction potential can be neglected.

By tilting the whole experimental setup, gravity acts as an external driving force, with a strength controlled by the tilt angle and the buoyancy-corrected effective mass of the particles ($m^* = 2.385(80) \cdot 10^{-14}$ kg). Using video microscopy, we measure the total particle flux through channels with zero, one, or two barriers as a function of the strength of the driving force.

MODEL

The external potential $V_{\mathrm{ext}}(x, y)$ is composed of a confining channel contribution, $V_{\mathrm{channel}}(y)$, and the barrier potential, $V_{\mathrm{barrier}}(x)$.

The steep repulsive potential forming the channel walls is given by

$$V_{\mathrm{channel}}(y) = V_c \left[1 - \frac{1}{2}\,\mathrm{erf}\left(\frac{y + \frac{L_y}{2}}{\sqrt{2}w} \right) + \frac{1}{2}\,\mathrm{erf}\left(\frac{y - \frac{L_y}{2}}{\sqrt{2}w} \right) \right], \tag{2}$$

with channel width L_y and maximum channel potential height $V_c = 1000 k_B T$. The parameter $w = 0.25a$ sets the softness of the walls. We choose $L_y = 4.65a$. The channel length $L_x = 25.79a$ is fixed by the imposed number of particles $N = 120$.

A single barrier potential is given by

$$V_{\mathrm{barrier}}(x) = \begin{cases} V_0 \left[1 - \left(\frac{x - x_1}{a/2} \right)^2 \right], & \text{for } |x - x_1| < a/2 \\ 0, & \text{otherwise} \end{cases}, \tag{3}$$

where x_1 is the position of the barrier. The double barrier potential is simply the superposition of two non-overlapping single barrier potentials at x_1 and x_2, where $|x_1 - x_2| = \Delta x \geq a$.

DYNAMICAL DENSITY FUNCTIONAL THEORY

Within the DDFT framework [3, 4], the number density field $\rho(\mathbf{r}, t)$ of the colloidal particles is calculated by solving the differential equation

$$\frac{\partial \rho(\mathbf{r}, t)}{\partial t} = D\nabla \left(\rho(\mathbf{r}, t) \nabla \frac{\delta \mathcal{F}[\rho(\mathbf{r}, t)]}{\delta \rho(\mathbf{r}, t)} \right), \tag{4}$$

where $D = k_{\mathrm{B}}T/\xi$ is the single particle diffusion constant, ξ the friction coefficient and $\mathcal{F}[\rho] = \mathcal{F}_{\mathrm{id}}[\rho] + \mathcal{F}_{\mathrm{ext}}[\rho] + \mathcal{F}_{\mathrm{exc}}[\rho]$ is the total Helmholtz free energy functional. This functional incorporates the ideal gas contribution

$$\mathcal{F}_{\mathrm{id}}[\rho] = k_{\mathrm{B}}T \int \mathrm{d}\mathbf{r}\; \rho(\mathbf{r}) \big(\log(\Lambda^2 \rho(\mathbf{r})) - 1 \big) \tag{5}$$

and the external potential term

$$\mathcal{F}_{\mathrm{ext}}[\rho] = \int \mathrm{d}\mathbf{r}\; \rho(\mathbf{r}) \big(V_{\mathrm{ext}}(\mathbf{r}) - xF \big), \tag{6}$$

where Λ is the thermal de Broglie wavelength. As an approximation for the excess free energy functional $\mathcal{F}_{\rm exc}[\rho]$ we chose the Ramakrishnan–Yussouff functional [5]

$$\mathcal{F}_{\rm exc}[\rho] = \mathcal{F}^{\rm ref}_{\rm exc}(\rho_0) - \frac{k_{\rm B}T}{2}\int{\rm d}\mathbf{r}\int{\rm d}\mathbf{r}'\,\Delta\rho(\mathbf{r})\Delta\rho(\mathbf{r}')c_0^{(2)}(|\mathbf{r}-\mathbf{r}'|;\rho_0,\Gamma). \quad (7)$$

Here, $\mathcal{F}^{\rm ref}_{\rm exc}(\rho_0)$ is the excess free energy of an isotropic and homogeneous reference fluid at density ρ_0, $\Delta\rho(\mathbf{r}) = \rho(\mathbf{r}) - \rho_0$ describes the density difference to the reference density, and $c_0^{(2)}(r;\rho_0,\Gamma)$ is a pair (two-point) direct correlation function[6] that has been calculated via liquid integral theory with Rogers-Young closure [7].

The DDFT is solved numerically by using finite volume difference methods [8]. In each run, we first compute the equilibrium configuration of the system at a given barrier configuration in absence of a driving force ($F = 0$). Then, we switch on the driving force and let the system evolve towards its steady state.

ANALYTICAL THEORY

For non-interacting particles the excess free energy vanishes, i.e. $\mathcal{F}_{\rm exc} \equiv 0$, and the DDFT in the steady state can be reduced to a single variable x. The general solution for periodic boundary conditions and tilted potential $V(x) = V_{\rm barrier}(x) - Fx$ is [9]

$$J = \frac{D\rho_0 L_x L_y(1-e^{-\beta F L_x})}{I_+ I_- - (1-e^{-\beta F L_x})\int_0^{L_x}{\rm d}x\; e^{-\beta V(x)}\int_0^x {\rm d}x'\; e^{-\beta V(x')}}, \quad (8)$$

with $I_\pm = \int_0^{L_x}{\rm d}x\; e^{\pm\beta V(x)}$.

For single and double barrier potentials we can find an analytic expression for J and therefore express the ratio of resistances as

$$\frac{R_2}{R_1} = 1 - K\left(e^{-F(\Delta x - a)} + e^{-F(L_x - \Delta x - a)}\right). \quad (9)$$

Here, the value $K = \frac{P}{Q}$ does not dependent on Δx and is determined by the expressions

$$P = \beta^2F^2(A_1(1-e^{-\beta F a}) - A_2) - (1-e^{-\beta F a})^2, \quad (10)$$

$$Q = \beta^2F^2(A_1(1-e^{-\beta F(L_x-a)}) + A_3 - A_4) - \beta F a(1-e^{-\beta F L_x}) - (1-e^{-\beta F(L_x-a)})(1-e^{-\beta F a}), \quad (11)$$

with

$$\gamma = \frac{a}{4}\sqrt{\frac{\pi}{\beta V_0}}, \quad (12)$$

$$\zeta_\pm = \sqrt{\beta V_0}\left(\frac{Fa}{4\beta V_0} \pm 1\right), \quad (13)$$

$$\Delta E = {\rm erf}(\zeta_+) - {\rm erf}(\zeta_-), \quad (14)$$

$$\Delta I = {\rm erfi}(\zeta_+) - {\rm erfi}(\zeta_-), \quad (15)$$

$$A_1 = \gamma\left(e^{-\zeta_+^2}\Delta I + e^{\zeta_-^2}\Delta E\right), \quad (16)$$

$$A_2 = \gamma^2 e^{-\beta F a}\Delta E\Delta I, \quad (17)$$

$$A_3 = \gamma^2\Delta I\left({\rm erf}(\zeta_+) - {\rm erf}(\zeta_-)e^{-\beta F L_x}\right), \quad (18)$$

$$A_4 = \frac{a^2(1-e^{-\beta F L_x})}{8\beta V_0}\left(\zeta_+^2\Phi(\zeta_+^2) - \zeta_-^2\Phi(\zeta_-^2)\right), \quad (19)$$

where ${\rm erfi}(x)$ is the imaginary error function, and $\Phi(x) = {}_2F_2\left(1,1;\frac{3}{2},2;x\right)$ is the generalized hypergeometric function.

BROWNIAN DYNAMICS SIMULATIONS

In addition to DDFT, we perform overdamped Brownian Dynamics simulations of particles. Here, we numerically solve the equations of motion for the particles, given by

$$\dot{\mathbf{r}}_i = \frac{-\nabla_i V_{\rm tot}}{\xi} + \frac{F\hat{\mathbf{x}}}{\xi} + \sqrt{2D}\mathbf{R}(t), \quad (20)$$

where $\mathbf{r}_i$ is the position of particle i, and $V_{\rm tot}$ is the total potential energy of the system, including particle-particle, particle-wall, and particle-barrier interactions. Finally, $\mathbf{R}(t)$ is a delta-correlated random variable with zero mean and unit variance. The dipolar interactions were truncated and shifted at a distance of $5a$.

Most simulations were performed using $N = 120$ particles, in a channel with periodic boundary conditions along the x-axis. We have confirmed that our results are qualitatively the same for larger systems of $N = 600$ particles.

* urs.zimmermann@uni-duesseldorf.de

[1] K. Zahn, J. M. Méndez-Alcaraz, and G. Maret, Phys. Rev. Lett. **79**, 175 (1997).
[2] C. Kreuter, U. Siems, P. Henseler, P. Nielaba, P. Leiderer, and A. Erbe, J. Phys.: Condens. Matter **24**, 464120 (2012).
[3] U. M. B. Marconi and P. Tarazona, J. Chem. Phys. **110**, 8032 (1999).
[4] A. J. Archer and R. Evans, J. Chem. Phys. **121**, 4246 (2004).
[5] T. V. Ramakrishnan and M. Yussouff, Phys. Rev. B **19**, 2775 (1979).

[6] J.-P. Hansen and I. R. McDonald, *Theory of Simple Liquids: with Applications to Soft Matter*, 4 ed. (Elsevier Academic Press, Oxford, 2009).
[7] S. van Teeffelen, R. Backofen, A. Voigt, and H. Löwen, Phys. Rev. E **79**, 051404 (2009).
[8] J. E. Guyer, D. Wheeler, and J. A. Warren, Computing in Science & Engineering **11**, 6 (2009).
[9] H. Risken, *The Fokker-Planck Equation: Methods of Solution and Applications*, Vol. 18 of *Springer Series in Synergetics*, 3 ed. (Springer-Verlag, Berlin, 1996), p. 289.

Literaturverzeichnis

[1] I. W. Hamley. *Introduction to Soft Matter*. John Wiley & Sons, Chichester, revised edition (2007).

[2] M. Kleman and O. D. Laverntovich. *Soft matter physics: an introduction*. Springer Science & Business Media (2007).

[3] R. A. Jones. *Soft condensed matter*, volume 6. Oxford University Press (2002).

[4] P.-G. de Gennes. Soft matter: more than words. *Soft Matter* **1**, 16–16 (2005).

[5] M. Daoud and C. E. Williams, editors. *Soft Matter Physics*. Springer-Verlag Berlin Heidelberg (1999).

[6] D. G. Dervichian. The Control of Lyotropic Liquid-Crystals, Biological and Medical Implications. *Molecular Crystals and Liquid Crystals* **40**, 19–31 (1977).

[7] P.-G. de Gennes. Nobel Lecture: Soft Matter (1991). URL `http://www.nobelprize.org/nobel_prizes/physics/laureates/1991/gennes-lecture.htm`.

[8] A. Miriyev, K. Stack, and H. Lipson. Soft material for soft actuators. *Nature Communications* **8** (2017).

[9] M. M. Schmauch, S. R. Mishra, B. A. Evans, O. D. Velev, and J. B. Tracy. Chained Iron Microparticles for Directionally Controlled Actuation of Soft Robots. *ACS Applied Materials & Interfaces* **9**, 11895–11901 (2017).

[10] J. A. Rogers. A clear advance in soft actuators. *Science* **341**, 968–969 (2013).

[11] D. A. LaVan, T. McGuire, and R. Langer. Small-scale systems for in vivo drug delivery. *Nature Biotechnology* **21**, 1184–1191 (2003).

[12] W. Gao and J. Wang. Synthetic micro/nanomotors in drug delivery. *Nanoscale* **6**, 10486–10494 (2014).

[13] W. Gao, R. Dong, S. Thamphiwatana, J. Li, W. Gao, L. Zhang, and J. Wang. Artificial Micromotors in the Mouse's Stomach: A Step toward in Vivo Use of Synthetic Motors. *ACS Nano* **9**, 117–123 (2015).

[14] R. P. Feynman. There's Plenty of Room at the Bottom (1959). URL `http://www.its.caltech.edu/~feynman/plenty.html`.

[15] D. Fennell Evans, H. Wennerstrom, and R. Rajagopalan. The colloidal domain: where physics, chemistry, biology, and technology meet. *Journal of Colloid and Interface Science* **172**, 541–541 (1995).

[16] J. K. G. Dhont. *An Introduction to Dynamics of Colloids*. Elsevier, Amsterdam, 2 edition (2003).

[17] M. Doi and S. Edwards. *The Theory of Polymer Dynamics*, volume 73 of *International Series of Monographs on Physics*. Oxford University Press, Oxford, 1 edition (1986).

[18] G. R. Strobl and G. R. Strobl. *The physics of polymers*, volume 2. Springer (1997).

[19] P. J. Collings and M. Hird. *Introduction to liquid crystals: chemistry and physics*. CRC Press (2017).

[20] G. Filipcsei, I. Csetneki, A. Szilágyi, and M. Zrínyi. Magnetic field-responsive smart polymer composites. In: *Oligomers-Polymer Composites-Molecular Imprinting*, pages 137–189. Springer (2007).

[21] J. R. Van der Maarel. *Introduction to biopolymer physics*. World Scientific (2008).

[22] A. Ivlev, H. Löwen, G. Morfill, and C. Royall. *Complex Plasmas and Colloidal Dispersions: Particle-Resolved Studies of Classical Liquids and Solids*, volume 5 of *Series in Soft Condensed Matter*. World Scientific Publishing, Singapore, 1 edition (2012).

[23] Nobelprize.org. Pierre-Gilles de Gennes - Facts (1991). URL `http://www.nobelprize.org/nobel_prizes/physics/laureates/1991/gennes-facts.html`.

[24] J.-L. Barrat and J.-P. Hansen. *Basic Concepts for Simple and Complex Liquids*. Cambridge University Press, Cambridge, 1 edition (2003).

[25] H. Löwen. Colloidal soft matter under external control. *Journal of Physics: Condensed Matter* **13**, R415–R432 (2001).

[26] W. B. Russel, D. A. Saville, and W. R. Schowalter. *Colloidal dispersions*. Cambridge university press (1989).

[27] R. J. Hunter. *Foundations of colloid science*. Oxford University Press (2001).

[28] D. Frenkel. Introduction to colloidal systems. In: M. R. Evans and M. E. Cates, editors, *Soft and Fragile Matter*, Scottish Graduate Series, pages 113–144. Taylor & Francis (2000).

[29] W. Poon. Colloids as big atoms. *Science* **304**, 830–831 (2004).

[30] T. Riste and D. Sherrington. *Phase transitions in soft condensed matter*, volume 211. Springer Science & Business Media (2012).

[31] A. Denton and H. Löwen. Stability of colloidal quasicrystals. *Physical Review Letters* **81**, 469 (1998).

[32] S. Fischer, A. Exner, K. Zielske, J. Perlich, S. Deloudi, W. Steurer, P. Lindner, and S. Förster. Colloidal quasicrystals with 12-fold and 18-fold diffraction symmetry. *Proceedings of the National Academy of Sciences* **108**, 1810–1814 (2011).

[33] E. R. Weeks. Microscopy of soft materials. In: J. Olafsen, editor, *Experimental and Computational Techniques in Soft Condensed Matter Physics*, page 1–24. Cambridge University Press (2010).

[34] M. Minsky. Memoir on inventing the confocal scanning microscope. *Scanning* **10**, 128–138 (1988).

[35] V. Prasad, D. Semwogerere, and E. R. Weeks. Confocal microscopy of colloids. *Journal of Physics: Condensed Matter* **19**, 113102 (2007).

[36] B. J. Berne and R. Pecora. *Dynamic light scattering: with applications to chemistry, biology, and physics*. Courier Corporation (2000).

[37] R. Klein and G. Nägele. Static and dynamic scattering by concentrated systems: theory. *Current Opinion in Colloid & Interface Science* **1**, 4–10 (2010).

[38] J. K. Dhont, C. Smits, and H. N. Lekkerkerker. A time resolved static light scattering study on nucleation and crystallization in a colloidal system. *Journal of Colloid and Interface Science* **152**, 386–401 (1992).

[39] J. C. Crocker and D. G. Grier. Methods of digital video microscopy for colloidal studies. *Journal of Colloid and Interface Science* **179**, 298–310 (1996).

[40] R. Besseling, L. Isa, E. R. Weeks, and W. C. Poon. Quantitative imaging of colloidal flows. *Advances in Colloid and Interface Science* **146**, 1–17 (2009).

[41] V. N. Manoharan. Colloidal matter: Packing, geometry, and entropy. *Science* **349**, 1253751–1253751 (2015).

[42] A. Yethiraj. Tunable colloids: control of colloidal phase transitions with tunable interactions. *Soft Matter* **3**, 1099–1115 (2007).

[43] D. M. Herlach, I. Klassen, P. Wette, and D. Holland-Moritz. Colloids as model systems for metals and alloys: a case study of crystallization. *Journal of Physics: Condensed Matter* **22**, 153101 (2010).

[44] H. Löwen. Introduction to colloidal dispersions in external fields. *European Physical Journal Special Topics* **222**, 2727–2737 (2013).

[45] T. Palberg. Crystallization kinetics of repulsive colloidal spheres. *Journal of Physics: Condensed Matter* **11**, R323–R360 (1999).

[46] V. J. Anderson and H. N. Lekkerkerker. Insights into phase transition kinetics from colloid science. *Nature* **416**, 811–815 (2002).

[47] W. C. K. Poon. A day in the life of a hard-sphere suspension. In: M. R. Evans and M. E. Cates, editors, *Soft and Fragile Matter*, Scottish Graduate Series, pages 1–8. Taylor & Francis (2000).

[48] A. Yethiraj and A. van Blaaderen. A colloidal model system with an interaction tunable from hard sphere to soft and dipolar. *Nature* **421**, 513–517 (2003).

[49] J. T. G. Overbeek. Monodisperse colloidal systems, fascinating and useful. *Advances in Colloid and Interface Science* **15**, 251–277 (1982).

[50] E. Matijevic. Preparation and properties of uniform size colloids. *Chemistry of Materials* **5**, 412–426 (1993).

[51] E. Pelizzetti. *Fine particles science and technology: from micro to nanoparticles*, volume 12. Springer Science & Business Media (2012).

[52] Y. Xia and G. M. Whitesides. Soft lithography. *Annual Review of Materials Science* **28**, 153–184 (1998).

[53] S. Y. Chou, P. R. Krauss, and P. J. Renstrom. Imprint lithography with 25-nanometer resolution. *Science* **272**, 85 (1996).

[54] A. Ashkin. Acceleration and trapping of particles by radiation pressure. *Physical Review Letters* **24**, 156 (1970).

[55] F. Evers, R. Hanes, C. Zunke, R. Capellmann, J. Bewerunge, C. Dalle-Ferrier, M. Jenkins, I. Ladadwa, A. Heuer, R. Castañeda-Priego, and S. Egelhaaf. Colloids in light fields: particle dynamics in random and periodic energy landscapes. *European Physical Journal Special Topics* **222**, 2995–3009 (2013).

[56] A. Ashkin, J. M. Dziedzic, J. Bjorkholm, and S. Chu. Observation of a single-beam gradient force optical trap for dielectric particles. *Optics Letters* **11**, 288–290 (1986).

[57] D. G. Grier. A revolution in optical manipulation. *Nature* **424**, 810–816 (2003).

[58] M. Allen and D. Tildesley. *Computer Simulation of Liquids*. Oxford University Press, Oxford, 1 edition (1987).

[59] H. Löwen. Applications of density functional theory in soft condensed matter. In: *Understanding Soft Condensed Matter Via Modeling And Computation*, pages 9–45. World Scientific (2011).

[60] T. G. Van de Ven. *Colloidal hydrodynamics*. Academic press (1989).

[61] J. Ingen-Housz. Bemerkungen über den Gebrauch des Vergrößerungsglases. Number 2 in Vermischte Schriften physisch-medicinischen Inhalts: Mit Kupfertafeln, pages 123–126. Wappler, Wien (1734).

[62] R. Brown. XXVII. A brief account of microscopical observations made in the months of June, July and August 1827, on the particles contained in the pollen of plants; and on the general existence of active molecules in organic and inorganic bodies. *The Philosophical Magazine* **4**, 161–173 (1828).

[63] A. Einstein. Über die von der molekularkinetischen Theorie der Wärme geforderte Bewegung von in ruhenden Flüssigkeiten suspendierten Teilchen. *Annalen der Physik* **322**, 549–560 (1905).

[64] M. von Smoluchowski. Zur kinetischen Theorie der Brownschen Molekularbewegung und der Suspensionen. *Annalen der Physik* **326**, 756–780 (1906).

[65] J. Perrin. Mouvement brownien et réalité moléculaire. *Annales de Chimie et de Physique* **18**, 5–114 (1909).

[66] Nobelprize.org. Jean Baptiste Perrin - Facts (1926). URL `http://www.nobelprize.org/nobel_prizes/physics/laureates/1926/perrin-facts.html`.

[67] H. Risken. *The Fokker-Planck Equation: Methods of Solution and Applications*, volume 18 of *Springer Series in Synergetics*. Springer-Verlag, Berlin, 3 edition (1996).

[68] V. A. Parsegian. *Van der Waals forces: a handbook for biologists, chemists, engineers, and physicists*. Cambridge University Press (2005).

[69] R. Tadmor. The London-van der Waals interaction energy between objects of various geometries. *Journal of Physics: Condensed Matter* **13**, L195 (2001).

[70] Z. Zhang and S. Glotzer. Self-assembly of patchy particles. *Nano Letters* **4**, 1407–1413 (2004).

[71] A. B. Pawar and I. Kretzschmar. Fabrication, assembly, and application of patchy particles. *Macromolecular Rapid Communications* **31**, 150–168 (2010).

[72] Y. Wang, Y. Wang, D. R. Breed, V. N. Manoharan, L. Feng, A. D. Hollingsworth, M. Weck, and D. J. Pine. Colloids with valence and specific directional bonding. *Nature* **491**, 51–55 (2012).

[73] W. C. Poon, E. R. Weeks, and C. P. Royall. On measuring colloidal volume fractions. *Soft Matter* **8**, 21–30 (2012).

[74] C. P. Royall, W. C. Poon, and E. R. Weeks. In search of colloidal hard spheres. *Soft Matter* **9**, 17–27 (2013).

[75] P. Pusey, E. Zaccarelli, C. Valeriani, E. Sanz, W. C. Poon, and M. E. Cates. Hard spheres: crystallization and glass formation. *Philosophical Transactions of the Royal Society of London A: Mathematical, Physical and Engineering Sciences* **367**, 4993–5011 (2009).

[76] M. N. Rosenbluth and A. W. Rosenbluth. Further results on Monte Carlo equations of state. *Journal of Chemical Physics* **22**, 881–884 (1954).

[77] W. W. Wood and J. Jacobson. Preliminary results from a recalculation of the Monte Carlo equation of state of hard spheres. *Journal of Chemical Physics* **27**, 1207–1208 (1957).

[78] B. Alder and T. Wainwright. Phase transition for a hard sphere system. *Journal of Chemical Physics* **27**, 1208–1209 (1957).

[79] P. Pusey and W. van Megen. Phase Behavior of Concentrated Suspensions of Nearly Hard Colloidal Spheres. *Nature* **320**, 340–342 (1986).

[80] M. Dijkstra. Entropy-driven phase transitions in colloids: from spheres to anisotropic particles. *Advances in Chemical Physics* **156**, 35 (2014).

[81] W. Van Megen and S. Underwood. Glass transition in colloidal hard spheres: Measurement and mode-coupling-theory analysis of the coherent intermediate scattering function. *Physical Review E* **49**, 4206 (1994).

[82] B. Doliwa and A. Heuer. Cage effect, local anisotropies, and dynamic heterogeneities at the glass transition: A computer study of hard spheres. *Physical Review Letters* **80**, 4915 (1998).

[83] A. Haji-Akbari, M. Engel, A. Keys, X. Zheng, R. Petschek, P. Palffy-Muhoray, and S. Glotzer. Disordered, quasicrystalline and crystalline phases of densely packed tetrahedra. *Nature* **462**, 773–777 (2009).

[84] P. F. Damasceno, M. Engel, and S. C. Glotzer. Predictive self-assembly of polyhedra into complex structures. *Science* **337**, 453–457 (2012).

[85] H. H. Wensink, H. Löwen, M. Marechal, A. Härtel, R. Wittkowski, U. Zimmermann, A. Kaiser, and A. M. Menzel. Differently shaped hard body colloids in confinement: from passive to active particles. *European Physical Journal Special Topics* **222**, 3023–3037 (2013).

[86] A. Härtel and H. Löwen. Fundamental measure density functional theory for hard spherocylinders in static and time-dependent aligning fields. *Journal of Physics: Condensed Matter* **22**, 104112 (2010).

[87] H. Hansen-Goos and K. Mecke. Tensorial density functional theory for non-spherical hard-body fluids. *Journal of Physics: Condensed Matter* **22**, 364107 (2010).

[88] J. A. Cuesta and Y. Martınez-Ratón. Fundamental measure theory for mixtures of parallel hard cubes. I. General formalism. *Journal of Chemical Physics* **107**, 6379–6389 (1997).

[89] Y. Martınez-Ratón and J. A. Cuesta. Fundamental measure theory for mixtures of parallel hard cubes. II. Phase behavior of the one-component fluid and of the binary mixture. *Journal of Chemical Physics* **111**, 317–327 (1999).

[90] E. Jagla. Melting of hard cubes. *Physical Review E* **58**, 4701 (1998).

[91] M. Marechal and M. Dijkstra. Phase behavior and structure of colloidal bowl-shaped particles: simulations. *Physical Review E* **82**, 31405 (2010).

[92] M. Marechal, H. H. Goetzke, A. Härtel, and H. Löwen. Inhomogeneous fluids of colloidal hard dumbbells: Fundamental measure theory and Monte Carlo simulations. *Journal of Chemical Physics* **135**, 234510 (2011).

[93] M. Marechal, U. Zimmermann, and H. Löwen. Freezing of parallel hard cubes with rounded edges. *Journal of Chemical Physics* **136**, 144506 (2012).

[94] K. Zahn, J. M. Méndez-Alcaraz, and G. Maret. Hydrodynamic interactions may enhance the self-diffusion of colloidal particles. *Physical Review Letters* **79**, 175 (1997).

[95] K. Zahn, R. Lenke, and G. Maret. Two-stage melting of paramagnetic colloidal crystals in two dimensions. *Physical Review Letters* **82**, 2721 (1999).

[96] J. D. Jackson. *Classical electrodynamics*. John Wiley & Sons (2007).

[97] J. Zhao, P. Papadopoulos, M. Roth, C. Dobbrow, E. Roeben, A. Schmidt, H.-J. Butt, G. Auernhammer, and D. Vollmer. Colloids in external electric and magnetic fields: colloidal crystals, pinning, chain formation, and electrokinetics. *European Physical Journal Special Topics* **222**, 2881–2893 (2013).

[98] J.-P. Hansen and I. McDonald. *Theory of Simple Liquids: with Applications to Soft Matter*. Elsevier Academic Press, Oxford, 4 edition (2009).

[99] F. Reif. *Fundamentals of statistical and thermal physics*. Waveland Press (2009).

[100] A. M. Menzel. Tuned, driven, and active soft matter. *Physics Reports* **554**, 1–45 (2015).

[101] S. Ramaswamy. The mechanics and statistics of active matter. *Annual Review of Condensed Matter Physics* **1**, 323–345 (2010).

[102] P. Romanczuk, M. Bär, W. Ebeling, B. Lindner, and L. Schimansky-Geier. Active Brownian particles. From individual to collective stochastic dynamics. *European Physical Journal Special Topics* **202**, 1–162 (2012).

[103] A. Walther and A. Müller. Janus particles. *Soft Matter* **4**, 663–668 (2008).

[104] W. F. Paxton, K. C. Kistler, C. C. Olmeda, A. Sen, S. K. St. Angelo, Y. Cao, T. E. Mallouk, P. E. Lammert, and V. H. Crespi. Catalytic nanomotors: autonomous movement of striped nanorods. *Journal of the American Chemical Society* **126**, 13424–13431 (2004).

[105] S. Das, A. Garg, A. I. Campbell, J. Howse, A. Sen, D. Velegol, R. Golestanian, and S. J. Ebbens. Boundaries can steer active Janus spheres. *Nature Communications* **6** (2015).

[106] R. A. Pavlick, S. Sengupta, T. McFadden, H. Zhang, and A. Sen. A Polymerization-Powered Motor. *Angewandte Chemie* **123**, 9546–9549 (2011).

[107] J. Deseigne, O. Dauchot, and H. Chaté. Collective motion of vibrated polar disks. *Physical Review Letters* **105**, 098001 (2010).

[108] K. K. Dey, X. Zhao, B. M. Tansi, W. J. Mendez-Ortiz, U. M. Cordova-Figueroa, R. Golestanian, and A. Sen. Micromotors powered by enzyme catalysis. *Nano Letters* **15**, 8311–8315 (2015).

[109] S. van Teeffelen and H. Löwen. Dynamics of a Brownian circle swimmer. *Physical Review E* **78**, 20101 (2008).

[110] S. van Teeffelen, U. Zimmermann, and H. Löwen. Clockwise-directional circle swimmer moves counter-clockwise in Petri dish-and ring-like confinements. *Soft Matter* **5**, 4510–4519 (2009).

[111] A. Kaiser, A. Peshkov, A. Sokolov, B. ten Hagen, H. Löwen, and I. Aranson. Transport powered by bacterial turbulence. *Physical Review Letters* **112**, 158101 (2014).

[112] A. Kaiser, H. H. Wensink, and H. Löwen. How to capture active particles. *Physical Review Letters* **108**, 268307 (2012).

[113] A. Pototsky and H. Stark. Active Brownian particles in two-dimensional traps. *Europhysics Letters* **98**, 50004 (2012).

[114] F. Woodhouse and R. Goldstein. Spontaneous circulation of confined active suspensions. *Physical Review Letters* **109**, 168105 (2012).

[115] K.-T. Wu, J. B. Hishamunda, D. T. N. Chen, S. J. DeCamp, Y.-W. Chang, A. Fernández-Nieves, S. Fraden, and Z. Dogic. Transition from turbulent to coherent flows in confined three-dimensional active fluids. *Science* **355**, 1284 (2017).

[116] T. Brotto, J.-B. Caussin, E. Lauga, and D. Bartolo. Hydrodynamics of confined active fluids. *Physical Review Letters* **110**, 38101 (2013).

[117] B. ten Hagen, R. Wittkowski, D. Takagi, F. Kümmel, C. Bechinger, and H. Löwen. Can the self-propulsion of anisotropic microswimmers be described by using forces and torques? *Journal of Physics: Condensed Matter* **27**, 194110 (2015).

[118] M. Marchetti, J. Joanny, S. Ramaswamy, T. Liverpool, J. Prost, M. Rao, and R. Simha. Hydrodynamics of soft active matter. *Reviews of Modern Physics* **85**, 1143–1189 (2013).

[119] S. Chandrasekhar. Stochastic problems in physics and astronomy. *Reviews of Modern Physics* **15**, 1 (1943).

[120] C. J. Geankoplis. *Transport processes and separation process principles(includes unit operations)*. Prentice Hall Professional Technical Reference (2003).

[121] A. Fick. Ueber Diffusion. *Annalen der Physik* **170**, 59–86 (1855).

[122] P. Heitjans and J. Kärger. *Diffusion in condensed matter: methods, materials, models*. Springer Science & Business Media (2006).

[123] W. Jost. *Diffusion in solids, liquids, gases*. Academic press, New York (1952).

[124] H. Löwen. Melting, freezing and colloidal suspensions. *Physics Reports* **237**, 249–324 (1994).

[125] Y. Singh. Density-functional theory of freezing and properties of the ordered phase. *Physics Reports* **207**, 351–444 (1991).

[126] R. Evans. The nature of the liquid-vapour interface and other topics in the statistical mechanics of non-uniform, classical fluids. *Advances in Physics* **28**, 143–200 (1979).

[127] R. Evans. *Fundamentals of Inhomogeneous Fluids*, chapter 3: Density, pages 85–176. Marcel Dekker, New York, 1 edition (1992).

[128] H. Löwen. Dynamical density functional theory for brownian dynamics of colloidal particles. In: J. Wu, editor, *Variational Methods in Molecular Modeling*, chapter 9, pages 255–284 (2017).

[129] J. Wu and Z. Li. Density-functional theory for complex fluids. *Annual Review of Physical Chemistry* **58**, 85–112 (2007).

[130] D. Oxtoby. Crystallization of liquids: a density functional approach. In: J.-P. Hansen, D. Levesque, and J. Zinn-Justin, editors, *Liquids, Freezing and Glass Transition*, volume 1 of *Proceedings of the Les Houches Summer School, Course LI, 3-28 July 1989*, pages 145–192. USMG, NATO Advanced Study Institute, North Holland, Elsevier Science Publishers B. V., Amsterdam (1991).

[131] J. F. Lutsko. Recent developments in classical density functional theory. *Advances in Chemical Physics* **144**, 1 (2010).

[132] P. Hohenberg and W. Kohn. Inhomogeneous electron gas. *Physical Review* **136**, 864–871 (1964).

[133] N. D. Mermin. Thermal Properties of the Inhomogeneous Electron Gas. *Phys. Rev.* **137**, A1441–A1443 (1965).

[134] W. Kohn and L. Sham. Self-consistent equations including exchange and correlation effects. *Physical Review* **140**, 1133–1138 (1965).

[135] Nobelprize.org. Walter Kohn - Facts (1998). URL `https://www.nobelprize.org/nobel_prizes/chemistry/laureates/1998/kohn-facts.html`.

[136] C. Ebner, W. Saam, and D. Stroud. Density-functional theory of simple classical fluids: I. Surfaces. *Physical Review A* **14**, 2264–2273 (1976).

[137] R. Evans. Density functional theory for inhomogeneous fluids I: Simple fluids in equilibrium. In: B. Cichocki, M. Napiórkowski, and J. Piasecki, editors, *3rd Warsaw School of Statistical Physics*. Warsaw University Press, Warsaw, Poland (2010).

[138] B. Q. Lu, R. Evans, and M. Telo da Gama. The form of the density profile at a liquid-gas interface: Dependence on the intermolecular potential. *Molecular Physics* **55**, 1319–1338 (1985).

[139] W. Curtin. Density-functional theory of crystal-melt interfaces. *Physical Review B* **39**, 6775–6791 (1989).

[140] J. F. Lutsko and G. Nicolis. Theoretical evidence for a dense fluid precursor to crystallization. *Physical Review Letters* **96**, 046102 (2006).

[141] P. Tarazona. Free-energy density functional for hard spheres. *Physical Review A* **31**, 2672 (1985).

[142] W. Curtin and N. Ashcroft. Density-functional theory and freezing of simple liquids. *Physical Review Letters* **56**, 2775–2778 (1986).

[143] W. Curtin and N. Ashcroft. Weighted-density-functional theory of inhomogeneous liquids and the freezing transition. *Physical Review A* **32**, 2909–2919 (1985).

[144] A. Denton and N. Ashcroft. Modified weighted-density-functional theory of nonuniform classical liquids. *Physical Review A* **39**, 4701–4708 (1989).

[145] Y. Rosenfeld. Free-energy model for the inhomogeneous hard-sphere fluid mixture and density-functional theory of freezing. *Physical Review Letters* **63**, 980–983 (1989).

[146] R. Roth, R. Evans, A. Lang, and G. Kahl. Fundamental measure theory for hard-sphere mixtures revisited: the White Bear version. *Journal of Physics: Condensed Matter* **14**, 12063–12078 (2002).

[147] H. Hansen-Goos and R. Roth. Density functional theory for hard-sphere mixtures: the White Bear version mark II. *Journal of Physics: Condensed Matter* **18**, 8413 (2006).

[148] H. Hansen-Goos and K. Mecke. Fundamental measure theory for inhomogeneous fluids of nonspherical hard particles. *Physical Review Letters* **102**, 18302 (2009).

[149] T. Ramakrishnan and M. Yussouff. First-principles order-parameter theory of freezing. *Physical Review B* **19**, 2775–2794 (1979).

[150] A. Haymet and D. W. Oxtoby. A molecular theory for the solid–liquid interface. *Journal of Chemical Physics* **74**, 2559–2565 (1981).

[151] D. Oxtoby and A. Haymet. A molecular theory of the solid-liquid interface. II. Study of bcc crystal-melt interfaces. *Journal of Chemical Physics* **76**, 6262–6272 (1982).

[152] D. Dean. Langevin equation for the density of a system of interacting Langevin processes. *Journal of Physics A: Mathematical and General* **29**, L613–L617 (1996).

[153] K. Kawasaki and S. Miyazima. Path integral formulation of dynamical density functional equation for dense fluids. *Zeitschrift für Physik B Condensed Matter* **103**, 423–431 (1997).

[154] U. Marconi and P. Tarazona. Dynamic density functional theory of fluids. *Journal of Chemical Physics* **110**, 8032–8044 (1999).

[155] A. Archer and R. Evans. Dynamical density functional theory and its application to spinodal decomposition. *Journal of Chemical Physics* **121**, 4246–4254 (2004).

[156] P. Español and H. Löwen. Derivation of dynamical density functional theory using the projection operator technique. *Journal of Chemical Physics* **131**, 244101 (2009).

[157] R. Lovett, C. Y. Mou, and F. P. Buff. The structure of the liquid–vapor interface. *Journal of Chemical Physics* **65**, 570–572 (1976).

[158] D. Enskog. Kinetic theory of heat conductivity, viscosity and diffusion in certain condensed gases and liquids. *Kungl. Svenska Vetenskap. Handl* **63**, 42 (1922).

[159] H. Van Beijeren and M. H. Ernst. The modified Enskog equation. *Physica* **68**, 437–456 (1973).

[160] H. Löwen. Density Functional Theory for Inhomogeneous Fluids II: Statics, Dynamics, and Applications. In: B. Cichocki, M. Napiórkowski, and J. Piasecki, editors, *3rd Warsaw School of Statistical Physics*, chapter 3, pages 87–121. Warsaw University Press, Warsaw, Poland (2010).

[161] M. Rex and H. Löwen. Dynamical density functional theory with hydrodynamic interactions and colloids in unstable traps. *Physical Review Letters* **101**, 148302 (2008).

[162] M. Rex and H. Löwen. Dynamical density functional theory for colloidal dispersions including hydrodynamic interactions. *European Physical Journal E* **28**, 139–146 (2009).

[163] A. M. Menzel, A. Saha, C. Hoell, and H. Löwen. Dynamical density functional theory for microswimmers. *Journal of Chemical Physics* **144**, 024115 (2016).

[164] H. H. Wensink and H. Löwen. Aggregation of self-propelled colloidal rods near confining walls. *Physical Review E* **78**, 31409 (2008).

[165] R. Wittkowski and H. Löwen. Dynamical density functional theory for colloidal particles with arbitrary shape. *Molecular Physics* **109**, 2935–2943 (2011).

[166] M. Enculescu and H. Stark. Active colloidal suspensions exhibit polar order under gravity. *Physical Review Letters* **107**, 58301 (2011).